A spin-polarized scanning tunneling microscopy and spectroscopy study of individual nanoscale particles grown on copper surfaces

Dissertation

zur Erlangung des akademischen Grades
doctor rerum naturalium (Dr. rer. nat.)

vorgelegt der
Naturwissenschaftlichen Fakultät II
der Martin-Luther-Universität Halle-Wittenberg

von Herrn **Dipl.-Phys. Sebastian Wedekind**
geboren am 16.06.1981 in Halle an der Saale

angefertigt am
Max-Planck-Institut für Mikrostrukturphysik
in Halle an der Saale

verteidigt am 01. Juni 2010

Gutachter:

1. Prof. Dr. Jürgen Kirschner
2. Prof. Dr. Wolf Widdra
3. Prof. Dr. Bene Poelsema

Halle an der Saale, 27. November 2009

Contents

Chapter 1

Introduction

Electronics and magnetism on the nanometer scale have for a long time been a topic of substantial interest, since both exhibit very often new and unexpected physical phenomena [1–5]. In the last three decades scanning tunneling microscopy (STM) [6,7] and spectroscopy (STS) [8] have developed into very powerful tools to study the morphology and electronic structure of nanometer sized objects. Within the last decade, these already fascinating capabilities have been extended to also study magnetism on the nanometer scale by spin-polarized scanning tunneling microscopy (spin-STM) [9,10]. With its unsurpassed spatial resolution spin-STM offers the way to study magnetic properties of nanometer scaled particles and even single atoms [11–13]. Spin-polarized STM is the experimental technique used in this thesis.

Already in the early 1990's Crommie and others reported the first studies on quantum interference phenomena of surface state electrons on metal surfaces [1, 2, 14, 15]. Since then models based on simplified boundary value problems have been utilized in order to describe the observed interference patterns and the corresponding energy states. I demonstrate in my thesis that the wave-vector quantization due to electron confinement within nanostructures can be described by a one-dimensional quantization rule. Also a new method to identify the eigenstates of the confined electron gas is introduced. This method utilizes a Fast Fourier Transformation (FFT) of the STM data and is capable of identifying all eigenstates of the system, in contrast to the previous approach, which only predicted half of the eigenstates.

This thesis also advances the field of spin-STM by introducing a new measurement scheme. This approach extends the previously introduced use of non-magnetic tips covered with a magnetic material [9] with spectroscopy measurements on individual nanoparticles in magnetic fields. In an advance of previous work [16–18] this leads to a reliable characterization of magnetic tips used in spin-STM. In this work the magnetic configuration of the tip is characterized by measuring hysteresis loops of the differential conductance of single nanostructures in an external magnetic field. It is demonstrated that this is a necessary condition for a reliable analysis of the magnetic contrast in spin-STM, and novel insight into the unexpectedly complex magnetic response of tips used in spin-STM studies to external fields is presented.

This new technique opens the way to tackle a fundamental aspect of nanoscale magnetism for the first time, i.e. the magnetic switching field of an individual particle supported by a metal surface. We measure hysteresis loops of the differential conductance on bilayer high Co islands grown on Cu(111), which is a well known prototype

system [16, 19–25], and extract the magnetic switching field of individual Co islands. Previous studies on the switching of magnetic particles [26–29], mostly performed on huge ensembles, were lacking a diligent characterization of the structural, chemical and electronic properties of their samples and the magnetic properties of the single particles were often disguised by ensemble properties. The capabilities of STM enable us to perform this missing characterization and to study the size and temperature dependence of the magnetic switching field of individual particles for the first time.

It is of large current interest to control at the same time both, the electronic as well as the magnetic properties of nanostructures. The physical quantity of high relevance in this respect is the spin-polarization of electrons. Recent theoretical work predicted a spatial modulation of the spin-polarization within Co islands on Cu(111) [30], though the authors could not provide any experimental evidence for their results. This missing experimental evidence is provided here. We present the first measurement of the spatially modulated spin-polarization within a single nanometer scaled object. Our findings might open a new way of tailoring the spin-polarization on the nanometer scale.

To study the electronic and magnetic properties of individual nanostructures or even single atoms, it is often preferable to have a very limited electronic coupling between the nanostructure and the substrate. Recently it was demonstrated that Copper nitride systems, such as Cu_2N on Cu(100) [12,31], can act as a decoupling layer. Here we investigate the similar system of Cu(110)-p(2×3)N (Cu_3N on Cu(110)) [32, 33]. In addition to the expected decoupling effect, this system is especially interesting, since it turned out to be a very versatile substrate for growing nanowires from numerous metals [34, 35]. However, none of the previous reports investigated the electronic properties of neither the Cu_3N substrate nor the wires grown on top. Here, the first results on the electronic structure of Cu_3N and Co wires grown on top of it are presented. Our findings indicate a strong electronic coupling between the Co wires and the Cu_3N substrate, which questions the use of Cu_3N on Cu(110) as a decoupling layer.

This thesis is organized in the following way. Chapter 2 introduces the basic theoretical concept of tunneling and spin-polarized scanning tunneling microscopy and spectroscopy. The experimental equipment used for this work, especially the low temperature STM operated in an external magnetic field, is described in chapter 3. The same chapter specifies the preparation of samples and STM tips. In chapter 4 I present the experimental results on the electronic and magnetic properties of Co islands on Cu(111). In this chapter it is shown that the dispersion relation of surface state electrons is discrete in the wave-vector k within a Cu stripe and within Co islands on Cu(111) due to electron confinement. Spin-polarized studies reveal the size and temperature dependence of the switching field of individual Co islands. Chapter 4 closes with a description of spin-polarized electron confinement within an individual Co island. Results on the morphology and electronic structure of Cu(110)-p(2×3)N, and Co nanowires grown on top of it are presented in chapter 5.

All experimental results are discussed in chapter 6. It is shown that the discrete dispersion relations obtained for a Cu stripe on Cu(111) and within Co islands can be explained by electron wave-vector quantization. The data obtained for the size and temperature dependence is tentatively analyzed within the framework of thermally assisted coherent magnetization reversal [36–39]. However, it is demonstrated that this simple model clearly fails to describe our experimental results. Possible explanations for that failure and alternative magnetization reversal processes are discussed, also in view of recent theoretical results. The discussion of data obtained on spin-polarized electron confinement within a Co island reveals, that these measurements probe the spatial variation of the spin-polarization within the island. This conclusion is supported by corresponding ab-initio calculations. The discussion of the electronic properties of Co wires grown on Cu(110)-p(2×3)N closes the discussion chapter. I conclude that a strong electronic coupling of the wires to the underlying Cu nitride substrate is observed, which might question the previous view of Cu_3N as a decoupling layer between nanostructures and substrate.

The major conclusions of the thesis and indications for future prospects are presented at the end.

Chapter 2

Theoretical background

2.1 Tunneling and scanning tunneling microscopy

Since its invention by Binnig and Rohrer [6, 7] at the laboratories of IBM in Rüschlikon, Switzerland in 1981 the scanning tunneling microscope (STM) has developed into a powerful technique for investigating surfaces at the atomic scale. With its unsurpassed spatial resolution the STM opened the way to a whole new field of investigating the physical properties of nanometer sized structures and even single atoms. This section gives a short introduction to the very basic principles of STM, scanning tunneling spectroscopy (STS) and also to spin-polarized tunneling. It is, however, not the aim to give a comprehensive description of all phenomena occurring in real STM experiments, since more complete descriptions of the topic can be found in numerous textbooks [40–43].

To model the STM experiments performed in this thesis we consider a STM consisting of a sharp metallic tip and a metallic sample. In a most simplistic model the tunnel process in a STM can be described in analogy to tunneling through a one-dimensional potential barrier. The justification for this stems from an analysis of the energy levels involved in tunneling between tip and sample, as shown in Figure 2.1. The potential barrier in the STM geometry is the vacuum barrier between tip and sample. When tip and sample are brought into close distance, typically several angstrom (Å), wave functions of tip and sample overlap and tunneling between tip and sample occurs. Applying a non-vanishing bias V between sample and tip results in a *net* tunnel current, which is described approximately by:

$$I_T \propto e^{-2\kappa d}, \tag{2.1}$$

where

$$\kappa = \sqrt{2m(\Phi - eV)}/\hbar.$$

Here, d is the width of the vacuum gap and Φ the work function, with $V \ll \Phi$. The voltage applied between tip and sample is, due to the separating vacuum gap, also referred to as V_{Gap}. The work function of a metal surface is the minimum energy required for an electron to be removed from the bulk into the vacuum. For the sake of simplicity the work function is assumed to be the same for tip and sample here. The treatment of tunneling including two different work functions can be found in literature [40].

Figure 2.1(a) sketches a very simplistic picture of the energy diagram for tunneling in STM. Within this simple picture, the tunneling process is described by the following statements: When a positive voltage is applied between sample and tip, only states that
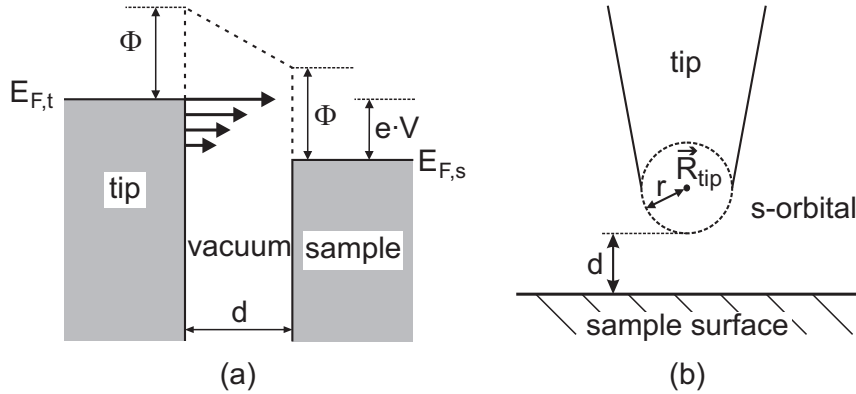
Figure 2.1: Scanning tunneling microscopy. (a) Energy diagram for tunneling in STM. Φ is the work function and $E_{F,t}, E_{F,s}$ are the Fermi energies of tip and sample, respectively. The applied bias V is positive with respect to the sample, so electrons can tunnel from occupied states of the tip into unoccupied states of the sample. Arrows indicate the decreasing tunnel probability of states at lower energies. (b) Tunneling geometry within the Tersoff Hamann model. The tip is approximated by a s-like wave-function at position $\vec{R}_{tip}$ and at distance d from the surface.

are located between the Fermi energy of the tip $E_{F,t}$ and $E_{F,t} - eV$ can contribute to the tunnel current. Note, that preferentially occupied states of the tip which are close to the Fermi level $E_{F,t}$ contribute to I_T, states further away from the Fermi level contribute less to tunneling. This is indicated by arrows across the vacuum barrier in Fig. 2.1. Applying a negative voltage between sample and tip reverses the whole picture. In this case electrons tunnel from occupied states of the sample into unoccupied states of the tip. The real situation in a STM experiment is of course much more complicated, however, main aspects of the experimentally observed phenomena can already be explained by these crude approximations.

As stated above the tunnel current decays exponentially with growing barrier width. The decay length κ is mainly determined by the work function Φ. The work function of most metals is of the order of $4-5$ eV [40, Table 1.1]. Hence, the typical decay constant is $2\kappa \sim 2$ Å^{-1}. Thus, the tunnel current drops by nearly one order of magnitude when increasing the tip-sample distance by 1 Å. This behavior is exploited in STM measurements. The tip is scanned laterally across the surface while the tip-sample distance d is permanently adjusted to keep I_T constant. This is realized by an electronic feedback circuit, which keeps a given tunnel current by operating a piezo actuator, which is moving the tip perpendicular to the surface. If the tip encounters a protrusion on the surface during scanning, the tunnel current increases, due to the reduced tip-sample distance. This rise in tunnel current is detected by the feedback loop, which consequently retracts the tip from the surface by changing the voltage applied to the piezo actuator, until the set current value is reached again. The recorded image is proportional to the voltage applied to the z-piezo of the tip and is a map of the apparent height of the sample (see chapter 3 for instrumentation details). However, it is important to realize that the contrast relies on measurements of the tunnel current, and the link between topography and electronic properties can be far from trivial. This mode of operation is called constant current mode and is the most common mode used in STM measurements. Other modes, such as the

constant height mode are also used in special cases, however STM images presented in this work are always obtained in the constant current mode.

For a full understanding of lateral features in STM images a precise knowledge of the atomic and electronic structure of the tip is required. Yet it is well known, that the exact arrangement of atoms at the apex of a STM tip is extremely hard, if not impossible, to identify or control. In general the atomic structure of the tip apex and also its electronic structure are in most cases unknown. However, in many situations the simple model introduced by Tersoff and Hamann [44, 45] is able to describe the experimental results correctly.

The model of Tersoff and Hamann assumes that the electronic structure of the tip is characterized by a metallic s-orbital and that the applied voltages are much smaller than the work functions of tip and sample. With those assumptions and the geometry shown in Fig. 2.1(b) they derive for the tunnel current:

$$I_T \propto \rho_{tip}(E_{F,t}) \cdot \rho_{sample}(\overrightarrow{R}_{tip}, E_{F,s}) \cdot V, \tag{2.2}$$

where $\rho_{tip}(E_F)$ is the density of states of the tip and $\rho_{sample}(\overrightarrow{R}_{tip}, E_F)$ is the density of states of the sample surface at the center $\overrightarrow{R}_{tip}$ of the tip s-orbital at the Fermi energy E_F. Hence, within this simplified model the spatial variations in the tunnel current, measured by STM, are proportional to the local electronic density of states of the sample at the Fermi energy at the tip apex position. However, the investigation of metal surfaces revealed that the Tersoff-Hamann model systematically underestimates the atomic corrugation observed in the experiments. It was found by Chen [46], that considering d states at the tip leads to a much improved description of the atomic corrugation observed in experiment.

At larger bias voltages, which do not fulfill the criterion $V \ll \Phi$, the tunnel current is better described by a weighted integral over the sample density of states:

$$I_T \propto \int_0^{eV} \rho_{sample}(E_{F,s} + \epsilon)\rho_{tip}(E_{F,t} - eV + \epsilon)T(\epsilon, eV)d\epsilon, \tag{2.3}$$

where $T(\epsilon, eV)$ is a transmission coefficient which depends on the applied voltage and the energy of the tunneling electrons. In contrast to equation (2.2) the high voltage extension takes into account that all states between the Fermi energies of tip and sample contribute to the tunnel current and not only the states close to $E_{F,t}$. The contributions of the different states are weighted by the transmission coefficient T. A close investigation of $T(\epsilon, eV)$ reveals, that states close to the Fermi energy are the dominant contribution and that the tunneling probability decreases exponentially with decreasing energy [41], as indicated by the arrows in Fig. 2.1(a).

A more complete description of transport phenomena in mesoscopic systems, including the STM geometry, is given by the Landauer-Büttiker formalism [47–49]. Landauer introduced the idea, that the transport of non-interacting particles, e.g. electrons, between two reservoirs can be described by transport through a number of independent channels or modes. Later, Büttiker extended this concept by including the treatment of n leads. The Landauer-Büttiker formalism describes tunneling in an STM as a scattering problem (see e.g. [50]) and all transport properties derived within this formalism are governed by the transmission probability. This approach yields in general a better description of the tunneling processes than the simple Tersoff Hamann theory. This improved description is

on the one hand achieved by considering a more complicated electronic structure of the tip, and not only a simple s state as in the Tersoff Hamann model, and by taking into account the complete electronic structure of the tip, and not only the LDOS at the Fermi energy $\rho_{tip}(E_{F,t})$. In addition the Landauer-Büttiker formalism can treat, apart from the simplified geometry illustrated in Fig. 2.1, virtually any tip sample geometry. Thus, within this formalism a much better modeling of the experimental situation is feasible.

The Landauer-Büttiker formalism is also used to describe spin-polarized tunneling experiments [51,52]. Here, the concept of different transport channels is used to treat the tunneling of spin-up and spin-down electrons independently. Comprehensive descriptions of advanced theories on transport phenomena in mesoscopic and nanoscale system can be found in [53,54].

2.2   Spectroscopy

One most interesting aspect of STM measurements is the possibility to gain information about the electronic properties of the sample. The local density of states (LDOS) of the sample can be retrieved from the voltage dependent derivative of the tunnel current $dI/dV(V)$ by differentiating equation (2.3):

$$\frac{dI}{dV}(V) \propto \rho_s(eV) \cdot \rho_t(E_{F,t}) \cdot T(eV,eV) + \int\limits_0^{eV} \rho_s(E_{F,s}+\epsilon)\rho_t(E_{F,t}-eV+\epsilon)\frac{d[T(\epsilon,V)]}{dV}d\epsilon. \quad (2.4)$$

At first sight it seems very demanding to extract the desired sample LDOS $\rho_s(eV)$ from the above relation. However, in a lot of cases the second term turns out to be negligible and in first approximation one obtains:

$$\frac{dI}{dV}(V) \propto \rho_s(eV) \cdot \rho_t(E_{F,t}) \cdot T(eV,eV). \quad (2.5)$$

A close inspection of the transmission coefficient T, which is usually unknown, reveals that it is a smooth, monotonic increasing function of the applied bias [41]. Thus, the transmission coefficient (or transmission probability) adds a smooth varying background to the measured $dI/dV(V)$ spectra. Consequently spectral features in the $dI/dV(V)$ signal can usually be assigned to variations of the sample LDOS. See Fiete and Heller for a recent review [55]. Later in section 4.3.1 I shall demonstrate that this approach can be successfully applied also to spin-dependent dI/dV measurements.

When comparing spectroscopy data with theoretical predictions it is in some situations desirable to estimate the influence of the bulk band structure on the tunneling process. From very principle considerations it becomes clear that the band structure influences tunneling spectra, since the decay length of tip and sample states into the vacuum is determined by their momentum perpendicular to the surface $k_\perp$ [41]. The effective height of the tunneling barrier depends on the electron energy, and the higher $k_\perp$ the higher the tunneling probability. Using $k^2 = k_\perp^2 + k_\parallel^2$ [41] the effects of a non-vanishing momentum parallel to the surface can be included by replacing the electron energy E by

$$E - \hbar^2 \frac{k_\parallel^2}{2m}.$$

Thus, a vanishing $k_\parallel$ leads to the largest energy and consequently to the highest tunneling probability. Therefore states with zero $k_\parallel$ have the longest decay length. These states, at the $\overline{\Gamma}$ point of the surface Brillouin zone, are preferentially probed by STM measurements. These considerations become important in section 6.4, where the calculated LDOS of a Co bilayer on Cu(111) is compared to dI/dV spectra.

2.3 Spin-polarized tunneling

The major topic of this thesis are spin-dependent scanning tunneling spectroscopy measurements. Hence, this section gives a short introduction to the mechanisms relevant for the contrast in spin-STM measurements. Comprehensive reviews of the topic are given by Bode [9] and Wulfhekel and Kirschner [10].

Jullière discovered in 1975 that the tunnel current between two ferromagnetic electrodes depends on the relative orientation of the magnetization directions of both electrodes [56]. In his experiments with Fe-Ge-Co tunnel junctions he found that a parallel alignment of the magnetization directions of both electrodes leads to a high tunnel current, while an antiparallel alignment results in a low tunnel current. This phenomenon was later called magnetic valve effect. A theoretical treatment of spin dependent tunneling between two spin-polarized electrodes was later on given by Slonczewski [57]. Slonczewski found that, under the assumption of free electrons, a vanishing external bias and $T = 0$ K, the spin-polarized tunnel current is given by:

$$I_{SP} = I_0(1 + P_1 P_2 \cos\theta). \tag{2.6}$$

Here, I_0 is the non-spin-polarized part of the current, $P_{1,2}$ are the spin polarizations of the two electrodes and θ is the angle between the magnetization directions of the two electrodes. In the STM geometry the two electrodes are the tip and the sample. Assuming a constant spin polarization of the tip P_t, the tunnel current I_{SP} at a fixed position of the sample depends on the local spin polarization of the sample P_s and on variations of the angle θ. The two extreme cases of parallel ($\theta = 0°$) and antiparallel ($\theta = 180°$) alignment of tip and sample magnetization lead to the largest difference in the tunnel current:

$$I_{\uparrow\uparrow} = I_0(1 + P_s P_t) \qquad ; \ \theta = 0° \tag{2.7}$$

$$I_{\downarrow\uparrow} = I_0(1 - P_s P_t) \qquad ; \ \theta = 180° \tag{2.8}$$

Please note that any change of θ can lead to a change of the measured tunnel current. The simple cosine dependence of I_{SP} on θ was observed experimentally in planar tunnel junctions by Miyazaki [58] and Moodera [59]. However, only recently it has been confirmed by ab-initio calculations by [52] and [60], which were both partially triggered by the results presented here.

Czerner et al. [52] calculated the ballistic transport between two magnetic electrodes in the framework of the Landauer-Büttiker approach using KKR Green's functions including non-collinear magnetic order. In this thesis spin-STM experiments are performed on bilayer high Co islands grown on Cu(111) and with Cr covered W tips. To resemble this experimental situation, the authors of [52] used two semi-infinite Cu(111) electrodes, where one electrode was covered with two monolayers of Co and one with a cluster of Cr atoms to model the STM tip. The two electrodes are separated by a vacuum barrier of three equivalent Cu monolayers. Modeling the tip as a tetrahedral cluster of Cr atoms,
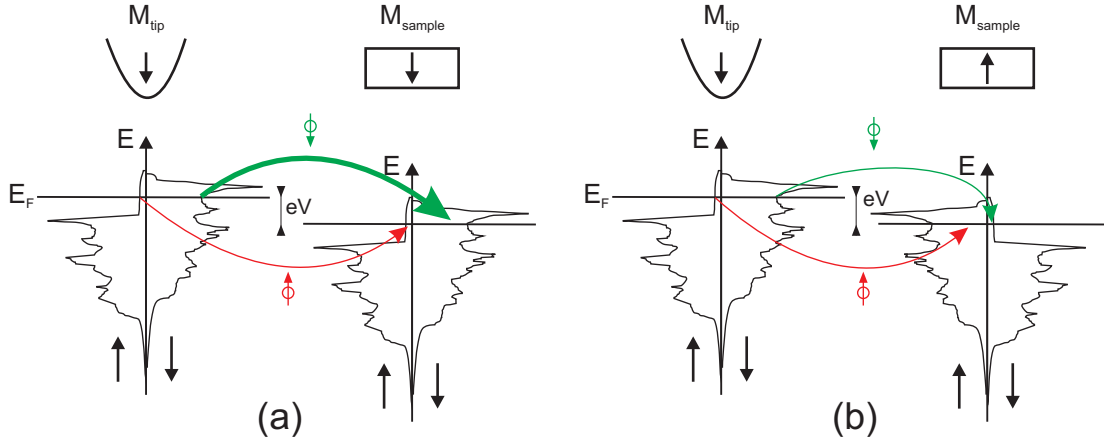
Figure 2.2: Simplified picture of spin polarized tunneling. The electronic structure of tip and sample is represented by the calculated spin-resolved electronic density of states of bulk fcc Co taken from [61]. The spin orientation of the tunneling electrons is assumed to be conserved during tunneling, i.e. spin-up electrons always tunnel into spin-up states (red arrow) and spin-down electrons always tunnel into spin-down states (green arrow). Black arrows indicate the DOS of spin-up and spin-down electrons. $M_{tip,sample}$ denote the magnetization orientation of tip and sample, respectively. (a) Parallel and (b) antiparallel alignment of tip and sample magnetization lead to high and low tunnel current, respectively.

the calculations find, that all possible collinear spin configurations lead to a non-zero magnetization of the tip[1]. In a next step the conductance between the two electrodes was calculated for different angles between the magnetizations of the Co bilayer and the Cr cluster. The calculations reveal a sinusoidal behavior of the conductance with respect to the relative orientation between the magnetizations of the Co bilayer and the Cr tip. Hence, the angular dependence of the tunnel current predicted by Slonczewski was reproduced by ab-initio calculations.

Figure 2.2 presents a sketch of spin polarized tunneling involving spin-split density of states. In this picture it is assumed that the spin orientation of the tunneling electrons is conserved. It was found that this assumption is well justified in the limit of low bias voltage [9], where the tunnel current is dominated by elastic processes. In Fig. 2.2(a) the situation for a parallel alignment of tip and sample magnetization is shown. For the sake of simplicity the electronic density of states (DOS) of bulk Co is chosen to represent the electronic structure of both tip and sample. Under parallel alignment and with a positive voltage V applied between sample and tip, electrons can tunnel from occupied spin-up (spin-down) states of the tip into unoccupied spin-up (spin-down) states of the sample. The high DOS of spin-down electrons at the Fermi energy of tip and sample results in a high tunnel current (marked by the thick green arrow). The contribution of spin-up electrons to the tunnel current is very small, due to the reduced spin-up DOS at the Fermi level, as marked by the thin red arrow. In 2.2(b) the magnetization of the sample is reversed, the DOS of spin-up and spin-down electrons are swapped. Now the number of unoccupied sample states of spin-down character is strongly diminished, which leads to

---

[1]This surprising result will be further discussed in section 6.2

a low tunnel current of the spin-down electrons. For the spin-up electrons the situation remains unchanged. Despite the higher density of unoccupied states in the sample, the number of occupied tip states available for tunneling is unchanged. In total the tunnel current is smaller in the antiparallel situation.

The spin-dependence of the differential conductivity $dI/dV(V)$ can be explained by the same picture. However, the $dI/dV(V)$ signal is determined by the DOS of the sample in a small energy window around the applied voltage. Therefore, the statement for the tunnel current made above, that parallel alignment of the magnetizations of tip and sample leads to a high current and antiparallel alignment to a low current, is not always valid for the $dI/dV(V)$ signal. Depending on the electronic structure of tip and sample, parallel aligned tip and sample magnetizations can result in a low or in a high amplitude of the $dI/dV(V)$ signal. This effect is observed by our experiments presented in section 4.3.1 and further discussed in section 6.2.

The above considerations demonstrate the necessity of having a spin-polarized STM tip. Today mainly two different approaches to achieve a spin-polarization of STM tips are successfully used. The first one relies on covering a non-magnetic tip, like tungsten, with a magnetic material. Covering materials, that have been reported in literature include Fe, Co, Gd, Cr (see e.g. [9] and references therein). In addition to the tip covering approach, also the use of bulk tips with antiferromagnetic (e.g. Cr [62]) or ferromagnetic (e.g. Ni [43]) ordering has been proposed. The second, fundamentally different approach was introduced by Johnson and Clarke [63] and further developed by Wulfhekel at the MPI Halle [64]. This approach uses a very soft magnetic tip whose magnetization direction is periodically switched by 180° through a coil that is wound around the tip. Whether the tip is sensitive to the out-of-plane or in-plane component of the sample magnetization is determined by the shape of the tip. For the very soft tip material used by Wulfhekel the easy magnetization axis is determined by shape anisotropy. Ring shaped tips are found to have in-plane sensitivity, whereas needle shaped tips exhibit out-of-plane sensitivity. However, no spin-dependent measurements can be performed in an external magnetic field, as the external field pins the magnetization direction of the tip, suppressing the modulation of M_{tip}. Thus, in this work the first approach of covering tips with a magnetic material is used, and its application is described in section 3.2.

Chapter 3

Experimental setup

Spin-polarized scanning tunneling microscopy (STM) studies aim at exploring structural, electronic and magnetic properties of nanoscopic objects on surfaces. Hence, clean and well defined surfaces are the necessary prerequisite for successfully retrieving the desired physical properties from the systems under investigation. To achieve that goal, all measurements presented in this work are performed under ultra high vacuum (UHV) conditions. Under these conditions surfaces can stay clean on atomic scales for very long time periods from hours to days, due to the low residual gas pressure in the chamber.

This chapter describes first the low temperature scanning tunneling microscope that was used to perform all presented measurements. In the second part tip and sample preparation are described. STM tips, covered with magnetic material for studying the magnetic properties of single nanoparticles are briefly discussed. A thorough discussion of the preparation of tips for magnetic studies is presented in section 6.2.

3.1 The Cryo-SFM

The results presented in this work have all been achieved by using the so-called Cryogenic SFM. This system is commercially available from Omicron NanoTechnology[1] and is based on a scanning probe microscope described by Hug et al. [65]. The Cryogenic SFM is an instrument dedicated to operate at cryogenic temperatures and in high magnetic fields. In addition to STM, an interferometric glass fiber setup enables full atomic force microscopy (AFM) capabilities [66]. However, here I only used the STM capabilities. The instrument is operated inside a ^{4}He bath cryostat (Janis Corp.) with optical access and it is attached to a UHV chamber (Fig. 3.1). The base pressure of the STM chamber is as low as 2×10^{-11} mbar, and it is estimated to be orders of magnitudes smaller at the STM head in the cryostat, where the temperature reaches $7 - 8$ K. The cryostat is equipped with a superconducting split coil magnet that can produce magnetic fields of up to 7 T in the vertical direction. An even higher field value of 8 T can be achieved by operating the Lambda plate [67], when the temperature of the lHe bath surrounding the superconducting magnet is lowered by reducing the vapor pressure of the He in the reservoir. Thus, higher critical fields are accessible [68].

A home-built preparation chamber is attached to the STM chamber via a gate valve. Figure 3.1 shows a picture of the complete UHV setup. The preparation chamber is
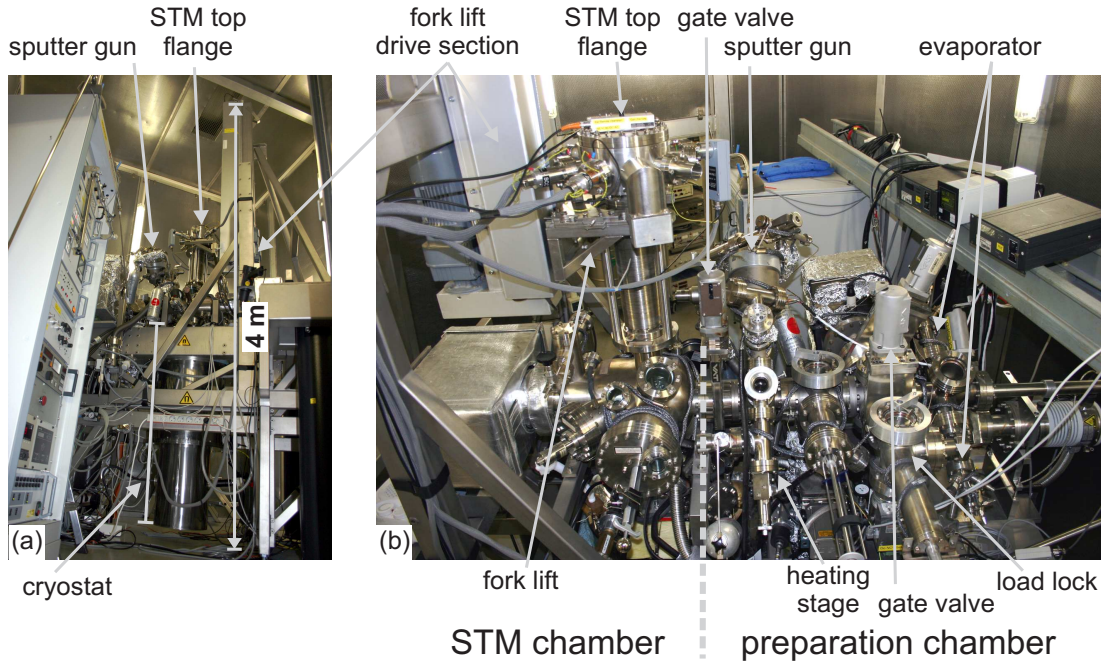
---

[1]www.omicron.de

Figure 3.1: The ultra high vacuum (UHV) chamber containing the low-temperature scanning tunneling microscope. (a) Side view on the system. Part of the cryostat is visible inside the main stainless steel frame. (b) Top view on the complete system. The STM chamber on the left houses the STM. The picture shows the STM lowered into the cryostat. The right part shows the preparation chamber which is separated from the STM chamber by a gate valve.

equipped with a scanning ion gun and a home-built sample and tip heating stage for cleaning purposes. Three evaporators can be used to deposit different metals onto samples and also tips. The preparation chamber is also equipped with a load lock which is pumped and degassed separately. The load lock allows fast introduction (within three hours) and removal (within 10 minutes) of samples and tips into and out of UHV.

The STM is spring-suspended on an almost two meter long column with the STM head (see Fig. 3.3) at the lower end. During measurements the whole column is inserted into the cryostat. In order to perform tip or sample preparation the STM has to be lifted up from the cryostat. This is done by a dedicated fork lift attached to the STM chamber. It raises the STM top flange (see Fig. 3.1), which is connected to the upper end of the STM column, until the STM head has reached the level of the preparation chamber. Subsequently a linear transfer rod and two wobble sticks can be used to transfer tip and/or sample to the desired preparation position. After preparation, tip and sample are put back into the STM and the microscope is lowered into the cryostat again. The subsequent cooling down from room to operating temperature $(7 - 8 \text{ K})$ typically takes $8 - 10$ hours. The temperature of the STM is monitored by two Cernox$^{\text{TM}}$ sensors, mounted in close proximity to the sample stage of the STM head. This sensor is characterized by low magnetic field induced errors $(\Delta T/T = -0.4\%$ at 8 T and 10 K) and by a high temperature range of 100 mK to 420 K [69].

The Cernox sensors are read out by a LakeShore temperature controller. The same controller is also used to set the temperature of the STM to values above its equilibrium
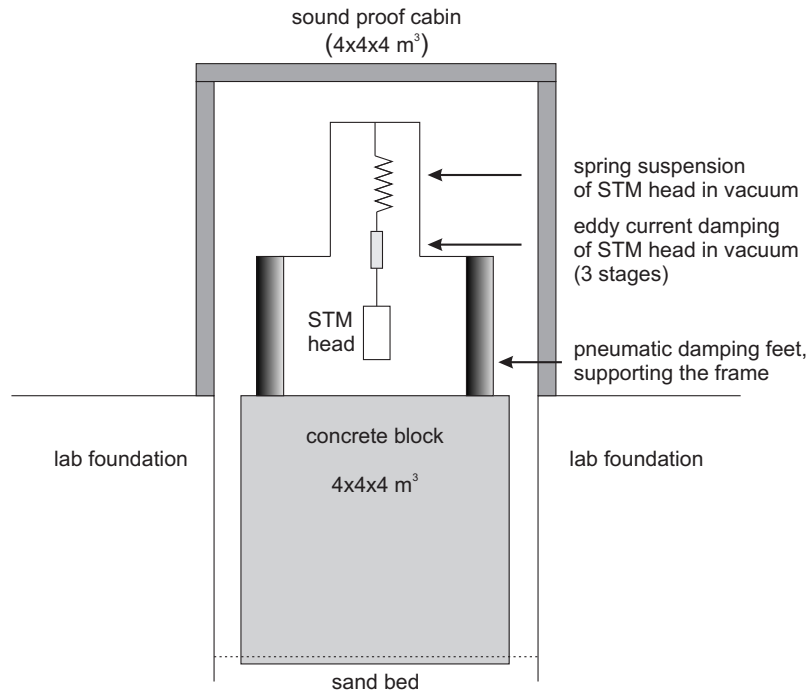
Figure 3.2: Sketch of measures taken to minimize the noise level of the STM. See text for explanations.

value of $7 - 8$ K. This is realized by energizing a resistive heater which is build into the STM head. The temperature controller is able to keep the temperature of the STM within ± 0.1 K around the set temperature. The temperature of the STM can be lowered by reducing the vapor pressure above the lHe reservoir. Thus, the equilibrium temperature of the STM can be lowered by roughly 1 K and kept for several hours, until the lHe reservoir is emptied due to pumping on its gas outlet.

Different measures are taken to minimize the noise level during STM measurements, Figure 3.2 shows a sketch of the different damping and suspension systems. The UHV system is based on an air damped rigid frame. In measurement mode the complete frame is floating on an air based damping system. This is a measure against coupling of mechanical vibrations from the ground to the microscope. Inside the UHV chamber the STM head is hanging on a spring suspension and residual vibrations are damped by a three-stage eddy current damping. A further relevant aspect is the foundation on which the UHV chamber is positioned. It consists of a solid concrete cube with a base length of 4 meters which is sitting in its own sand bed. This leads to a complete decoupling of the block from the rest of the building and consequently to an extremely efficient noise reduction for the STM. Furthermore a sound proof cabin surrounds the UHV chamber. This cabin prevents acoustical vibrations to couple to the STM. In operation mode the doors to the cabin are closed and the system is efficiently shielded from external acoustical noise.

The noise level of the tip-sample distance is estimated from so-called point mode measurements. In this special measuring mode the STM tip is placed at a fixed position over the sample and a constant current "image" is recorded at this one point of the sample. Since the position of the tip is fixed in this mode, variations of the tip-sample distance are only due to mechanical or electrical noise. Under optimal conditions the noise level,
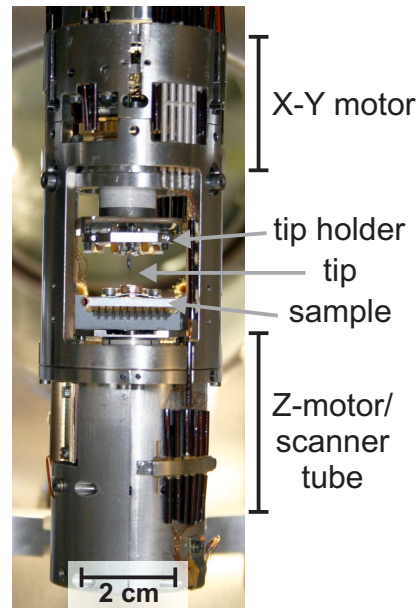
Figure 3.3: Head of the LT-STM with tip and sample inserted. The piezo motors for moving tip and sample are hidden in the upper and lower cylinder, respectively. A detailed view of tip and sample holder is presented in Fig. 3.9

as estimated from point mode measurements, is considerably below 1 pm. This value is a factor 30 lower than the noise level guaranteed by the manufacturer Omicron.

The heart of the STM, the so-called STM head, is shown in Figure 3.3. It consists of the sample and tip reception stages, with sample plate and tip holder, and the piezo-electric actuators to move both parts. The design of the SFM head is completely non-magnetic and enables full three-dimensional tip and sample positioning. The x-y-motor used for lateral coarse motion of the tip is situated in the upper part of the head. The z-motor used for vertical coarse motion is located below the sample plate in the lower part of the head. The vertical coarse motion of the sample plate is designed as a so-called walker [70]. The piezo tube used for the z-movement of the sample during scanning is also located in the lower part. Hence, during image acquisition the tip is fixed, the sample is moving in the z-direction to keep the desired distance to the tip, and the sample is scanned for imaging. At its equilibrium temperature of $7 - 8$ K the thermal drift of the STM during measurement is as low as 1 nm in 24 hours.

Spectroscopy

In addition to the constant current imaging mode [40], I also use the spectroscopy mode. The goal of such measurements is to retrieve information about the electronic structure of the sample. This is done by placing the tip over a position of interest with the stabilization parameters I_{Stab} and V_{Stab}. Then the feedback loop is switched off and the applied bias is ramped between an initial and a final value. Disabling the feedback loop leads to a fixed tip sample distance throughout the measurement. During the voltage ramp the tunnel current is recorded and an $I(V)$ spectrum is obtained at a fixed tip-sample distance. By changing the stabilization parameters it is possible to probe the electronic structure at
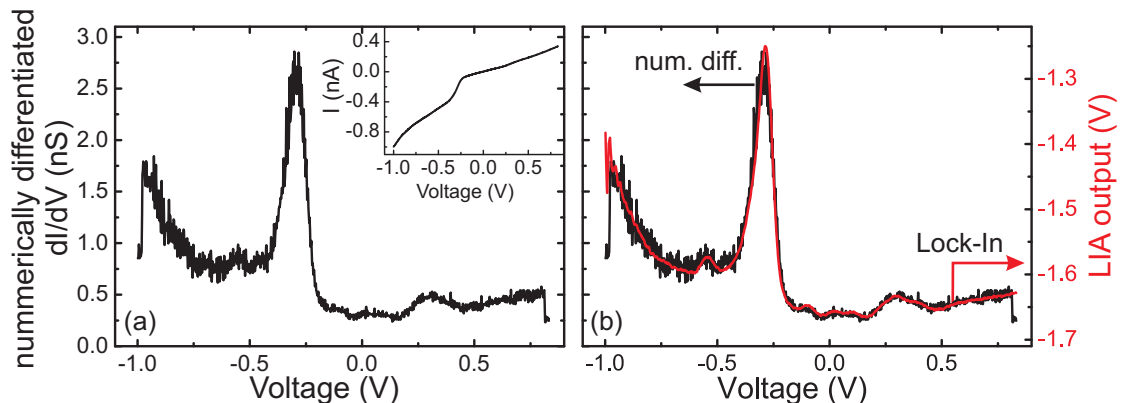
Figure 3.4: Single point spectra measured on a Co island on Cu(111). (a) dI/dV spectrum produced by numerical differentiation of the $I(V)$ spectrum shown in the inset. (b) Numerically differentiated spectrum (black) and dI/dV spectrum measured with a lock-in amplifier (red). The noise level of the lock-in signal is significantly reduced.

different heights above the surface.

In addition to $I(V)$, also the derivative dI/dV is measured simultaneously by a lock-in technique. The derivative dI/dV is within certain approximations, see Sec. 2.2 for details, proportional to the sample LDOS. It could be obtained from the $I(V)$ data by numerical differentiation. However, this method is not preferable since it exhibits a smaller signal to noise ratio. The noise is mainly caused by the numerical differentiation of the experimental, discrete $I(V)$ data. Figure 3.4(a) shows the dI/dV spectrum produced by numerically differentiating the $I(V)$ curve shown in the inset. It exhibits a substantial noise level although the $I(V)$ curve does not show any significant noise. The favorable approach is therefore to measure the dI/dV signal directly with the help of a lock-in amplifier (LIA).

The LIA adds a modulation voltage of the order of $10-20$ mV to V_{Gap}. The modulation frequency is chosen to be well above the cutoff frequency of the tunnel current preamplifier to prevent a modulation of the tip-sample distance and to allow constant current imaging parallel to spectroscopy. In the experiments presented in this work $f_{mod} = 4 - 5$ kHz. The AC component of the tunnel current, which is induced by the modulation of V_{Gap}, is measured phase-sensitive by the LIA. The amplitude of the AC component of the tunnel current corresponds to the derivative of the tunnel current with respect to V_{Gap} [40].

The red curve in Fig. 3.4(b) shows the dI/dV spectrum recorded with the LIA technique parallel to the $I(V)$ curve presented in (a). The noise level is significantly reduced and minute features in the spectrum, such as the small peak left of the large one, appear much clearer. We will see later that the feasibility of detecting these minute features is essential for the experiments within this work. The dI/dV spectrum recorded with the LIA is reliably calibrated with the help of the numerical differentiated dI/dV spectrum. This is shown in Fig. 3.4(b), where a proper scaling and shifting of the LIA data leads to a good match of the numerically differentiated with the LIA measured dI/dV curve. Hence, the LIA data is transformed into a quantitative signal of the differential conductance in units nS. This calibration technique is used throughout the thesis.

Spectroscopy measurements can be performed in single point and in imaging mode. Single point measurements are used to probe the electronic structure of the sample at
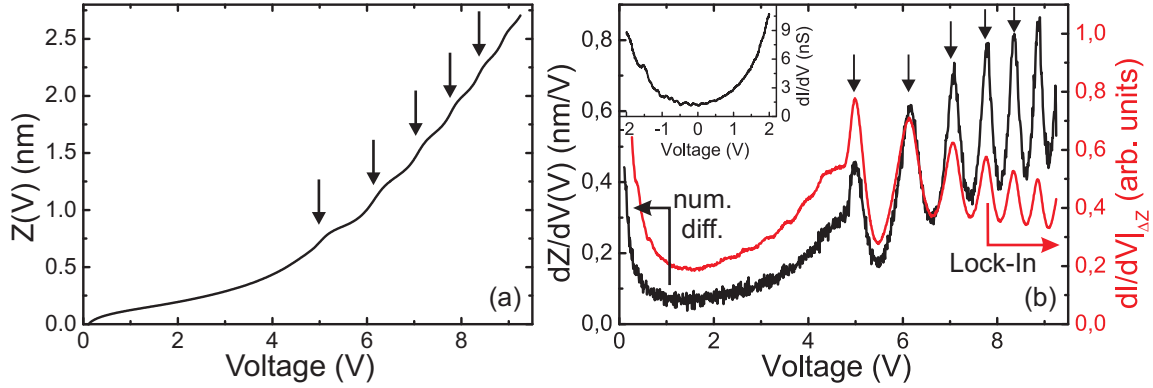
Figure 3.5: $Z(V)$ spectra measured with feedback loop on at a constant $I_T = 1$ nA. (a) $Z(V)$ spectrum measured on Cu(110). Black arrows mark steps in the spectrum. (b) $dI/dV|_{\Delta Z}$ spectrum obtained by numerical differentiation of the data shown in (a) (black) and measured with a lock-in amplifier (red). Arrows mark peak positions corresponding to the steps in the $Z(V)$ data presented in (a).

a fixed position and a fixed tip-sample distance as a function of applied bias, i.e. as a function of energy. The imaging mode is used to map spatial variations of the LDOS at a fixed energy. In this mode the LIA signal is recorded parallel to the imaging with the feedback loop switched on. Note, that in this setup V_{Gap} is applied to the sample and that the tip is on ground potential. Hence, at positive (negative) V_{Gap}, electrons tunnel from occupied states of the tip (sample) into unoccupied states of the sample (tip).

The single point spectroscopy mode can be operated with the feedback loop switched off or on, i.e. at fixed height above the surface or with changing tip sample distance and fixed I_T, respectively. If not indicated differently, the spectra shown in this work are all recorded with the feedback switched off. In this mode the usable bias range is limited by the exponential dependence of the tunnel current on the bias. The magnitude of the tunnel current increases exponentially for $|V_{Gap}| > 2$ V, and spectroscopic details of the $I(V)$ signal reside on a strongly changing background, rendering their detection difficult.

One way to circumvent this issue is to record spectra with the feedback switched on. Fig. 3.5(a) shows an $Z(V)$ curve obtained with feedback on. It shows a series of steps (arrows) on a strongly increasing background. These steps are a signature of image potential states (IPS). This aspect will be presented in greater detail in chapter 5 and discussed in section 6.5. Fig. 3.5(b) shows the numerically differentiated $Z(V)$ signal. The series of peaks visible in this spectrum corresponds to a series of image potential states, as is shown in the discussion in section 6.5. The spectrum exhibits significant noise. This issue is resolved in the same way as described for the dI/dV data above. The red curve is the spectrum recorded parallel to the $I(V)$ spectrum with the help of the LIA. The noise is significantly reduced in this data, the peak positions correspond to those extracted from the numerical differentiation, albeit the relative peak intensities are different. The detailed understanding of this spectroscopy is a topic of present research [71, 72], it is far from trivial, and we exploit peak positions, and not the intensities in chapter 5 and section 6.5.

For the analysis of certain spectroscopy measurements (see section 6.4) it is necessary to estimate the distance between tip and sample during the measurement. Here,

the tip-sample distance is verified by indentation experiments in the following way: The tip is placed at a certain position of the sample and the feedback loop is switched off. Subsequently, while keeping all other parameters constant, the tip is moved closer to the sample by several Å and retracted to the starting position again. The position where this experiment was performed is imaged afterwards to check for changes on the surface. A structural change of the surface, such as a small bump or depression, at this position indicates that the tip has touched the surface. Thus, the distance by which the tip was moved towards the surface is the approximate tip-sample distance. The accuracy of this procedure is increased by repeating this experiment a number of times. Using this approach the tip-sample distance is estimated with a precision of ± 1 Å and for a typical set point of $V_{Gap} = -0.1$ V, $I_T = 1$ nA we estimate a tip-sample distance of 4 Å. As mentioned in section 2.1 a change of the tunnel current by a factor of ten changes the tip-sample distance by only 1 Å.

3.2 Sample and tip preparation

This section presents the experimental techniques to prepare STM tips and sample surfaces studied in this thesis. The first part of this section describes the preparation of Co islands on Cu(111) and the crystallographic properties of the Co islands. After that the preparation of the Cu(110)-p(2×3)N system and the growth of Co nanowires on top of it is described. The second part concentrates on the tip preparation via electrochemical etching and in-situ annealing, and also introduces the preparation of magnetic STM tips required for spin-STM measurements.

Sample preparation

This work focuses on the investigation of structural, electronic and magnetic properties of two systems. Co islands on a Cu(111) surface and Co nanowires on a Cu(110)-p(2×3)N surface. In both cases single crystals have been used. The Cu(111) crystal has been cleaned by cycles of ion bombardment (Ar$^+$, 2×10^{-7} mbar, 1 keV) and subsequent annealing at 700 K. The annealing is done in the heating stage shown in Fig. 3.10(a). The sample plate is heated via electron bombardment from the filament behind it (700 V, 15 mA). It turns out that 3 cycles of sputtering and annealing are sufficient to yield a clean surface, as verified by constant current STM images and dI/dV maps, the latter being highly sensitive to contaminations. Co islands are grown by depositing a submonolayer amount of cobalt at room temperature onto the clean Cu(111) surface. Deposition was performed by an e-beam evaporator. Figure 3.6 shows an STM overview image, which exhibits the Co coverage typically used in this work.

Upon deposition triangular islands, which are two atomic layers high, form on the surface [19–22]. The STM image of one single Co island, shown in Figure 3.7(a) illustrates the triangular shape of the island (cf. Fig. 3.6(a)). However, a close inspection of the STM image reveals that the island exhibits some deviations from the perfect triangular shape and has rather blunt corners. The vast majority of the islands investigated in this work does not have a perfect triangular shape with sharp corners, similar to the example in Fig. 3.7(a). However, for the sake of simplicity they will be called triangular shaped throughout the thesis, and only where it is necessary will the deviations from the perfect triangle be discussed.
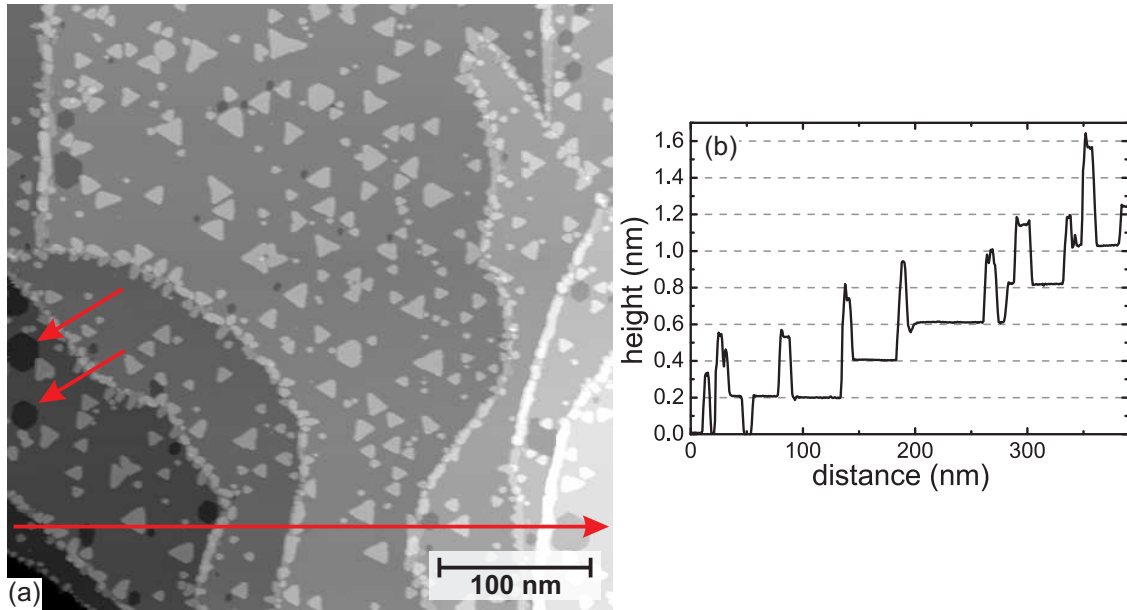
Figure 3.6: STM topography image of Co islands on Cu(111) taken at 8.3 K. Co is deposited at room temperature before cooling the system to 8.3 K. Imaging conditions: $V_{Gap} = -0.1$ V, $I_T = 1$ nA. (b) Line scan along the horizontal red arrow in (a). Monoatomic steps of 2.1 Å separate terraces. Step edge decoration occurs by Co, and monolayer deep holes are visible (red arrows).
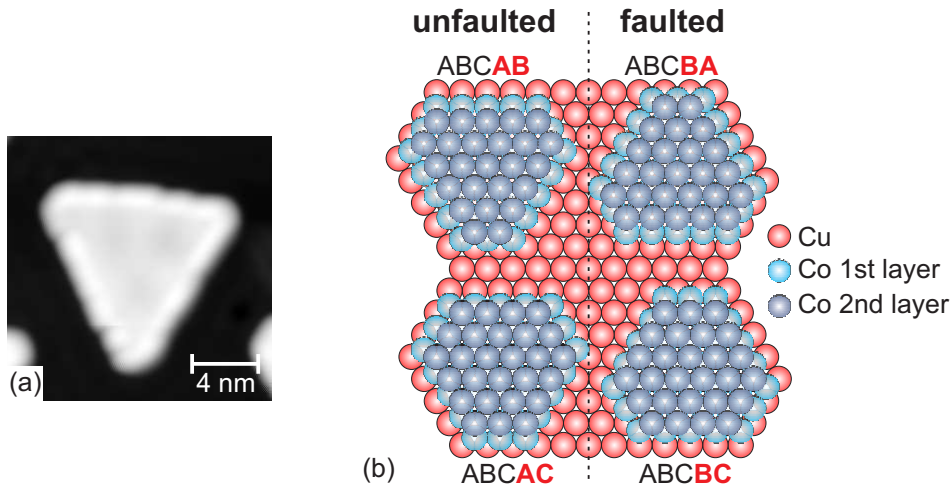

Figure 3.7: Crystallographic orientation of bilayer high Co islands on Cu(111). (a) STM topography image, the majority of the Co islands exhibit blunt tips and have no perfect triangular shape. Imaging conditions: $V_{Gap} = -0.1$ V, $I_T = 1$ nA, $T = 8.3$ K. (b) Hard sphere model of Co islands on Cu(111) after [22]. The model shows the four possible orientations of the Co islands with respect to the underlying substrate. In the first Co layer the long edges of the islands always form a {100} microfacet with the Cu(111) lattice.

The crystallography of Co islands on Cu(111) was recently investigated by Monte-Carlo simulations [22], and the authors proposed a structural model for the islands, which is presented in Figure 3.7(b). The calculations suggest that the first Co layer forms {100} microfacets with the underlying Cu(111) surface at the long edges of the islands. The corners are forming {111} microfacets in the first Co layer. For the second Co layer the calculations do not predict a preference for one crystallographic orientation. Hence, four different layer stackings are possible for the bilayer high Co islands. These four configurations are illustrated in Figure 3.7(b) and can be classified in terms of faulted or unfaulted stacking order. The fcc stacking of the Cu(111) substrate follows an ABCABCABC order. Islands with an ABCAB and ABCAC stacking are therefore identified as unfaulted islands, since the first Co layer (A) continues the fcc stacking order (ABC). Consequently islands with ABCBA and ABCBC stacking are called faulted islands, since the first layer (B) does *not* continue the fcc stacking. Sometimes the stacking order of the islands is referred to as hcp and fcc, where fcc corresponds to unfaulted stacking (they continue the Cu(111) fcc stacking) and hcp to faulted stacking. However, in this thesis only the terms faulted and unfaulted are used. The authors of [22] find that the probability for the formation of unfaulted islands is 0.65, whereas faulted islands form with a probability of 0.35. With the help of this information the crystallographic orientation of the islands studied in this thesis was identified by a statistical analysis of large scale STM images (not shown).

The second system is Co on Cu(110)-p(2×3)N, it was first described by Leibsle et al. [32] and has been further explored by Ma and coworkers at the MPI in Halle [35]. The initial preparation step is the cleaning of the Cu(110) substrate. The same procedure as applied to Cu(111) is used here. The second step concerns the preparation of the nitrogen network on top of the cleaned surface. Two different approaches to achieve that goal have been reported. One approach is to bombard the surface with N^+ ions (600 eV) while keeping the Cu crystal at a temperature of 700 K [35]. The second idea is to first bombard the crystal with N^+ ions (500 eV) and to perform a subsequent annealing to $500 - 600$ K [33, 34, 73]. In this work the first method is applied and the crystal is sputtered with N^+ ions of 600 eV for 30 minutes at a temperature around 550 K. This time the sample plate is not heated via electron bombardment, but through heat radiation from the filament behind it. The preparation temperature is defined by the nitrogen desorption temperature which is in the range of $750 - 800$ K. Reliable preparation of the Cu$_3$N network is achieved at 200 K below the desorption point.

The final step, after successful preparation of the Cu$_3$N network on the Cu(110) surface, is the growth of Co nanowires on top of the network. It was shown by Ma and coworkers that it is possible to produce well separated wire-like structures with very high length-to-width ratios (up to 100) from a variety of metals such as Fe, Pd, Au [35] and Co [34] on this surface. It was found that the wires form upon room temperature deposition via self assembly. We follow that idea and deposited a small amount of Co onto the Cu nitride substrate. Figure 3.8 shows two constant current STM images of the resulting Co nanowires on Cu(110)-p(2×3)N.

In 3.8(a) an overview image of the Cu$_3$N network is shown, the elongated bright structures are the Co wires. Fig. 3.8(b) shows another terrace of Cu$_3$N with Co wires. The line-scan perpendicular to the Co wires reveals a separation between the Cu$_3$N rows of 1.15 nm. Ma proposed a structural model for the Cu(110)-p(2×3)N surface [35] with the unit vectors $a = 0.51$ nm and $b = 1.09$ nm. In the same work the minimum separation
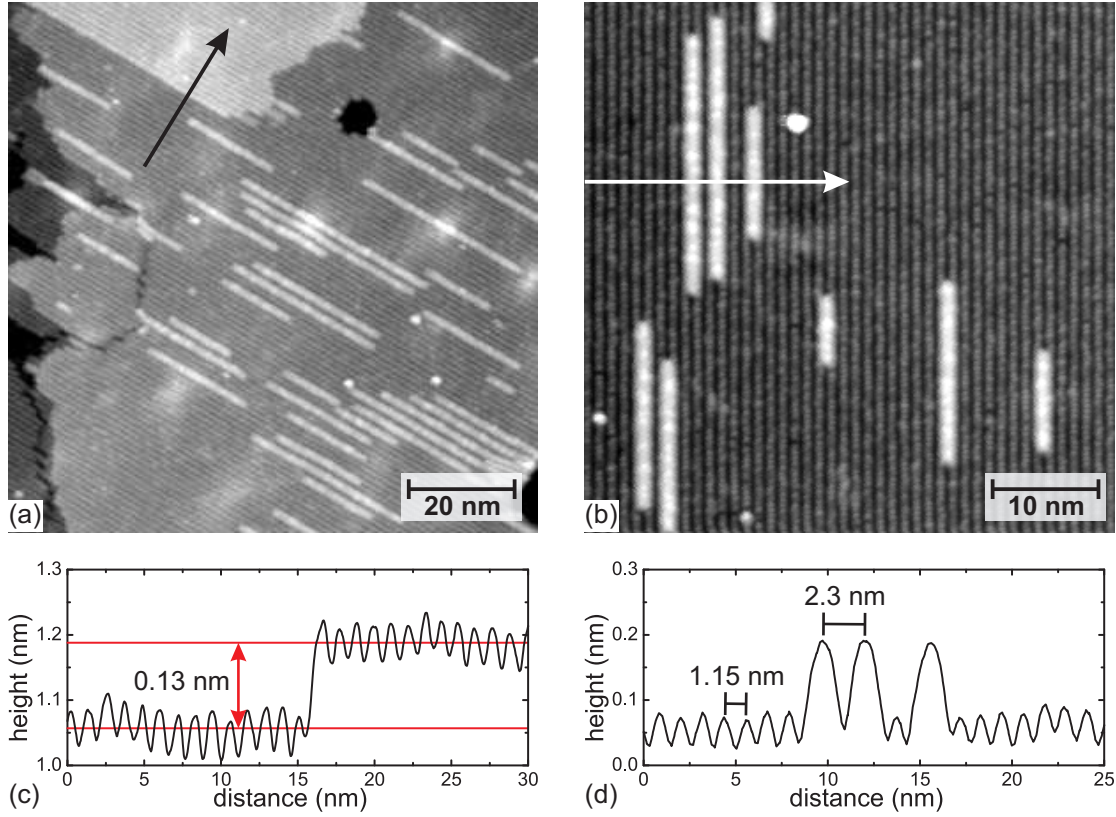
Figure 3.8: STM topography image of Co wires grown on a Cu$_3$N network on Cu(110). Imaging conditions: (a) $V_{Gap} = -0.5$ V, $I_T = 1$ nA, $\phi = 30°$. (b) $V_{Gap} = -1.3$ V, $I_T = 1$ nA, $\phi = 90°$. (c) Line scan along the black arrow in (a). The apparent height of the Cu$_3$N patch is 0.13 nm. (c) Line scan along the white arrow in (b). Co wires are separated by 2.3 nm and the distance of the Cu$_3$N rows is 1.15 nm. ϕ...angle of rotation with respect to the normal scanning direction.

of Co wires grown on Cu$_3$N is reported to be 2.2 nm. The line-scan of Fig. 3.8 suggests a value of 2.3 nm. In the upper left corner of image (a) an elevated patch of Cu$_3$N is visible. The line-scan in (c) reveals a step height of the patch of 0.13 nm. The height of monoatomic steps on the Cu(110) surface is 0.255 nm, as calculated from the lattice constant of copper of 0.361 nm [74]. This is almost double the height observed for the Cu$_3$N patch, suggesting that this step does not correspond to a Cu(110) step.

In summary the morphology of the Cu$_3$N surface and the Co wires grown on top of it is very similar to the structure reported by Ma and coworkers [35]. Detailed results on the structural and electronic properties of this system are presented in chapter 5 and discussed in section 6.5.

Tip preparation

The preparation of tips used in this work is a two step process which consists of ex-situ and in-situ treatments. The first step is an ex-situ etching process. All tips used in this work have been produced from annealed polycrystalline W wire (Alfa Aesar, 99.95%, $d = 0.375$ mm) by electrochemical etching in 8% sodium hydroxide solution. Detailed
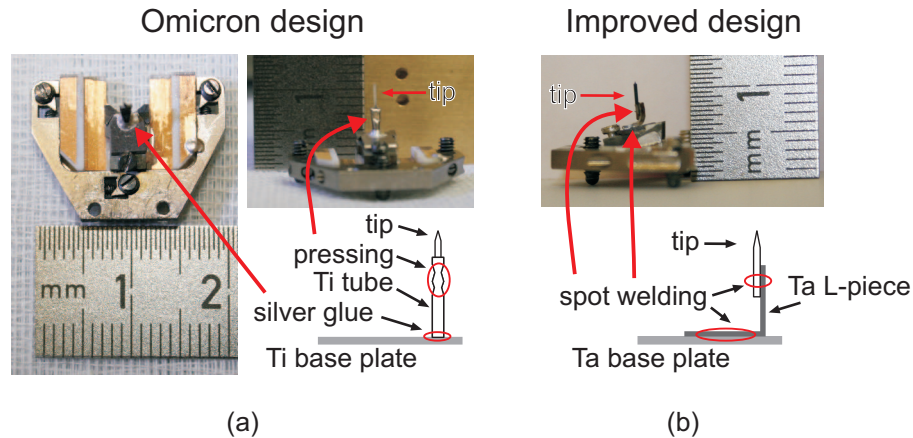
Figure 3.9: STM tip holder with two different tip mountings. (a) Original Omicron design as delivered. The tip is mounted within a Ti tube by pressing together the tube after inserting the tip. The tube is mounted to a Ti base plate by silver glue. (b) Our improved design. The tip is rigidly connected to a Ta L-piece and a Ta base plate by spot welding. Our improved design on the right has a much higher mechanical and thermal stability than the original Omicron design on the left. The original Omicron setup is not usable for tip annealing, it disintegrates upon flashing the tip. The design of (b) survives numerous tip heating cycles reliably.

descriptions of this standard procedure can be found in various text books [40–42, 75]. In this work all tips have been produced by the so-called lamella etching technique. A piece of W wire is mounted to a holder (anode) and is then placed in the center of a ring of 99.95% Pt wire (cathode). The ring with the W wire in the middle is then dipped briefly into the NaOH solution, which is producing a lamella of liquid within the ring. Now a positive voltage is applied between the ring and the W wire and the etching starts. Here, a commercially available device from Omicron [76] has been used to control the etching process. The device controls voltage and current during the etching process and switches off the voltage at the end of the etching as soon as the lower part of the wire drops off. It is argued that this might be favorable for getting a sharp tip apex [40].

After etching, tips are mounted on a tip holder and are subsequently introduced into the UHV chamber via the load lock. Figure 3.9 shows a tip holder where tips are mounted in two different ways. The original design by Omicron is shown on the left (a). The tip is placed in a Ti tube and fixed by pressing the tube, clamping the W wire, as shown. This setup has several disadvantages. Firstly, the pressing process is not very controlled and does not always guarantee a secure fixation of the tip. Secondly, the tube itself is mounted to a baseplate only by silver glue. This connection is mechanically and thermally instable and does not reliably survive annealing the tip in vacuum. The right side (b) shows our improved design to overcome this issue. Now the tip is spot-welded to a Ta L-piece, which is spot-welded to a Ta base plate. The spot-welding leads to a very rigid connection which has a much higher mechanical and thermal stability. This new design has proven to endure the in-situ annealing of the tip routinely and was used for all preparations.

The aim of ex-situ preparation are tips with a sharp apex. As the etching is performed in air it can be expected to lead to chemical contamination of the tip with oxides and other compounds. Such impurities are expected to lead to unstable tunneling conditions
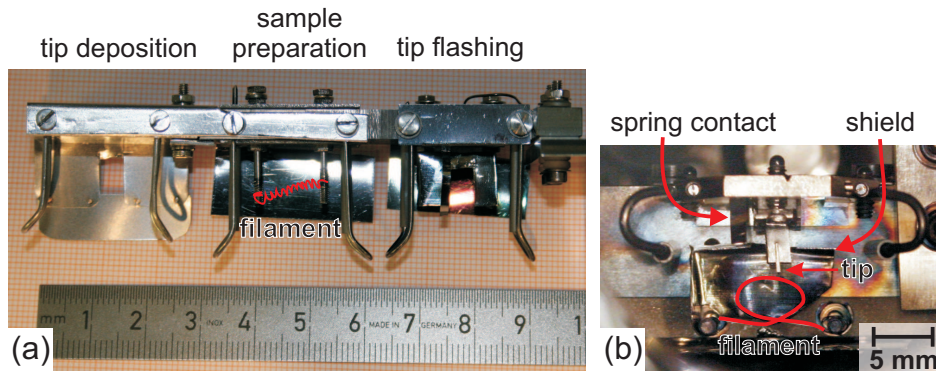
Figure 3.10: Customized heating stage. (a) Sample and tip heating stages mounted at the end of the transfer rod. (b) Tip holder in the heating stage insight the preparation chamber as seen through the view port.

in STM and hence spectroscopic measurements under such conditions are very demanding if not impossible. Indeed, we find that no stable imaging and spectroscopy can be achieved with an as-etched tip. The issue can be resolved by in-situ preparation. All tips used in this work have been heated in UHV to $\approx 2100°$C for $1 - 2$ seconds. This so-called flashing of the tip is performed by electron bombardment heating in a customized heating stage mounted on the transfer rod of the preparation chamber. Figure 3.10 shows the end of the transfer rod with three reception stages for tip and/or sample holders. The one in the middle is solely used for annealing the sample and the one on the right for flashing the tip. Fig. 3.10(b) shows a tip holder in the flashing stage. The filament used for heating is emphasized by a red line. The tip mounted on the L-piece is clearly visible, it is pointing towards the filament. A metal sheet is shielding the tip holder from heat radiation. For flashing the tip, it is put on high voltage potential of +1200 V by the spring contact. This way electrons emitted by the filament are only accelerated to the tip, at an emission current of 25 mA. This ensures an efficient tip heating while keeping the rest of the tip holder cool. The temperature of the tip during flashing is checked by a W-hairpin pyrometer (Keller Mikro-Pyrometer PV11) through a viewport. The photo shown in fig. 3.10(b) was taken through this viewport.

Preparation of magnetic tips

To yield information about the magnetic properties of the sample, magnetic probe tips are required [9, 10, 77]. This chapter describes the macroscopic preparation procedures which are applied in order to obtain such tips. Tungsten tips, cleaned as described above, are covered with a magnetic material in-situ under UHV conditions. Deposition of material onto the tip is done on a special stage of the transfer rod. It comprises a shield which covers the complete tip holder. As shown in Fig. 3.10(a) a small opening in the shield ensures, that only the tip is covered with material. In this work tips have been covered with $20 - 100$ atomic layers (AL) of chromium[2].

Another option is the use of Cr bulk tips. The group of Li Bassi at the Polytecnico di Milano was able to establish a working preparation scheme [62], and currently, after the completion of this thesis, we use Cr bulk tips successfully in spin-STM studies. For

---

[2]Deposition rate has been calibrated by STM measurements on low coverages of Cr on Cu(111).
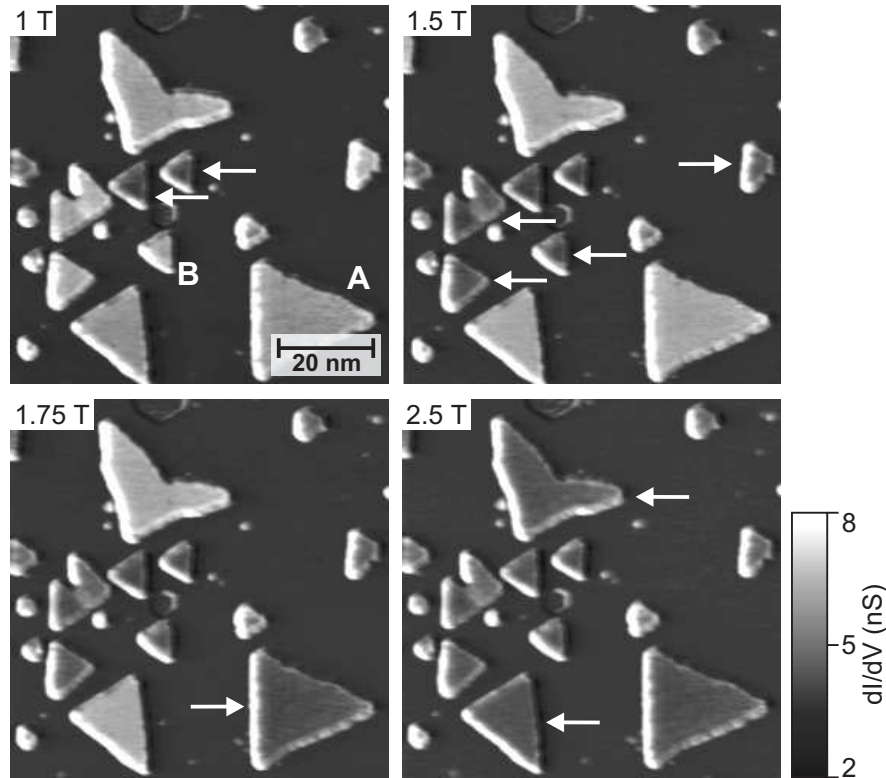
Figure 3.11: Magnetic switching of individual Co islands. dI/dV maps obtained with a magnetic tip (Cr/W)) at different external magnetic fields. White arrows mark islands whose magnetization is aligned parallel to the applied field (dark color). Imaging conditions: ($V_{Gap} = -0.51$ V, $I_T = 1$ nA, $T = 7$ K).

comparison also tips, which are first covered with 40 AL Co and subsequently with 40 AL Cr, are used here. The results presented in section 4.3.1 seem to indicate that Co might influence the dependence of the magnetization orientation of the tip on the external field, a detailed discussion of this issue is given in section 6.2.

One simple approach in order to test the magnetic sensitivity of the tips is the imaging of Co islands in spectroscopy mode while the magnetic state of the system is varied by an external field. The goal is to exploit that the dI/dV signal depends on the relative orientation of the magnetization directions of tip and sample, as described in numerous review articles and books [9, 40, 78]. Figure 3.11 presents a series of four dI/dV images taken with a Cr covered W tip at different magnetic field values. At a field of 1 T two small islands marked by arrows appear darker than the larger islands. Increasing the field to 1.5 T changes the color of four other islands from bright to dark. With further increasing magnetic field more and more islands change their color from bright to dark, until finally at 2.5 T all islands in the image exhibit a dark color. It can be concluded that, since only the external magnetic field is changing, the contrast change is due to the switching of the islands magnetization direction.

To ensure the magnetic origin of the contrast, we also measure single point spectra on single particles as a function of an external magnetic field. Hysteresis loops of single particles are thus extracted from this data at various voltages. Only these hysteresis loops

allow a rigorous disentanglement of tip and sample contributions to the measured data and a clear-cut determination of the magnetic state of the tip-sample system. The details of this approach are described and thoroughly discussed in sections 4.3.1 and 6.2.

Chapter 4

Electronic and magnetic properties of nanostructures on Cu(111)

This chapter presents the main experimental results of this thesis. It is divided into four sections. The first section 4.1 focuses on the electronic properties of the Cu(111) surface and electron confinement effects within a stripe of Cu on Cu(111). It is shown that an analysis of the energy dependent standing wave patterns within the stripe, which are due to electron confinement, yields the electron dispersion relation. This dispersion relation is quantized. In section 4.2 the electron confinement within triangular Co islands grown on Cu(111) is investigated. Applying the same analysis as mentioned above to the standing wave patterns within the Co islands yields again the dispersion relation, which is also quantized. The experiments presented in these two sections are all performed with non-magnetic W tips.

Sections 4.3 and 4.4 present spin-STM measurements on Co islands on Cu(111) utilizing magnetic tips. In section 4.3 our new method of measuring the magnetic switching field of single Co islands is introduced. This new method opens the way to study the island size and temperature dependence of the switching field of individual Co islands, as shown in subsection 4.3.2. A transition from the superparamagnetic state to the state of stable magnetization is observed, which is triggered by island size and temperature changes. Subsequently in subsection 4.3.3 results obtained on the position dependence of the electronic and magnetic properties within an individual Co island are presented. Distinct inhomogeneities of the electronic properties are found. The chapter closes with an investigation of spin-polarized electron confinement within Co islands, presented in section 4.4. Our observations reveal a pronounced spatial modulation of the dI/dV asymmetry within the islands, which is strongly related to the spin-polarization within the island.
All experiments are performed at 8.3 K, if not stated differently.

4.1 Electronic properties and confinement effects on Cu(111)

Figure 4.1(a) shows a constant current STM image of a stripe of Cu atoms on Cu(111). The Cu(111) surface was prepared as described in chapter 3, and a small amount of Co was deposited onto it. The stripe is observed after indenting the STM tip into the Cu
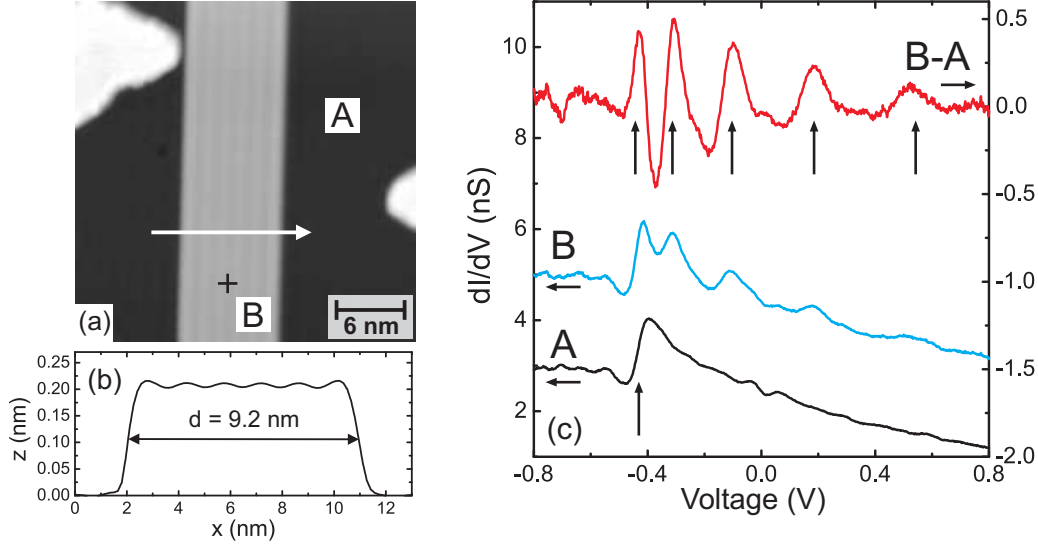
Figure 4.1: Stripe of Cu atoms on Cu(111) formed by tip indentation. (a) STM constant current image ($V_{Gap} = +0.05$ V, $I_T = 1$ nA). A and B mark positions where spectra are recorded. (b) Line scan along the white arrow in (a). (c) dI/dV spectroscopy performed on Cu(111) (A) and at the center of the stripe (B). The kink around -0.4 eV is a clear signature of the Cu(111) surface state. The difference between the two spectra (B-A) reveals pronounced peaks (marked by arrows). Spectrum B is shifted upward by 2.5 nS for clarity.

sample surface. Its formation can be understood as a mechanism to release the elastic stress induced by tip indentation. Step edges which are present on the surface during Co deposition are always decorated with Co (see section 3.2). The edges of the stripe do not show any decoration with Co. The missing decoration proofs that the observed structure is formed after Co deposition. The line profile in (b) reveals that the stripe is 0.2 nm high and 9.2 nm wide. Taking into account the lattice constant of Cu of $a = 0.361$ nm [74] the spacing of the (111) planes of Cu is $a\sqrt{3}/3 = 0.208$ nm, the nearest neighbor distance within a (111) plane is $a\sqrt{2}/2 = 0.255$ nm. Hence, the height of the stripe is one atomic layer and it is about 36 atomic distances wide.

The electronic properties of the system are investigated by dI/dV spectroscopy on both the stripe and the Cu(111) substrate. Figure 4.1(c) shows the average of 25 spectra measured on Cu(111) at positions close to the area marked A in (a). The prominent feature of the spectrum is a kink at -0.44 eV. This feature is identified as a signature of the Shockley surface state of Cu(111) [79, 80]. The blue curve in Fig. 4.1(c) is the average of 15 spectra measured on the stripe, exactly at position B marked by a cross in (a). To enhance the weight of the stripe electronic structure, spectrum A has been subtracted from the original data (red curve). The difference spectrum B-A exhibits several maxima indicated by the arrows, in contrast to the electronic structure of the Cu(111) substrate, where only a kink is observed.

This result might come as a surprise as both spectra are measured on pure copper. A closer look at the line profile in (b) and at the constant current image in (a) reveals a light spatial modulation within the stripe. It will be shown in the discussion (sec. 6.1), that these modulations are due to *electron confinement* [1, 2, 81, 82]. The observed wave
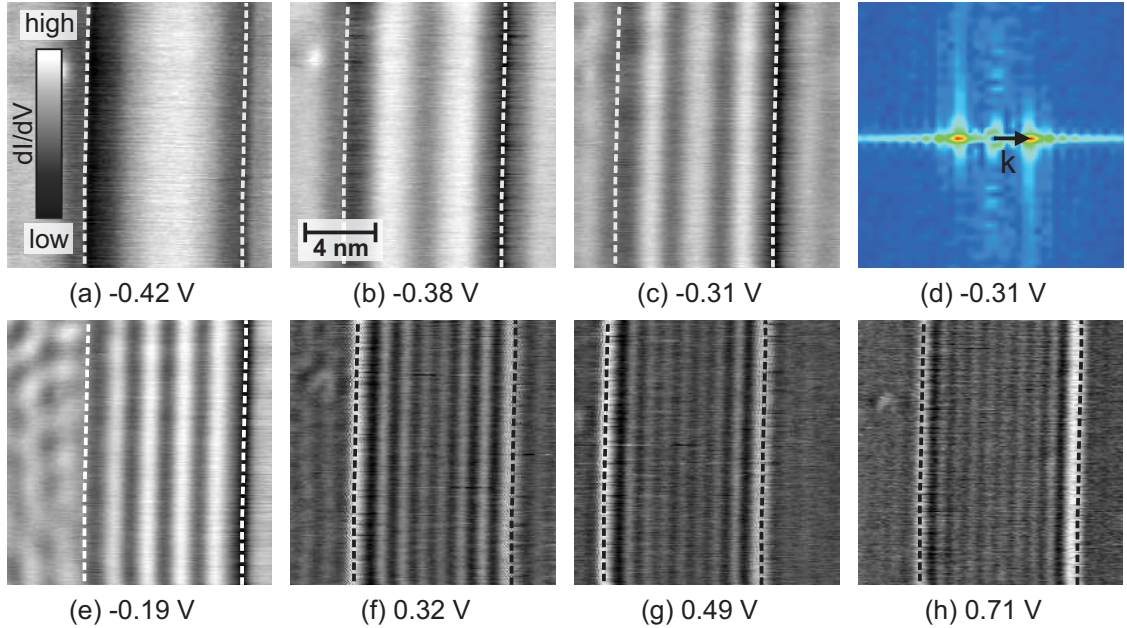
Figure 4.2: Spatially modulated dI/dV signal within a stripe of Cu on Cu(111). (a)-(c) and (e)-(h): dI/dV spectroscopy images at different bias voltages (15×15 nm^2, $I_T = 1$ nA). Dashed lines represent the width of the stripe as extracted from topography data. (d) Fast Fourier Transformation (FFT) map of the wave pattern in (c). From the FFT maps the electron wave-vector $\vec{k}$ is extracted.

pattern is ascribed to a spatially modulated LDOS within the stripe. The bias dependence of these modulation patterns is investigated in the following.

Fig. 4.2 shows a series of dI/dV maps of the Cu stripe obtained at different bias voltages. Pronounced modulations within the stripe are observed. The wave length of the modulation is steadily decreasing with energy. To investigate the energy dependence of the patterns in detail, a two-dimensional Fast Fourier Transformation (FFT) of the data is performed. As an example the FFT map of Fig. 4.2(c) is displayed in (d). Two intensity maxima are clearly visible. Note, that due to the nature of the FFT process, the resulting FFT maps (Fig. 4.2(d)) are always inversion symmetric[1]. The intensity maxima resemble the direction of the modulation in the dI/dV maps. The distance between the center of the FFT map and one maximum yields the wave-vector $\vec{k}$ of the standing wave pattern [83, 84].

Note, that the direct analysis of line scans through the dI/dV maps, by fitting the data with sine and cosine functions, not shown here, yields the same wave-vectors as the FFT analysis. The equivalence of the FFT analysis and fits with analytical solutions of the quantum mechanic problem of electron scattering at a step edge has also been demonstrated for step edges on Cu(111) [85]. The advantage of an FFT analysis over a direct analysis of line scans is, that the FFT analysis can be applied to virtually any geometrical shape (see e.g. section 4.2) and that there is no need for solving the scattering problem related to the investigated shape.

The FFT analysis is utilized to obtain the energy dependence of the wave-vector $\vec{k}$.

---

[1]The intensity I in the FFT maps obeys the following symmetry: $I(k_x, k_y) = I(-k_x, -k_y)$.
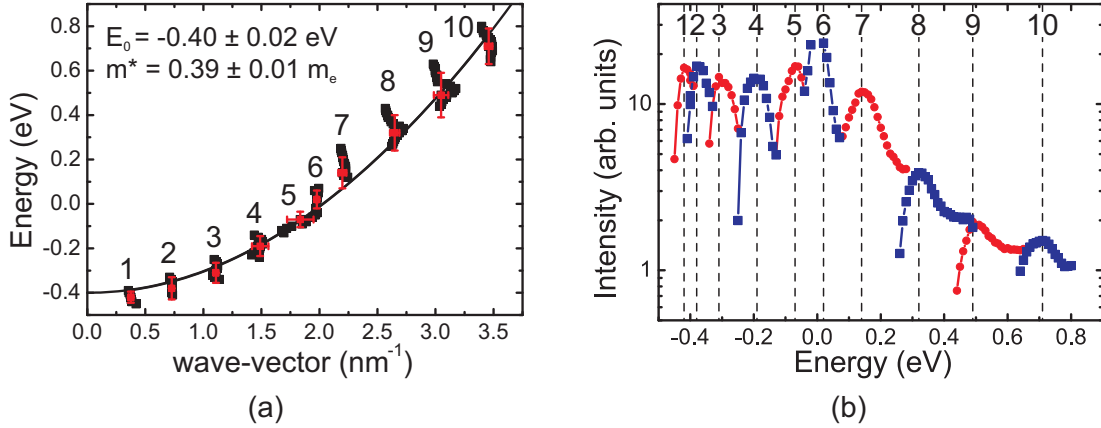
Figure 4.3: (a) Step-like dispersion relation of the Cu(111) surface state electrons extracted from the FFT analysis of dI/dV spectroscopy maps. Red data points mark center and energetic width of the quantized states as extracted from (b). Their x-coordinates are the averaged wave-vectors for each group of data points. A parabolic fit through all data points (solid line) yields E_0, and the effective electron mass m^*. (b) Intensity evolution of the peaks in the FFT maps as a function of energy. Dashed lines mark intensity maxima of the different states.

More than 100 dI/dV maps similar to those in Fig. 4.2 have been recorded in a bias range of -0.45 to $+0.85$ V and are analyzed by FFT. The resulting relation $E(\vec{k})$ is presented in Fig. 4.3(a). The most remarkable result is that the data points are grouped at certain positions of the $\vec{k}$-scale and that some $\vec{k}$-values are not observed. This is a clear signature of a quantization of $\vec{k}$. For a free electron gas a continuous parabolic dispersion would be expected [86]. Note that the experimental $E(\vec{k})$ data follow a parabolic shape. As will be outlined in the discussion in section 6.1, assuming a free electron like behavior, the parabola can be described by $E(\vec{k}) = E_0 + \frac{\hbar k^2}{2m^*}$, and the solid line through the data points gives:

$$m^* = 0.39 \pm 0.01 \ m_e \qquad E_0 = -0.40 \pm 0.02 \ eV$$

where m_e is the electron mass.

In addition to the position of a maximum in a FFT map, which yields the wave-vector $\vec{k}$, its peak intensity is also extracted here. Figure 4.3(b) represents the evolution of the FFT peak intensities of $\vec{k}$ as a function of energy. The FFT intensity exhibits a series of peak-like structures, which are colored alternately in blue and red for clarity. Each of the peak structures corresponds to a group of wave-vectors. Numbers on the peaks correspond to the clusters of data points in Fig. 4.3(a). It is discussed later in section 6.1 that the peak centers marked by dotted lines identify the eigenstates of the confined system. Note, that peak intensities shown in Fig. 4.3(b) are constant at negative energies but decay with increasing positive energy. Furthermore the data points in Fig. 4.3(a) which are close to zero bias (group 5) show a much wider distribution of wave vectors than the rest of the data. These observations suggest, that the scattering properties of the system might change as a function of energy. A detailed discussion of this issue is presented in section 6.1.
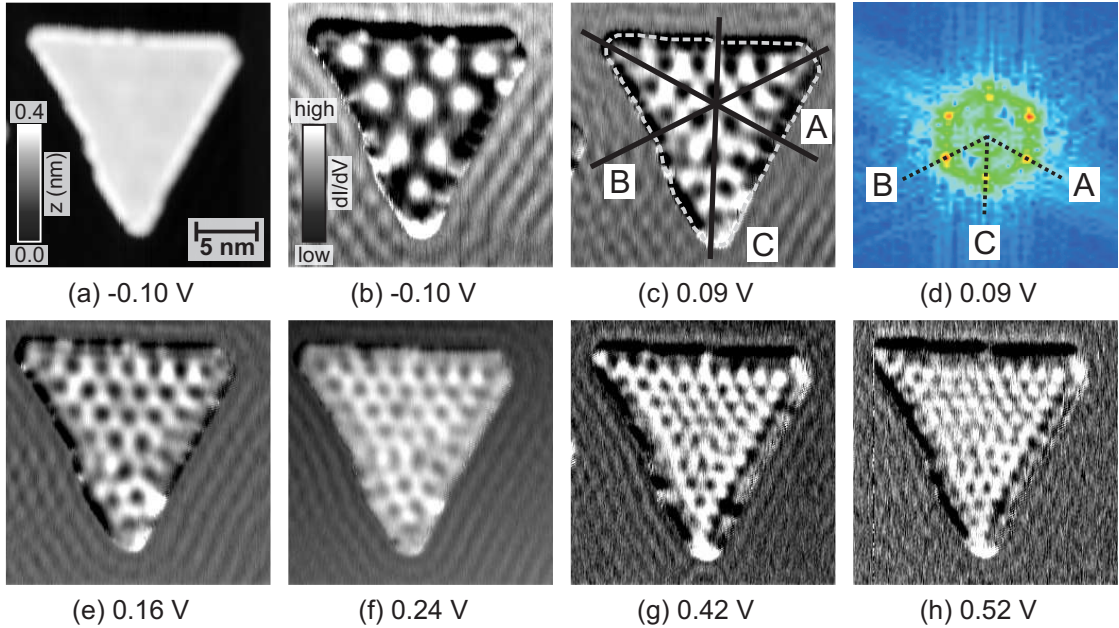
Figure 4.4: Spatially modulated dI/dV signal within a Co island on Cu(111). (a) STM topography image. (b),(c),(e)-(h): dI/dV spectroscopy maps at different bias voltages (22×22 nm^2, $I_T = 1$ nA) where (b) is measured simultaneously with (a). Solid black lines in (c) show the three heights of the triangular island. The dashed gray line represents the perimeter of the island as extracted from topography data. Dashed black lines in (d) show where the directions A-C appear in the FFT map of (c).

4.2   Electron confinement within Co islands

This sections presents the results on electron confinement effects within triangular two atomic layers high Co islands grown on Cu(111). Figure 4.4(a) shows a constant current STM image of the investigated island. The island has the shape of an almost equilateral triangle with a base length of about 18 nm. A series of dI/dV maps recorded at different V_{Gap} is presented in (b)-(c) and (e)-(h). Again pronounced modulation patterns within the island are observed[2]. These patterns become more complex with increasing energy, similar to the results of the copper stripe presented above in section 4.1. Here we focus on measurements with a W-tip in zero field. Later in section 4.4 measurements in an external magnetic field and with a magnetic tip are presented, which reveal spin dependent modulation patterns.

The appearance of the patterns is ascribed to the confinement of surface state electrons within the island. This phenomenon has been reported in a previous STM work by Diekhöner et al. [23], however, a detailed investigation of the quantization effects was missing so far and is presented here. Fig. 4.4(d) shows the FFT map of (c). The three symmetry axes of the triangle A, B and C are highlighted in both images. The FFT map

---

[2]In the as-prepared state the islands often do not exhibit the spatial modulation patterns presented in Fig. 4.4. We found empirically that the patterns become visible after imaging the island once at 30 nA and +1.5 V. Recently is was revealed that the absence of the modulation patterns can be ascribed to a layer of hydrogen adsorbed on the islands [87]. The same work states that hydrogen desorption is induced by the tunneling electrons when $I_T > 18$ nA and $|V_{gap}| > 0.5$ V.
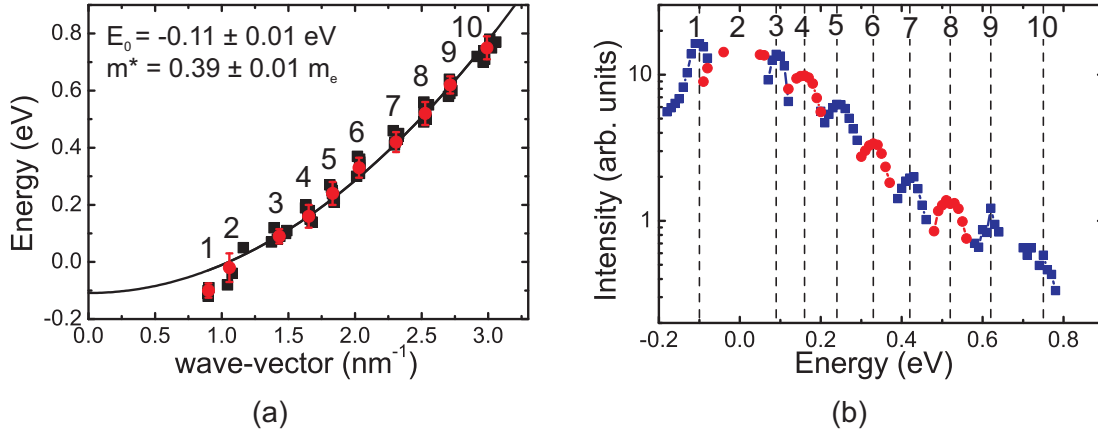
Figure 4.5: (a) Discrete dispersion relation of the Co surface state electrons along direction B. Red data points mark the center and energetic width of the quantized states as extracted from (b). Their x-coordinates are the averaged wave-vectors for each group of data points. A parabolic fit through all data points (solid line) yields the onset E_0 of the surface state and the effective electron mass m^*. (b) Intensity evolution of the peaks in the FFT maps as a function of energy. Dashed lines mark the intensity maxima of the different states.

exhibits six intensity maxima arranged in a hexagonal shape around the center of the map. Each pair of opposite maxima, which are symmetric about the center of the map, corresponds to one of the symmetry axes. Hence, the wave-vectors of the wave patterns can be extracted for each direction separately. It has to be noted, that this is the first time that wave-vectors are extracted for different directions separately. In previous work, only a radial average of the Fourier spectrum was used to determine $\vec{k}$.

The FFT analysis of approx. 90 dI/dV maps in the bias range of -0.18 to $+0.78$ V yields three dispersion relations for the different directions. The result of direction B is presented in Fig. 4.5(a). As for the case of the Cu stripe the data points are clustered at discrete $\vec{k}$-values and the dispersion is clearly discontinuous. The solid curve reflects a parabola with:

$$m^* = 0.39 \pm 0.01 \ m_e \qquad E_0 = -0.11 \pm 0.01 \ eV.$$

Note that the parameter E_0 of -0.11 eV differs from that of -0.44 eV of Fig. 4.3(a) extracted for Cu. The link between the energy offset of the parabolic fit and the dispersion relation of surface state electrons on both Cu and Co is discussed in section 6.1.

Fig. 4.5(b) shows the FFT intensity as a function of energy. A set of peak like structures is observed, where each of the alternately colored peaks belongs to a cluster of data points in the dispersion relation. Numbers on the peaks correspond to the clusters of data points in Fig. 4.5(a). It is striking that the amplitude of the peaks is rather constant for energies smaller than $+0.1$ eV but drops significantly for larger energies. On the other hand the width of the peaks does not exhibit significant changes across the investigated energy range. These findings are very similar to the observations made for the Cu stripe and suggest a general mechanism, that is applicable to both systems. A detailed discussion of these issues is presented in section 6.1.

4.3 Magnetic switching field of individual Co islands

This section presents the results concerning the magnetic properties of individual Co islands on Cu(111). First the method of measuring the switching field of a single island will be described. The second part reveals the dependence of the switching field on island size and temperature. In section 4.3.3 the spatial dependence of field dependent spectroscopy within a single Co island is explored. Section 4.4 presents maps of the dI/dV asymmetry of Co islands with different magnetization states, which are analyzed in the discussion of section 6.4 to extract the spatial modulation of the spin polarization of the islands.

Cobalt islands on Cu(111) have been studied before by SP-STM [16, 88, 89]. These works focused mainly on *imaging* ensembles of Co islands with a magnetic tip. It was demonstrated that the orientation of the easy magnetization axis is parallel to the surface normal. A switching field of the Co islands of the order of $1-2$ T has been reported. However, a detailed study of the magnetic switching of *individual* islands is still missing. Such a study is extremely important, as it offers insight into e.g. the magnetization reversal process by analyzing the size and temperature dependence of the switching field of individual islands. In this work we utilize the spectroscopic capabilities of STM in combination with its spatial resolution to investigate the magnetic properties of *individual* Co islands with spatial resolution within one island.

4.3.1 Field dependent scanning tunneling spectroscopy

Before the switching field of individual Co islands is discussed, we describe important novel insight into the behavior of the STM tip in an external magnetic field.

In section 3.2 the macroscopic preparation of magnetic tips has been described. One might expect that this preparation directly ensures magnetic sensitivity of the tips routinely. This is, however, not the case. Therefore an additional microscopic preparation under tunneling conditions is applied [90]. This comprises the application of voltage pulses between tip and sample, which are performed over clean Cu(111), away from the area of interest. It is found that voltage pulses from $+5$ to $+8$ V with a duration of a few milliseconds are suitable. Before applying the pulse, the tunnel current is increased from 1 nA, used for imaging, to 30 nA. Subsequently the feedback loop is switched off for the duration of the pulse. Significant changes in the dI/dV spectra may be caused by this procedure. To evaluate the outcome of this microscopic preparation, spectra are measured on both the Cu(111) substrate and the Co islands. Only tips showing both a clear signature of the Cu(111) surface state at -0.44 V and a clear Co related peak at -0.3 V are considered for further use in the experiments.

The general approach to spin-STM, as briefly described in section 3.2, has a number of deficiencies which call for an advancement of the technique. Most importantly several spin-STM studies use the assumption that a high dI/dV signal identifies a parallel (P) orientation of the magnetization directions of tip and sample and that a low signal corresponds to an antiparallel (AP) orientation [16–18]. However, this assumption is not always fulfilled and the authors seldom provide evidence for this assumption. Furthermore contributions of the tip to the measured signal are either postulated or even neglected completely. However, without a sound knowledge of the tip contributions it is hard to draw reliable conclusions about the properties of the sample. To overcome these difficulties and to disentangle tip and sample contributions to the observed contrast, the following approach is introduced in this work.
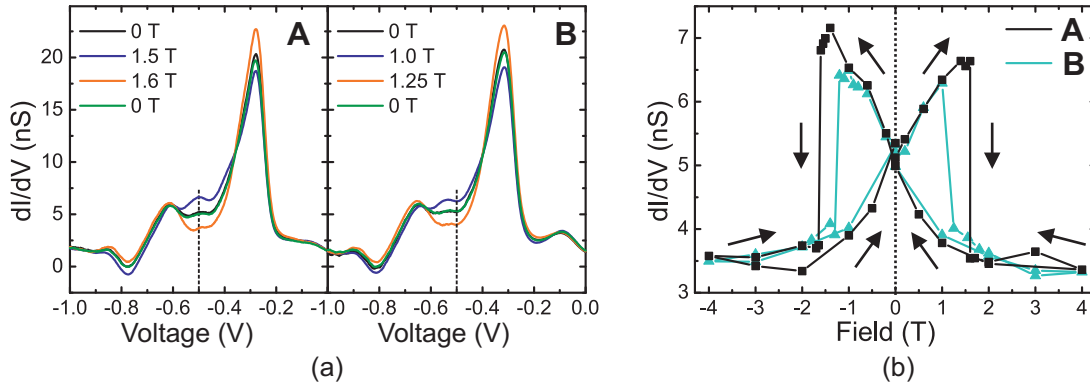
Figure 4.6: (a) Single Point dI/dV spectra taken at the centers of islands A and B marked in Fig. 3.11 at different magnetic fields. The spectra show clear changes as a function of field. (b) Loops of the dI/dV signal extracted from a series of spectra measured on both Co islands. Both loops are extracted at $V = -0.5$ V, as marked in (a). Arrows indicate the sequence in which the data are recorded.

We record dI/dV spectra on single Co islands during a complete cycle of the magnetic field. From this spectroscopic data, dI/dV hysteresis loops of individual islands are extracted, which allow a clear-cut unambiguous determination of P and AP states. In Figure 4.6(a) dI/dV spectra measured on islands A and B from Fig. 3.11 on page 25 are presented. The spectra of both islands exhibit distinct changes of shape and amplitude as the external field is varied. These changes are ascribed to a modification of the relative orientation of tip and island magnetization direction, as discussed in section 6.2. To understand the way the signal changes with field, the dI/dV signal is plotted at a fixed bias as a function of the applied field [91]. The result is a hysteresis loop of the studied particle as shown in Fig. 4.6(b).

Both plots are symmetric with respect to the field and both show a clear hysteresis. For example at ±1 T the dI/dV signal has two different values, depending on the history of the magnetic field. The two plots resemble the shape of so-called butterfly curves, which are well known from tunnel magnetoresistance (TMR) measurements [92]. For field values smaller than a critical value the signal changes continuously, whereas an abrupt change is observed at this critical point. The critical fields are ±1.625 T for island A and ±1.250 T for island B. It is shown later in the discussion of section 6.2, that the continuous change of signal between the critical fields is due to a field-induced reorientation of the magnetization direction of the tip. The points where the dI/dV signal changes abruptly mark the critical field that is needed to align the island magnetization direction parallel to the external field. This field is called the switching field of the island, H_{sw}.

One might be tempted to assume that tips covered with Cr always exhibit a similar behavior in field. This assumption is immediately disproved by the hysteresis loops shown in Figure 4.7. These loops have been obtained on different islands with different tips. The loops presented in (a) and (b) are both measured with Cr covered tips. Still they exhibit very different shapes. Whereas the loop in (a) is very similar to the results presented above, the loop in (b) shows an asymmetric shape without significant signal changes between the two critical field points. This is ascribed to a fixed tip magnetization direction. Green and red arrows mark the two possible magnetization configurations. The third loop in (c)
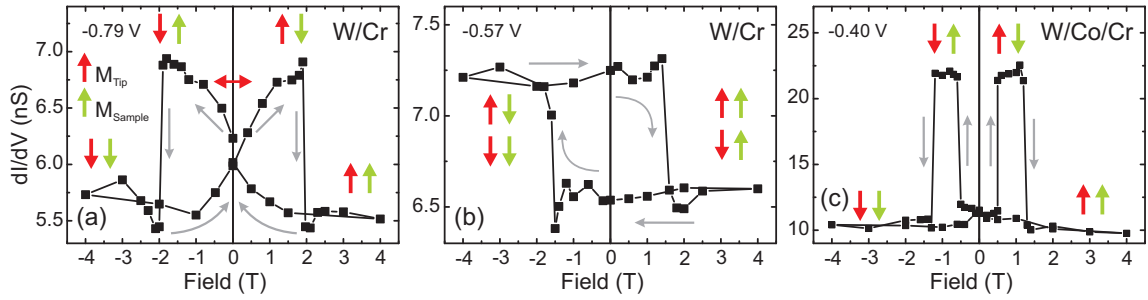
Figure 4.7: Hysteresis loops of the dI/dV signal measured at the center of different Co islands at 8.3 K. The abrupt changes of the signal mark the switching of the magnetization of either the tip (red arrow) or the Co island (green arrow). Grey arrows mark the time sequence of the field sweep.

shows yet another shape. Here two abrupt changes of the signal are observed, which can be ascribed to a switching of the tip at low fields and a switching of the island at higher fields. Note, however, that this tip is covered first with 40 ML of Co and then with 40 ML of Cr.

These results clearly demonstrate the importance of performing full cycles of the magnetic field in order to obtain a reliable characterization of the magnetic configuration of the tip. Since only a precise knowledge of the magnetic properties of the tip allows for drawing reliable conclusions about the magnetic properties of the sample. A detailed discussion of this issue will be given in section 6.2. In combination with the lateral resolution of STM the new approach to spin-STM presented here marks an important progress for the reliable study of the magnetic properties of single particles.

4.3.2 Size and temperature dependence of the switching field of individual Co islands

In this section the method of obtaining the switching field H_{sw} of an individual particle described above (see section 4.3.1) is used to extract the size and temperature dependence of H_{sw}. Figure 4.8 presents a compilation of six hysteresis loops. Loops (a) to (c) are recorded on three different islands with different sizes but at the same temperature. Loops (d) to (f) are obtained on one and the same island at three different temperatures. All loops have an asymmetric shape, indicating a fixed orientation of the tip magnetization.

A close look on Fig. 4.8(a)–(c) reveals that the switching field depends on island size. The loop of a 650 atoms small island presented in Fig. 4.8(a) measured at 8.3 K does not exhibit hysteretic behavior. Loops (b) and (c) reveal a switching field of 2 T for a size of 5600 atoms and 1.6 T for 21200 atoms. Note, that the increase of H_{sw} is not monotone with increasing size. The loops shown in (d)–(f) illustrate, that the switching field also depends on temperature. The switching field of an island with 1010 atoms drops with increasing temperature from ± 0.25 T at 7.6 K to ± 0.15 T at 8.3 K and finally at 12.0 K the curve becomes nonhysteretic.

Figure 4.9 combines the switching field data of ≈ 60 individual Co islands and is one of the main experimental results of this work. The plot of the switching field as a function of island size is separated into three regimes. Islands smaller than ≈ 1100 atoms in regime I do not show hysteresis. Medium sized islands of regime II in the range of 1100 to 7500
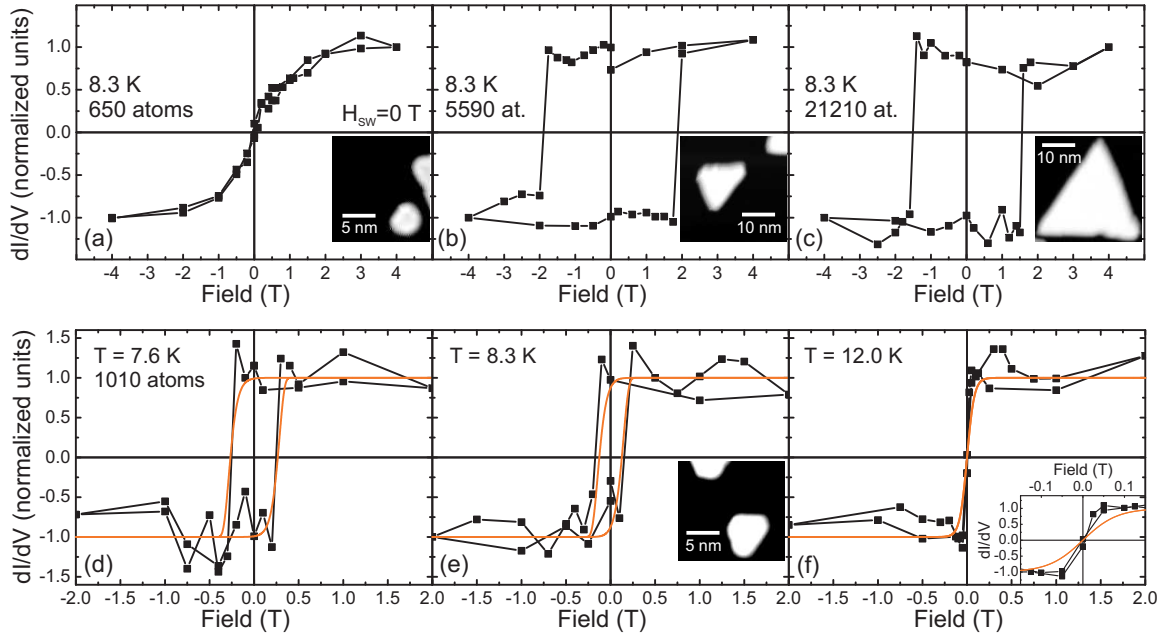
Figure 4.8: Size and temperature dependence of the switching field. (a)-(c) Hysteresis loops of *three different* islands recorded at the same temperature. The loops correspond to the three size dependence regimes denoted in Fig. 4.9. (d)-(f) Hysteresis loops of *one individual* Co island with a size of 1010 atoms recorded at different temperatures. Orange solid lines are guides to the eye. Insets show STM topography images of the studied islands ($V_{Gap} = -0.1$ V, $I_T = 1$ nA).

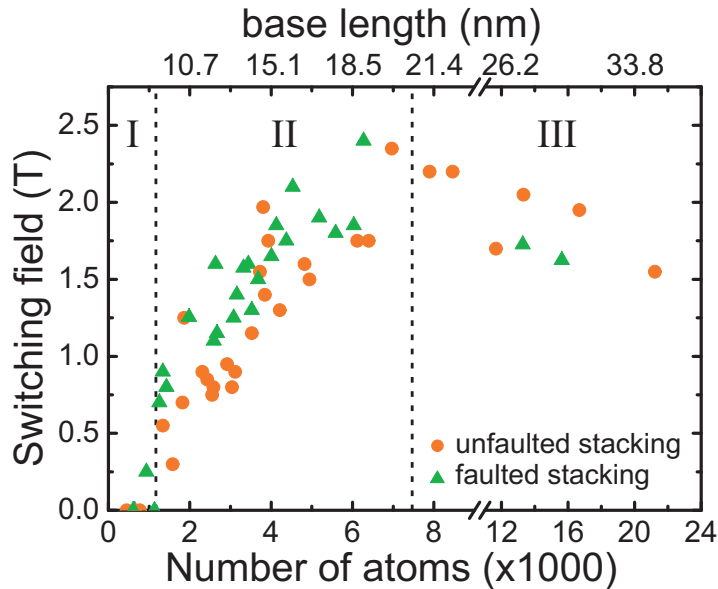Figure 4.9: Size dependence of the switching field of individual Co islands on Cu(111). Every data point marks the switching field of one individual Co island. The two possible orientations of Co islands on Cu(111) are plotted with different color and symbol. The data are divided into three regimes: I) Unhysteretic behavior, i.e. $H_{Sw} = 0$. II) Monotone increase with island size. III) Monotone decrease with island size.

atoms exhibit a monotone increase of the switching field with size. The largest islands within this size range reach switching fields of up to 2.4 T. For even larger islands in regime III with $N > 7500$ atoms switching fields decrease monotonic with size.

The data compilation in Fig. 4.9 distinguishes between unfaulted and faulted islands, this distinction is based on work by Negulyaev and coworkers at the MPI Halle [22]. Their theoretical study reveals that Co islands on Cu(111) grow either in a faulted or unfaulted stacking with respect to the Cu substrate. Both species are identified in STM images from the different abundance of their occurrence. From their kinetic Monte-Carlo simulations the authors conclude a ratio of 0.65 to 0.35 for the relative abundance of unfaulted and faulted islands, respectively. Here, a statistical analysis of large scale STM images is used to identify the orientations of the islands[3]. Figure 4.9 shows a systematic difference in switching field for the two crystallographic orientations. In regime II unfaulted islands exhibit on average smaller switching fields than faulted islands. In regime III the opposite is observed. This observation suggests, that the magnetocrystalline anisotropy differs for both species, as discussed in section 6.3.

4.3.3 Position dependence

This section is dedicated to the investigation of the position dependent electronic properties of individual Co islands. Until now hysteresis loops have been extracted from single point spectra taken at the center of the islands. A possible spatial variation of the studied properties cannot be excluded, and corresponding spatially resolved measurements are presented here. In a previous work Rusponi et al. [29] studied the magnetic properties of large ensembles of Co islands on Pt(111). The authors concluded that the rim atoms of a Co island on Pt(111) exhibit a dramatically changed magnetic anisotropy. A detailed study of the spatial dependence of the hysteresis loops is therefore also conducted.

Figure 4.10 shows four dI/dV spectra measured with the same tip and under the same tunneling conditions at four different positions on one Co island. A STM topography image of the island is shown as an inset in Fig. 4.10. Positions where the data were obtained are marked by black dots on a white line. Spectra 2 and 3, measured close to the center of the island, exhibit a pronounced peak at -0.3 V which is ascribed to a d-like surface state [23]. In contrast, spectrum 1, obtained very close to one of the corners of the triangular island, shows a different shape. The peak is strongly suppressed and shifted to a lower energy of -0.4 V. Spectra closer to the rim (spectrum 4) show even more pronounced changes. Spectrum 4 is taken directly on the edge of the island and reveals the appearance of a new peak close to the Fermi energy. This new peak only exists at the rim of the islands and was ascribed to an electronic rim state in a previous work [89]. The peak at -0.3 V observed in the other spectra completely vanished. The significance of these findings is discussed in section 6.3.1 below.

---

[3]Alternatively STM images with atomic resolution on both the Co islands and the Cu(111) substrate could in principle be used to identify the stacking of the Co islands. However, to obtain such data is experimentally very challenging and we did not succeed to obtain atomic resolution on both substrate and island simultaneously. Here we focused rather on spectroscopic than on resolution issues. In previous work the energy position of the d-like Co peak was used to identify the stacking order [16]. Recently it was demonstrated that the energy position of this peak also depends on the island size [24]. Thus, the identification of the stacking order by spectroscopy measurements also requires a statistical analysis of a large number of spectra measured on islands with different sizes. To identify the stacking order of Co islands on Cu(111) by a statistical analysis of large scale constant current images is therefore the simplest but still reliable approach.
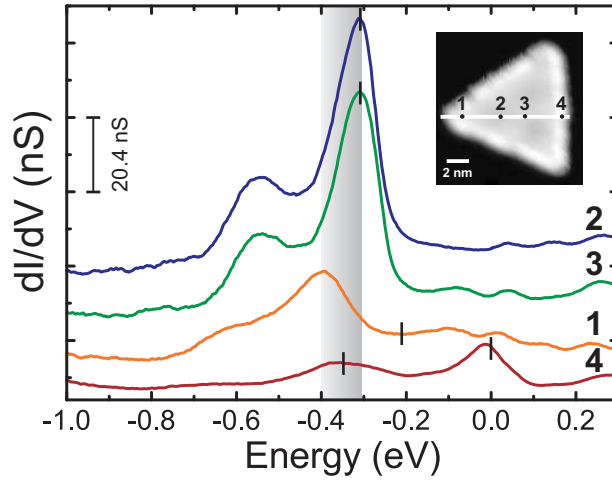
Figure 4.10: dI/dV spectra measured at four different positions on one Co island (Inset: STM topography image with $V_{Gap} = -0.1$ V, $I_T = 1$ nA.). Close to the rim of the island the dominant peak shifts to a lower energy, as depicted by the gray shaded area. At the rim the peak vanishes and a new peak appears around the Fermi energy. Spectra are shifted vertically for clarity. The markers indicate the energies at which the hysteresis loops of Fig. 4.11 are extracted.
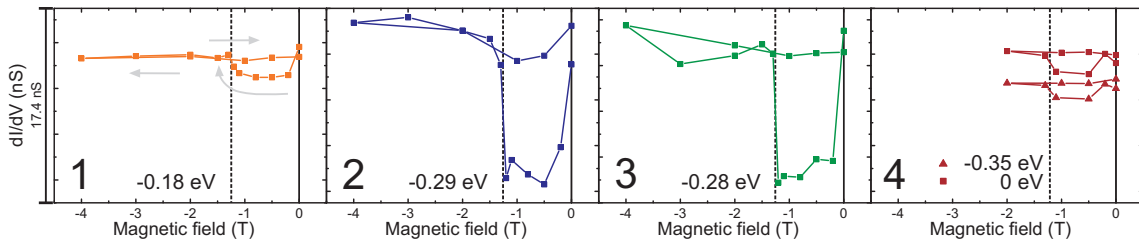

Figure 4.11: Half hysteresis loops of the dI/dV signal measured at the four positions shown in Fig. 4.10. All loops are extracted at the energies of maximum asymmetry (See markers in Fig. 4.10). For position 4 two loops are plotted, one at the maximum asymmetry and one at the peak around the Fermi energy. Dotted lines mark the switching field.

These observations reveal that the electronic structure of the island is changing significantly as a function of position. To test how this might possibly also affect the magnetic switching, spatially resolved magnetic measurements are performed. In Figure 4.11 half hysteresis loops corresponding to the spectra shown in Fig. 4.10 are presented. The loops are extracted at energies of maximum asymmetry, as defined below in Eq. (4.1). These energies are noted in the plots, and indicated by markers in Fig. 4.10. Loops 2 and 3 show a sudden change of the dI/dV signal at -1.25 T, which marks the switching of the islands magnetization direction. The signal changes at smaller fields are ascribed to a rotation of the magnetization direction of the tip. Loops 1 and 4 taken close to the rim of the island exhibit a very different shape at first sight. However, qualitatively they also show a drop of the signal at fields below -0.5 T and a jump at -1.25 T. Besides the reduced amplitude of signal change, the switching field at the rim is exactly the same as in the center. This result suggests that, on the time scale of our experiment of ≈ 100 s, the island is in a
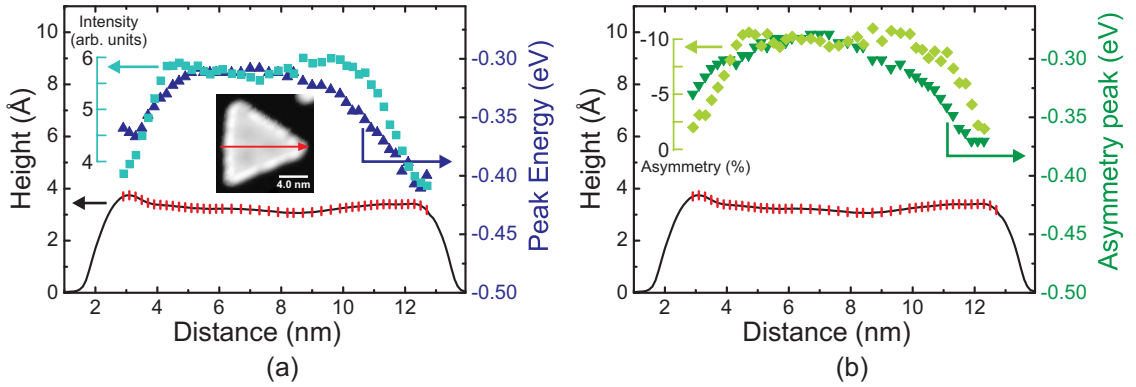
Figure 4.12: Position dependence of the electronic and magnetic properties of *one* individual Co island. Black lines in (a) and (b) show the height profile of the island along the red arrow shown in (a). All data are recorded at positions marked on the height profile. (a) Peak energy and peak intensity of the d-like surface state. Towards the rim of the island both signals shift to smaller values. (b) Energy position and amplitude of the maximum asymmetry. Both quantities decay in the proximity of the rim.

homogeneously magnetized state, as will be discussed in section 6.3.

The results described above illustrate that the energy position and intensity of the d-like peak around -0.3 V change as a function of position in a nontrivial way. Therefore a more detailed study of the phenomenon has been performed on the same island. Figure 4.12 presents a summary of this study. It displays four key parameters that are extracted from dI/dV spectra measured at different positions on the island at different magnetization states. The changes in electronic properties are characterized by position and intensity of the main peak of the spectrum near -0.3 V. The variations in the magnetic properties are characterized by position and intensity of the main peak in the asymmetry spectrum. The asymmetry between two spectra is defined by:

$$A = \frac{(dI/dV)_{AP} - (dI/dV)_P}{(dI/dV)_{AP} + (dI/dV)_P} \tag{4.1}$$

Here, $(dI/dV)_{AP}$ and $(dI/dV)_P$ are the dI/dV signal at parallel (P) and antiparallel (AP) magnetization orientation of tip and sample, respectively.

Figure 4.12(a) displays position and intensity of the main peak of the dI/dV spectrum, in (b) position and intensity of the maximum asymmetry are shown. The height profile of the island is shown as a solid black line, red markers indicate positions where spectra are measured. The inset shows a topography image of the investigated island. The evolution of peak position and intensity in (a) confirm the findings of the previous results (see Fig. 4.10). The position of the peak is shifting to lower energies towards the rim of the island and also the intensity is diminished close to the rim. Note, however, that the length scales on which these variations take place are different. This result indicates that the mechanism causing the peak shift is different from the mechanism responsible for the changes in peak intensity. A detailed discussion is given in section 6.3.1.

The peak position changes from a minimum of -0.4 eV at the islands corner to the maximum of -0.3 eV at the center of the island within 4 nm. In contrast to that, the variation of the peak intensity from its minimum value at the islands rim to the maximum
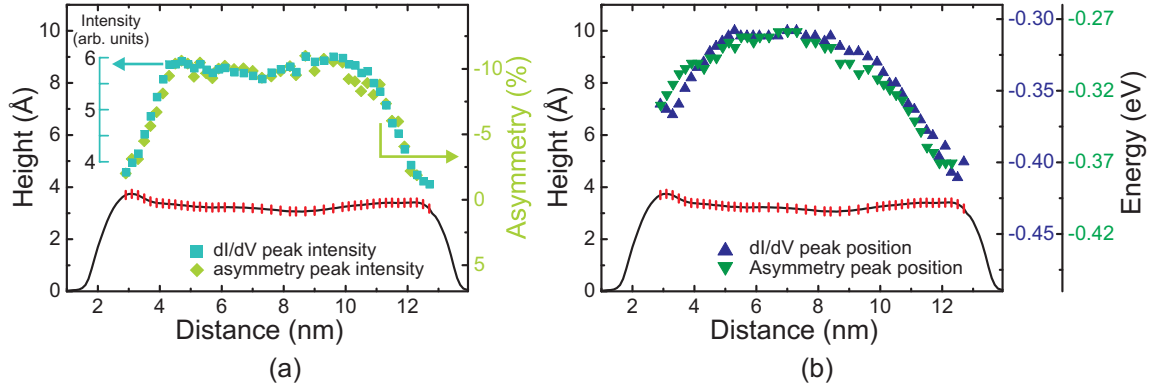
Figure 4.13: Same data as in Fig. 4.12. Here peak energies and peak intensities are plotted together. (a) The *intensity* of the surface state peak and the amplitude of the asymmetry change on the same length scale. (b) The shifting of the peak position as well as the shifting of the asymmetry peak position follow the same position dependence. The data of the asymmetry peak position are shifted vertically for clarity.

inside the island occurs on a much shorter length of only 2 nm. A similar behavior is observed for the asymmetry data. A close look at Fig. 4.12(b) reveals, that the position of the asymmetry peak changes from minimum to maximum on a length of about 4 nm, whereas the intensity changes within 2 nm from minimum to maximum. The shift of the peak position in the dI/dV spectra is ascribed to an in-plane relaxation of the Co island, as discussed in greater detail in section 6.3.1.

Since the length scales for peak shifts and intensity changes exhibit similar differences for the dI/dV as well as for asymmetry signal, it is worth to perform a different comparison. In Figure 4.13 peak positions and intensities are plotted together in one graph, respectively. Fig. 4.13(a) displays the peak intensities of the dI/dV signal and the values of the maximum asymmetry. Fig. 4.13(b) presents the peak positions of the dI/dV signal and the asymmetry spectra. In both plots a striking agreement in the position dependence of the signals is evident. This result is discussed in more depth in section 6.3.1.

4.4   Spin-polarized electron confinement within an individual Co island

The previous sections demonstrated that we are able to precisely measure the magnetic switching field of single Co islands. The corresponding results have been obtained by spectroscopy measurements performed at a fixed position (the center) on the islands. By measuring spectra at various positions within one island it was found that the switching field is constant throughout an island. However, the same measurements revealed, that the electronic structure within an island exhibits significant changes as a function of position and that even a new state appears at the rim of the islands. In addition, the results of section 4.2 revealed a pronounced modulation of the dI/dV signal within the islands, which is ascribed to electron confinement.

Here I focus on the spin dependence of electron confinement within single Co islands.
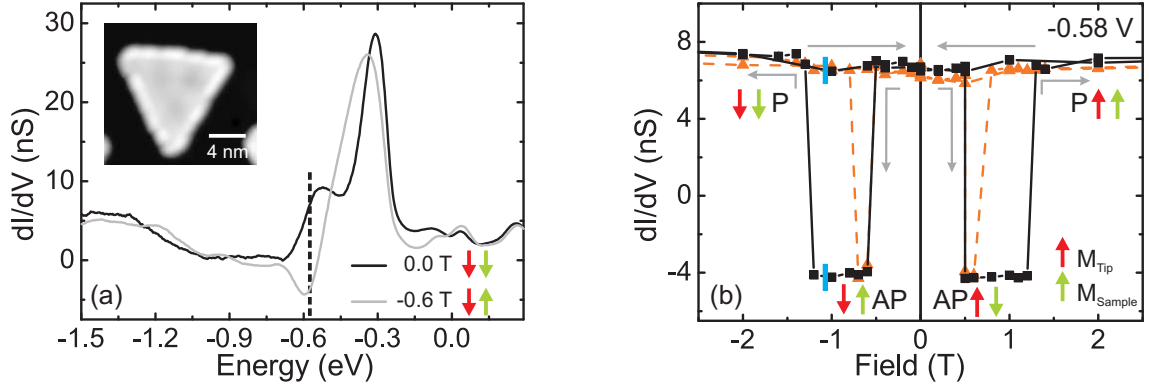
Figure 4.14: Parallel (P) and antiparallel (AP) magnetization orientations of tip and island. (a) dI/dV spectra taken on the island shown in the STM topography in the inset. (b) Hysteresis loop plotted at the energy marked in (a). Red and green arrows indicate the magnetization orientations of tip and island. Grey arrows indicate the time sequence of the field sweep. The hysteresis loop of a smaller island (orange dashed line) is shown for comparison.

An important quantity in this respect is the spin polarization. It is defined [93] by:

$$P(E) = \frac{n_\uparrow(E) - n_\downarrow(E)}{n_\uparrow(E) + n_\downarrow(E)}$$

where $n_\downarrow(E)$ is the minority spin LDOS and $n_\uparrow(E)$ is the majority spin LDOS at energy E. Wherever in this work P is mentioned, it is always defined for a fixed energy. In the following it will be shown how the observations and techniques presented previously can be used to yield a spatial map of the spin-polarization within an individual Co island. It was shown theoretically that the dI/dV asymmetry as defined in Eq. 4.1 is proportional to the spin polarizations of tip (P_T) and sample (P_S) [9, 94]:

$$A = \frac{(dI/dV)_{AP} - (dI/dV)_P}{(dI/dV)_{AP} + (dI/dV)_P} = -P_T P_S$$

Please note, that P_T and P_S are the spin-polarizations of tip and sample at the position of the tip apex and that the LDOS in vacuum strongly depends on the distance between the STM tip and the scanned surface [95].

The prerequisite for obtaining the asymmetry map of an island is a clearcut determination of parallel (P) and antiparallel (AP) magnetization configurations between tip and sample. From the data presented in Figure 4.14 a rigorous determination of P and AP orientations of the magnetization directions of tip and island is possible. The inset of Fig. 4.14(a) shows a constant current STM image of the island that is investigated. Fig. 4.14(a) also presents dI/dV spectra measured at the center of the island, which show pronounced differences in shape and peak amplitude in response to the magnetic field. These changes are resulting from the switching of the magnetization direction of either the tip or the island. At the position of maximum asymmetry (-0.58 V), marked by a dashed line, the hysteresis loop of the island is extracted (see Fig. 4.14(b)).

The hysteresis loop shows two switching events at ±0.5 T and at ±1.3 T. The first switching event is ascribed to the reorientation of the tip magnetization direction parallel
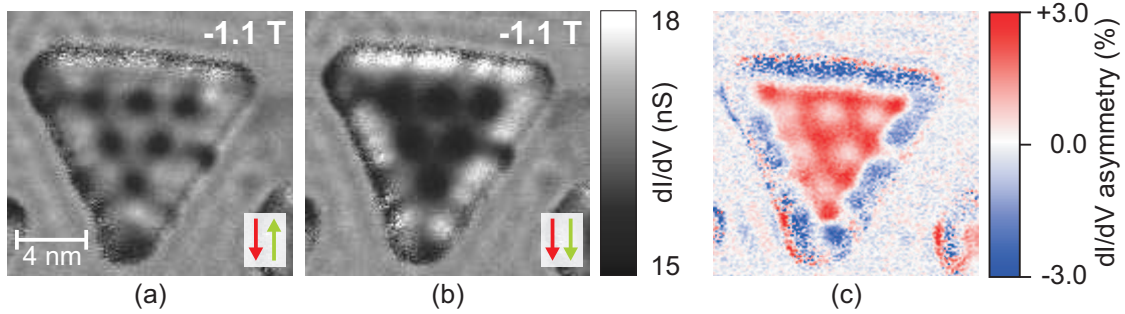
Figure 4.15: dI/dV maps of the Co island shown in Fig. 4.14 at (a) antiparallel (AP) and (b) parallel (P) magnetization orientation. Both images are recorded at -1.1 T as indicated by the blue markers on the hysteresis loop in Fig. 4.14. Within the island standing waves caused by electron confinement are clearly visible. Imaging conditions: $V_{Gap} = +0.04$ V, $V_{Stab} = +0.5$ V, $I_{Stab} = 1$ nA. (c) dI/dV asymmetry map calculated from the maps in (a) and (b). The rim of the island shows a negative asymmetry, whereas the center exhibits a positive asymmetry.

to the external magnetic field. The second change of signal results from the reorientation of the islands magnetization direction parallel to the external field. These interpretations are corroborated by an additional measurement performed with the same tip on a smaller island (dashed orange line). Here the first signal change occurs at exactly the same field as for the larger island, only the second signal change occurs at a smaller field value of 0.7 T. Hence, it is concluded that the first signal change marks the magnetization switching of the tip and the second identifies the switching of the island. This conclusion identifies the lower signal level as the AP state and the upper signal level as the P state.

With this information it is possible to measure electronic properties in the P and AP states of the system. Figure 4.15 present two dI/dV maps obtained at the same magnetic field of -1.1 T at P and AP magnetization configurations, respectively. A first inspection of the images reveals that the modulation patterns correspond qualitatively to the observations presented in section 4.2. However, there are also some pronounced differences between the two maps. The image taken in the P state shows, for example, a bright contrast on the islands rim and a dark center region. In contrast, the modulation pattern taken in the AP state does not exhibit any pronounced differences between the rim and the center region of the island.

To quantify the differences between both images, we numerically calculate the dI/dV asymmetry map shown in Figure 4.15(c) using Eq. 4.1. The resulting map, obtained close to the Fermi energy at $V = +0.04$ V, exhibits a pronounced position dependence of the dI/dV asymmetry signal within the island. The rim of the island shows a negative asymmetry (blue), whereas the inner part exhibits only positive values of asymmetry (red).

The investigations of electron confinement with a non-magnetic tip (section 4.2) showed that the dI/dV modulation patterns within the islands have a pronounced voltage dependence. It is therefore also important to study the evolution of the modulation of the dI/dV asymmetry as a function of applied voltage. Figure 4.16 presents maps of the dI/dV asymmetry obtained at different bias voltages. Each asymmetry map has been calculated from two dI/dV maps in the same way as already described for the map shown in Fig. 4.15(c). All dI/dV asymmetry maps show pronounced modulation patterns which strongly depend
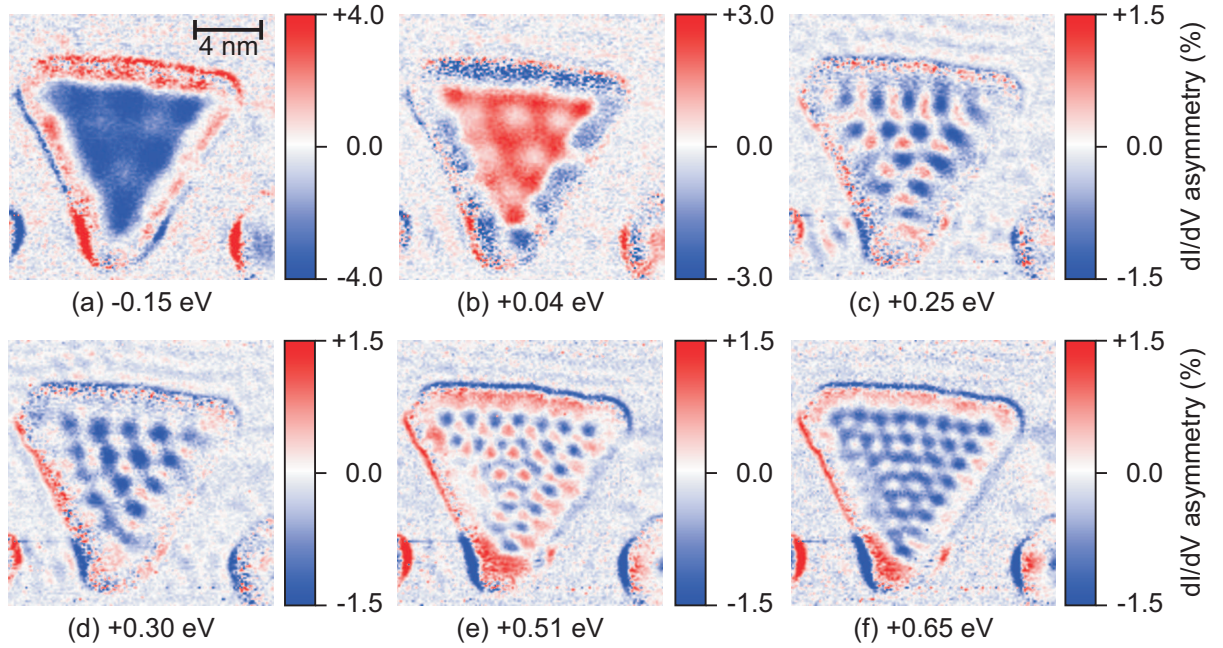
Figure 4.16: Energy dependence of dI/dV asymmetry maps of the Co island shown in Fig. 4.14. Each asymmetry map is calculated from two dI/dV maps measured at parallel and antiparallel magnetization configuration using equation 4.1. For example (b) is calculated with the maps of Fig. 4.15. The color scale is adjusted to maximum contrast for each image. Imaging conditions: $B = -1.1$ T, $V_{Stab} = +0.5$ V, $I_{Stab} = 1$ nA.

on the selected bias. The patterns get more and more complex with increasing energy and resemble very closely the behavior observed in the non-magnetic studies shown earlier in section 4.2. As stated above, the dI/dV asymmetry is proportional to the product of the spin-polarizations P_T and P_S of tip and sample. Assuming a constant spin-polarization of the tip P_T the results presented here suggest an energy dependent spatial modulation of the spin polarization within the Co island.

The experimental observations presented here are discussed in greater detail and in view of recent theoretical work in section 6.4.

Chapter 5

Co nanorods on Cu(110)-p(2×3)N

Copper nitride systems, such as Cu_2N on Cu(100) [12], have been proposed as a decoupling layer to study the electronic and magnetic properties of adsorbed atoms and clusters without or with very limited interaction with the substrate. The most desired property of the Cu(110)-p(2×3)N (Cu_3N) system studied here, is therefore to prevent an electronic or magnetic coupling of the substrate to the adatoms. To investigate this possible decoupling, a STS study of the electronic structure of the Cu_3N network and of nm long Co wires grown on top of the network was conducted, and the results are presented in this chapter.

The growth and morphology of the Cu(110)-p(2×3)N system studied here have been investigated before by Leibsle [32, 33] and York [73]. Recently Ma and coworkers at the MPI Halle [34, 35] studied the growth of various metals on the Cu_3N network. However, none of these reports investigated the electronic properties of neither the Cu_3N substrate nor the Co wires grown on top. Here, the first results on the electronic structure obtained by STS on both systems are presented.

Section 5.1 presents the results on structure and electronic properties of the clean Cu(110) surface. This section also investigates the details of the morphology and electronic structure of the Cu_3N network grown on top of the Cu(110) surface. These studies are the prerequisite for a detailed investigation of morphological and electronic properties of Co nanorods grown on top of the nitrogen network presented in section 5.2. A detailed discussion of the results is given in section 6.5.

5.1 The Cu(110)-p(2x3)N template

Figure 5.1 presents atomically resolved constant current STM images of the clean Cu(110) surface and the nitrogen network grown on top of Cu. In order to obtain optimum resolution the images have been recorded under different scan angles (ϕ) as compared to the normal scanning direction. The preparation of the Cu_3N surface has been described above in the experimental section 3.2 on page 21. Insets of Fig. 5.1 show FFT maps of the respective STM images. In (a) a constant current STM image of the Cu(110) surface is presented. The FFT map of the image yields the unit vectors $a = 0.361$ nm and $b = 0.255$ nm. These values are in perfect agreement with the corrugation extracted from the line scans presented in (c). With the lattice constant of Cu $a_{Cu} = 0.361$ nm [74] the unit vectors of the (110) surface are calculated: $a_{[001]} = a_{Cu} = 0.361$ nm, $b_{[1\bar{1}0]} = a_{Cu}\sqrt{2}/2 = 0.255$ nm. The excellent agreement with the measured values underlines the precise calibration of our STM.
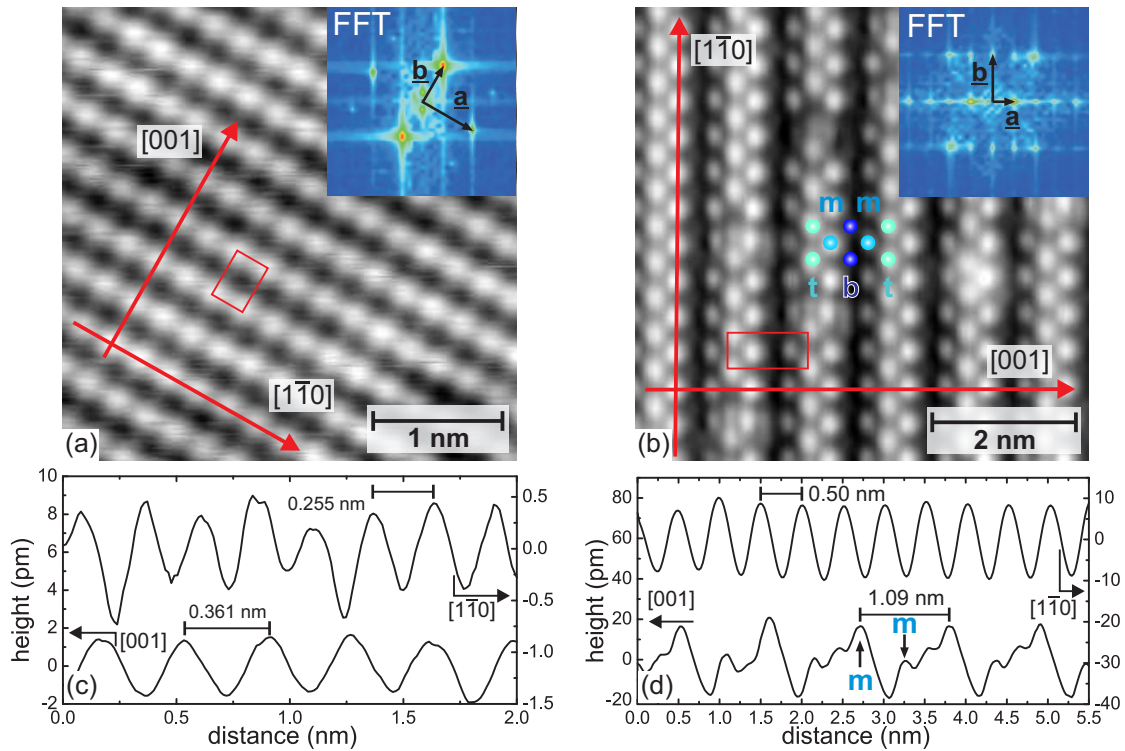
Figure 5.1: Atomically resolved STM topography images. Insets show the FFT map of the respective STM image and the lattice vectors. (a) Cu(110) substrate. Imaging conditions: $V_{Gap} = -0.02$ V, $I_T = 20$ nA, $\phi = 30°$. (b) Cu$_3$N network grown on Cu(110). Blue circles mark the positions of nitrogen atoms in top (t), middle (m) and bottom (b) positions as proposed by the model of Ma et al. [35]. Imaging conditions: $V_{Gap} = +0.2$ V, $I_T = 10$ nA, $\phi = 90°$, $T = 8.3$ K. ϕ...angle of rotation with respect to the [001] direction. (c) Line scans along the arrows in (a). (d) Line scans along the arrows in (b). Red rectangles mark the unit cells.
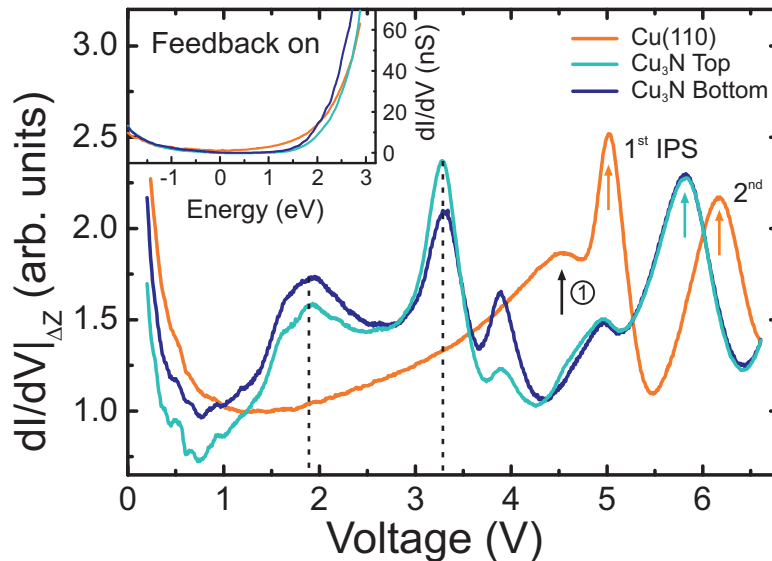
Figure 5.2: $dI/dV|_{\Delta Z}$ spectra measured on the bare Cu(110) substrate and on the Cu₃N network. The inset shows the corresponding dI/dV spectra obtained with activated feedback loop. The dI/dV spectra are, apart from the increase of the signal above 2 V, featureless. Only spectroscopy with varying tip-sample distance ΔZ shows pronounced features. Arrows mark the positions of the first image potential states (IPS). Dotted lines mark features that are solely attributed to the sample electronic structure. At position ① the signature of a projected bulk band is visible (see text for details).

This precision is the prerequisite for a structure analysis of the Cu₃N network and the Co wires grown on top of it. Fig. 5.1(b) displays the atomic structure of a network of nitrogen atoms grown on the Cu(110) surface by sputtering. See section 3.2 for experimental details. FFT and the line scans shown in (d) give the unit vectors as $\underline{a} = 1.094$ nm and $\underline{b} = 0.502$ nm. A recent publication by Ma [35] proposed a structural model for that surface, and atoms in top ("t"), middle ("m") and bottom ("b") positions are marked accordingly in Fig. 5.1(b). A discussion of our results in view of [35] is given in section 6.5.

The electronic properties of both the bare Cu(110) surface and the Cu₃N network are studied by STS. Figure 5.2 displays STS data obtained for the two systems in two different spectroscopy modes. The inset displays dI/dV spectra obtained at a constant tip-sample distance, i.e. with the feedback loop switched off. Those spectra appear featureless except for an exponential increase of the signal beyond 2 V. In order to extract spectroscopic information over a wider range of energy, a different mode of STS is applied. Spectra displayed in the main graph of Fig. 5.2 are obtained with varying tip-sample distance ΔZ, i.e. with the feedback loop switched on. The resulting $dI/dV|_{\Delta Z}$ spectra show pronounced peak-like features and no exponential dependence of the signal on bias.

The Cu(110) spectrum exhibits two peaks at 5.0 and 6.2 V, respectively. Both peaks are signatures of image potential states (IPS) as is outlined in the discussion of section 6.5. In the following peaks ascribed to the first IPS of the respective spectrum are always marked by an arrow. The spectrum of Cu(110) contains another small peak at 4.5 V. Dougherty and colleagues identified this peak as a contribution of a projected bulk band of copper [96], and we follow this assignment here. Fig. 5.2 also shows two spectra obtained on the Cu₃N
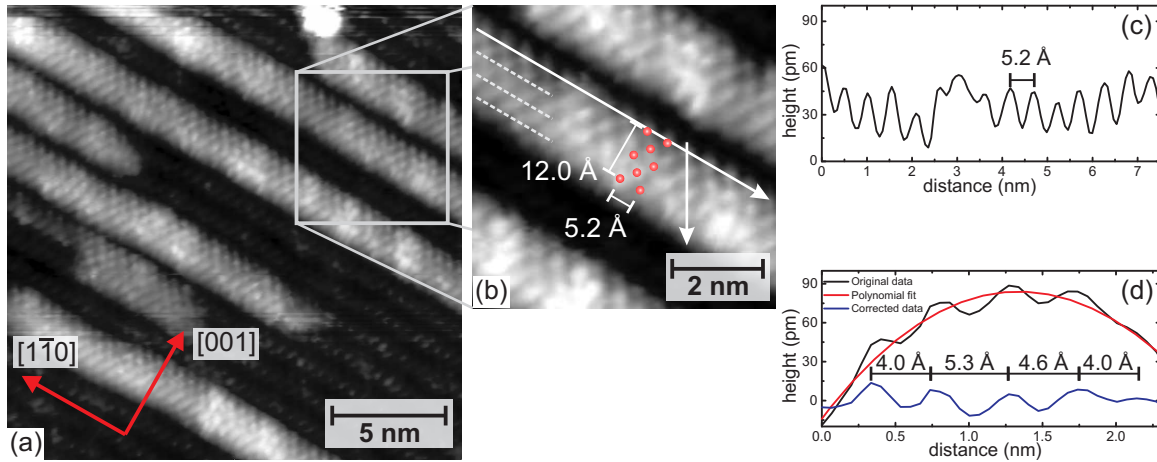
Figure 5.3: Atomically resolved STM topography of Co nanorods grown on Cu$_3$N. The bright stripes are the Co nanorods. Red dots in the zoom-in mark the Co atom positions which are similar to the model of Ma et al. [35]. Grey dotted lines are a guide to the eye and mark the Co atom rows. Imaging conditions: $V_{Gap} = -0.2$ V, $I_T = 3$ nA, $\phi = 30°$. (c) Line scan along the wire axis. (d) Line scan along the arrow across the wire. The original line scan (black) is fitted with a third order polynomial (red). The blue curve shows the line scan without the polynomial background.

network. One spectrum was measured on top of a row of nitrogen atoms (Cu$_3$N Top) and the other one at the bottom (Cu$_3$N Bottom) between two rows. Both spectra consistently reveal additional features, which are ascribed to IPSs of Cu$_3$N and other electronic Cu$_3$N signatures, as outlined in the discussion of section 6.5.

5.2 Morphology and electronic properties of Co nanorods

In the previous section the details of the morphology and the electronic structure of the Cu(110)-p(2×3)N system have been presented. This section will focus on the structural and electronic properties of Co deposited onto the Cu$_3$N substrate. Especially the influence of the substrate on the electronic properties of the nanoscopic Co structures is investigated by STS.

Atomically resolved constant current STM images of Co deposited onto the Cu$_3$N network are presented in Figure 5.3. As already described in the experimental section, Co grows in the form of elongated rod-like structures between rows of the top nitrogen atoms. The minimum separation between two Co rods is 23 Å, two adjacent rods are always separated by one Cu$_3$N "valley". The line scan presented in Fig. 5.3(c) suggests distance of 5.2 Å between adjacent Co atoms within the wire. The zoom-in reveals four rows of protrusions across the wire, marked by dashed lines, which are attributed to Co atom positions. Also the line scan in (d) shows four maxima across the wire. Thus, it seems that the wire is four atomic rows wide, in contrast to a recently proposed structural model [35], which claims a width of five atoms. This apparent conflict with the previously reported model is discussed in more detail in section 6.5.

In the following the electronic properties are investigated by spatially resolved $dI/dV|_{\Delta Z}$ spectroscopy and dI/dV maps. Figure 5.4 shows spectroscopy data obtained on the Co
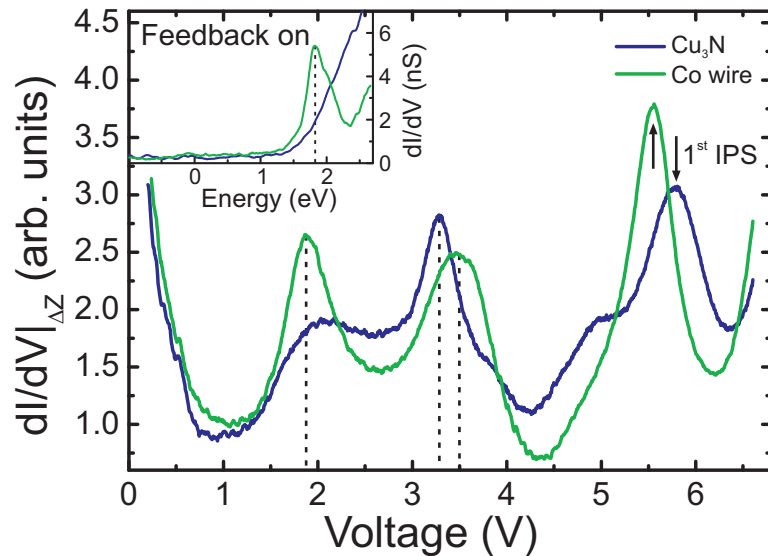
Figure 5.4: $dI/dV|_{\Delta Z}$ spectra taken on Cu$_3$N and on a Co nanorod. The inset shows the corresponding dI/dV spectra in constant Z mode. The Co nanorod exhibits a pronounced feature around +1.8 V in both spectroscopy modes (marked by dashed lines). The $dI/dV|_{\Delta Z}$ data show some additional features including the first image potential states (IPS) around 5.5 V (marked by arrows). The maxima of the peaks around 3.5 V are marked by dashed lines.

wires. The dI/dV spectrum of the Co wire shown in the inset is, in contrast to the Cu$_3$N substrate, not featureless but exhibits a pronounced peak at +1.8 V. Spectra taken in the $dI/dV|_{\Delta Z}$ mode show two peaks below the first IPS (+5.8 V) at +1.8 V and +3.5 V. The first peak is positioned at the same energy as the peak observed in the dI/dV spectrum. It is striking, that the electronic structure of the Co wire is very similar to the one of the Cu$_3$N substrate. Both systems show essentially two pronounced peaks around $+1.8-1.9$ V and $+3.3-3.5$ V. The similarity of the two spectra suggests a strong electronic coupling of the Co wires to the underlying Cu$_3$N network, as discussed in section 6.5.

To reveal more details of the electronic structure, maps of the dI/dV signal have been measured, as shown in Figure 5.5. In (a) a 40×40 nm^2 constant current STM image is presented. Figures (b)-(f) show dI/dV images of the same area measured at different voltages. A first look on the images reveals that the dI/dV signal of the Co wires is changing significantly as a function of position and energy. Also the contrast between the Co wires and the substrate is changing. At certain energies the rods appear brighter than the substrate and at other energies the opposite contrast is observed. In the discussion of section 6.5 it is proposed that these contrast variations can be understood by considering the different LDOS(E) of Co rods and Cu$_3$N substrate.

A closer inspection of Fig. 5.5(b) reveals that at +1.8 V the dI/dV signal within the Co wires shows pronounced spatial variations. These variations are irregular and do not show any periodical behavior. A possible explanation could be the presence of chemical impurities within the wires affecting the state represented by the peak at +1.8 V. Due to the missing chemical sensitivity of STM topography, such impurities could remain undetected in the topography images. Indeed Fig. 5.5(a) does not indicate any inhomogeneities within the wires. An alternative explanation would be a signature of electron confinement along
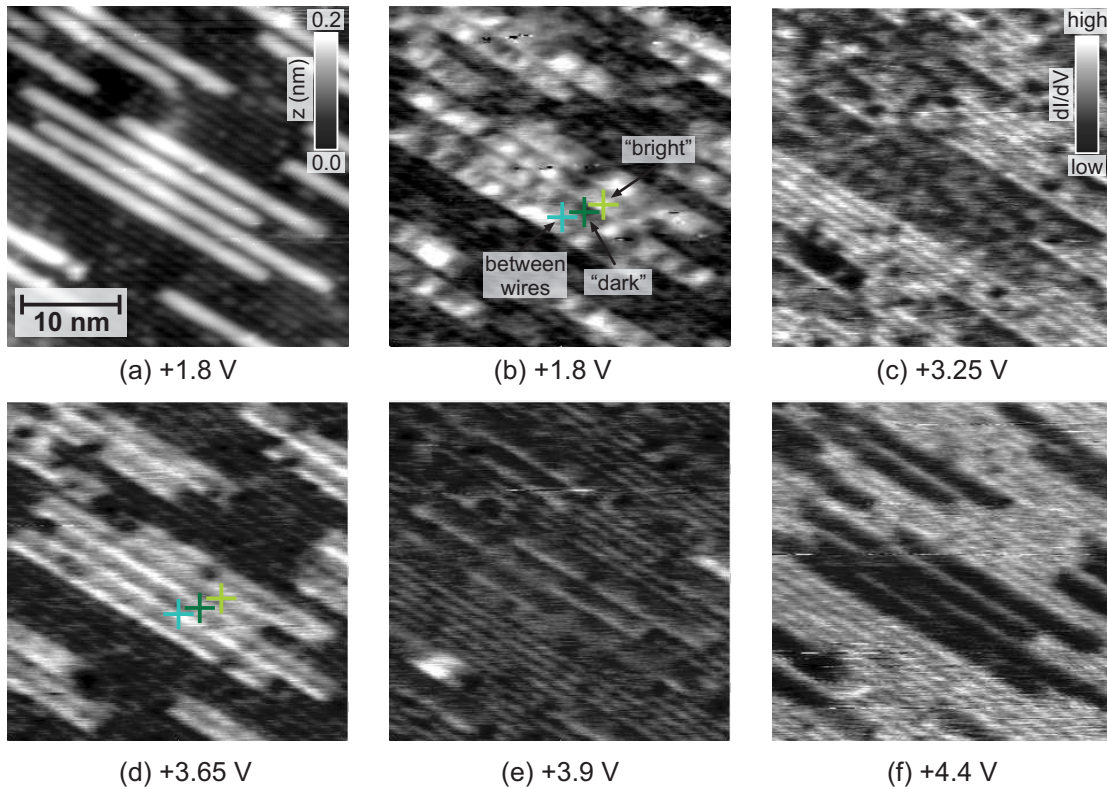
Figure 5.5: Voltage dependence of dI/dV maps of Co nanorods. All images show exactly the same area. (a) STM topography image. (b)-(f) dI/dV maps measured at the voltages denoted in the figure captions. Three crosses in (b) and (d) mark positions where single point spectra are measured (see Fig. 5.6). Imaging conditions: $I_T = 0.5$ nA, $\phi = 30°$.

the wires. Arguments supporting or disproving these ideas are given in the discussion of section 6.5.

A remarkable observation is that in Fig. 5.5(b)-(c) the dI/dV signals of the wires extents farther than the width of the wires as deduced from topography. The topography shows well separated wires with a small gap between two neighboring structures. However, in the spectroscopy images the gap is missing and wire related signals even touch. Only in (f), at +4.4 V, a gap between the wires can be recognized. A most peculiar behavior of the dI/dV signal is visible from data presented in (d). Here the dI/dV signal has a maximum at the very edge of the wires and a minimum in the center. For adjacent wires the width of the dI/dV maximum at the rim of the wires corresponds precisely to the width of the gap between them.

To yield more details on the electronic structure within the Co wires, single point spectra are measured at different positions. The positions are chosen in an attempt to clarify the cause of the dI/dV inhomogeneities within the wires. $dI/dV|_{\Delta Z}$ spectra are recorded at three positions, on a "bright" and on a "dark" spot and between the wires. They are marked by greenish crosses in Fig. 5.5(b) and (d). The results are displayed in Figure 5.6. A spectrum of the Cu_3N substrate is shown for comparison. All three Co spectra show two peaks below the first IPS, nevertheless, position and height of the peaks differ markedly. The differences between the three spectra are most distinct for the
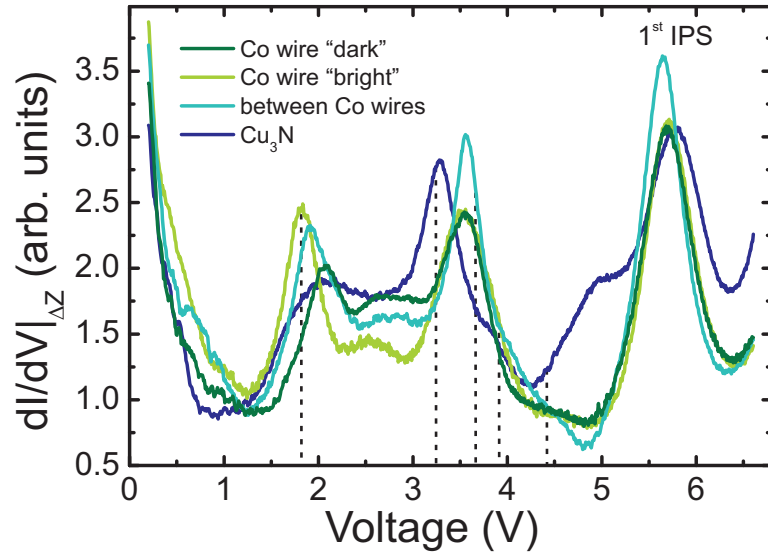
Figure 5.6: $dI/dV|_{\Delta Z}$ spectra obtained at the positions marked in Fig. 5.5. Dotted lines mark energies at which dI/dV images are recorded.

first peak. The peak position changes from +1.8 V at the bright spot to +1.9 V between the wires and reaches +2.2 V at the dark spot. The intensity of the peak decreases with increasing energy. Inspecting the second peak yields a rather different picture. Here the position of the peak is the same for all three positions. Even the intensity of the "dark" and the "bright" spectrum is the same. Only the spectrum taken at the gap position shows a distinctively increased intensity.

In conclusion the above results present the first study of the *electronic* structure of Cu(110)-p(2×3)N and of Co wires grown on top. This study extends the previous topography study by STM [35], and it reveals that the electronic structure of the wires is very similar to that of the Cu$_3$N substrate. This suggests a strong electronic coupling of the wires to the substrate, as outlined in the discussion (sec. 6.5). Hence, the Cu(110)-p(2×3)N surface does not seem to be a good candidate for studying the decoupled electronic structure of objects grown on top of it, as will be discussed in section 6.5.

Chapter 6

Discussion

In this chapter a detailed discussion and analysis of all experimental data presented above is given. The different topics are ordered according to their occurrence in the results chapters 4 and 5. First the results obtained on the electron confinement within a Cu stripe on Cu(111) and within Co islands on the same surface are discussed. It is demonstrated that the discrete dispersion relations obtained for both systems can be explained by electron wave-vector quantization, and that the quantized wave-vectors follow a very simple quantization rule. Models used previously are tested for their applicability. Section 6.2 summarizes and discusses our results on the important role of the magnetic tip used in spin-STM measurements. It is shown that measuring dI/dV hysteresis loops in an external field is a decisive prerequisite for a reliable characterization of tips used in spin-STM.

Section 6.3 discusses our results on the magnetic switching field of individual Co islands on Cu(111). It is attempted to describe the size and temperature dependence of the switching field in the framework of the thermally assisted coherent magnetization reversal model by Néel and Brown. However, this attempt leads to a clear failure of this model, and possible alternatives are discussed. In section 6.4 the experimental observation of a modulated dI/dV asymmetry within the Co islands is discussed in view of recent theoretical work. It is outlined that the observed phenomena can be explained by a spatially modulated spin-polarization within the islands. The chapter closes with a discussion of the results on the structural and electronic properties of Co wires on Cu(110)-p(2×3)N and the substrate itself.

6.1 Electron confinement and quantization rules for nano-structures

In this chapter the results obtained for the electron confinement presented for the Cu stripe on Cu(111) and for the Co islands on Cu(111) will be analyzed and discussed.

Figure 4.2 on page 29 shows a series of dI/dV maps of the Cu stripe which exhibit pronounced modulation patterns that change with energy. This observation is ascribed to the formation of standing waves in the local density of states (LDOS) due to confinement of surface state electrons of the Cu(111) surface state. Electrons in the Shockley surface state of Cu(111) form a two-dimensional, nearly free electron gas (2DEG) within the surface layer. The electrons of the 2DEG are free to propagate parallel to the surface, but their wave functions decay exponentially into the bulk and into vacuum [75]. Scattering of
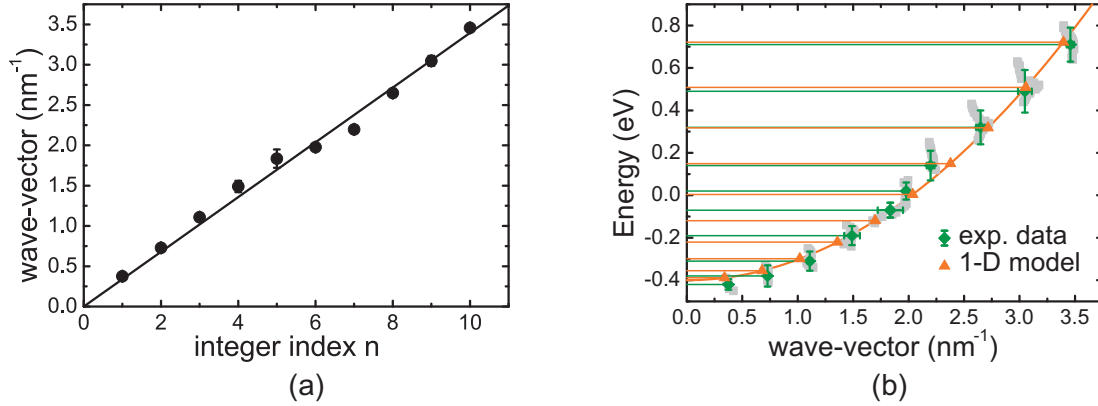
Figure 6.1: Quantization of the wave-vector within a Cu stripe on Cu(111). (a) Plot of the average wave-vectors, as extracted from Fig. 4.3(a), as a function of an integer index. Error bars are given by the standard deviation of the data, as depicted by the k error bars in (b), and they are mostly smaller than the plot symbol. (b) Quantized dispersion relation. Green data points mark the averaged wave-vectors, horizontal lines mark the energy centers of the eigenstates as extracted from Fourier analysis. Calculated eigenstates of the 1D particle-in-a-box model are marked by orange data points and lines.

the corresponding electron waves at potential barriers, such as the edges of the Cu stripe, leads to an interference of incoming and outgoing waves, and standing wave patterns form. Constant current images taken near zero bias reflect the spatial distribution of the LDOS at the Fermi Energy [40]. The image in 4.1(a) is taken very close to the Fermi energy (+0.05 V) and hence the modulated LDOS becomes visible.

In the results section 4.1 the energy dependence of the wave-vector within the stripe is extracted from the dI/dV maps by a FFT analysis. The resulting dispersion relation is presented in Fig. 4.3(a) on page 30. The data points follow a parabolic shape, although they exhibit a distinct quantization in k. As pointed out above the surface state of Cu(111) leads to the formation of a nearly free electron gas (2DEG) at the surface of the crystal. For a free electron gas a parabolic dispersion relation is expected [86]. Hence, the data are fitted by a parabola and the onset of the surface state $E_0 = -0.40 \pm 0.02$ eV and the effective electron mass $m^*/m_e = 0.39 \pm 0.01$ are extracted from the fit. These parameters are in close agreement with data obtained by high-resolution photoelectron spectroscopy (PES) [97]. This previous study reports for the Cu(111) surface $E_0 = -435 \pm 1$ meV and $m^* = 0.412\ m_e$, for the wave-vector at the Fermi energy they find $k_F = 2.15$ nm^{-1}. The analysis of the electron dispersion measured at the Cu stripe yields $k_F = 1.98 \pm 0.02$ nm^{-1}.

The comparison of our results for E_0 with photoelectron spectroscopy data [97] reveals that the bottom of the surface state band E_0 found within the Cu stripe is slightly shifted towards the Fermi energy. This effect has been discussed previously in terms of a depopulation of surface states on small terraces on Ag(111) [98]. However, the authors of [98] only observe this effect for terrace widths smaller than the Fermi wavelength of the surface state electrons. The Fermi wavelength of the surface state electrons on Cu(111) is $\lambda_F \sim 3$ nm [99] and thus three times smaller than the width of the Cu stripe. Hence, a depopulation of the Cu(111) surface state within the Cu stripe is excluded.

Previous work [85], by applying the same FFT analysis as used here, obtained the parabolic dispersion from standing wave patterns at a step edge on Cu(111) and found

$E_0 = -0.43 \pm 0.01$ eV and $m^*/m_e = 0.39 \pm 0.01$. In contrast to the Cu stripe, the dispersion relation of the step edge is not affected by confinement effects. The slight difference of $\Delta E_0 = 30$ meV, found between the stripe and the step edge, suggest, that the confinement could have an effect on the energy of the bottom of the surface state band of Cu(111). To clarify this point a systematic study of stripes with different widths is required, but such experiments have not been performed yet. In summary, despite the slight differences in E_0 between our results and previous work, it is concluded that the band structure of the Cu(111) surface is, besides the quantization, hardly affected by the confinement.

The details of the quantization of the dispersion relation will be discussed in the following. The first question to answer is: Is there a quantization rule with which the spectrum of states found in the dispersion can be explained? To answer that question we plot the sequence of wave-vectors k_n as a function of an integer number n in Fig. 6.1(a). The data can be fitted by the relation $k_n = n\pi/d$, where d is the characteristic length of the system. The fit yields $d = 9.2$ nm. This is exactly the width of the stripe, which is obtained from STM topography data. The width of the stripe is defined as the width of the topography line scan through the stripe at half height (see Fig. 4.1(b)). Fig. 6.1(b) shows, that also the dispersion is resembled by the model. Here we use $E_n = E_0 + \hbar^2 k_n^2/(2m^*)$. In conclusion the quantization rule of the electron wave vector reveals the width of the stripe as the relevant length scale for confinement effects.

That result is a direct manifestation of a textbook example of quantum mechanics. The applicability of such a simple relation for a real world nanosystem comes as a surprise. It suggests that the straight monoatomic steps of the Cu stripe of Fig. 4.1 represent an effective one-dimensional confinement. Previously, confinement in similar systems like terraces on vicinal surfaces [98, 100] have always been described by more complicated models. Here it is the first time, that the most basic model of an one-dimensional quantum box is applied successfully. A comparison to the models used in literature follows below.

As demonstrated in the results section, the FFT analysis does not only yield the magnitude of the wave-vectors but also intensity information. Rodary and coworkers at the MPI Halle have shown with the help of ab-initio calculations, that the peaks in the energy dependence of the Fourier intensity mark the positions of all eigenstates of the system [85]. The common approach to identify the eigenstates of a quantized system via STS is to take dI/dV spectra at high symmetry points of the system and to correlate maxima in the spectrum to eigenstates using specialized models [101, 102]. Rodary et al. demonstrated that this procedure is not sufficient to identify the *complete* set of eigenstates. They found that, in contrast to previous belief, minima *and* maxima of dI/dV spectra, taken at a high symmetry point of the system, identify eigenstates of the system.

We follow that idea and compare the dI/dV spectrum taken at the center of the stripe with the FFT intensity peaks in Fig. 6.2(a). We find that the positions of FFT intensity peaks are matched by the minima and maxima in the dI/dV spectrum. A close inspection of the data revealed that the dI/dV spectrum was obtained 0.3 nm away from the center. This leads to a worse agreement of the two datasets. This finding underlines the deficiency of the previously established approach [101, 103–105] of using only single point spectra to identify eigenstates.

Previously, standing wave patterns of the dI/dV signal between two parallel step edges on Ag(111) have been investigated [100]. The authors employed a Fabry-Pérot model, known from optics, to interpret their experimental results. To check the validity of this model, we apply this model to our data. Fig. 6.2(c) shows the LDOS at the center
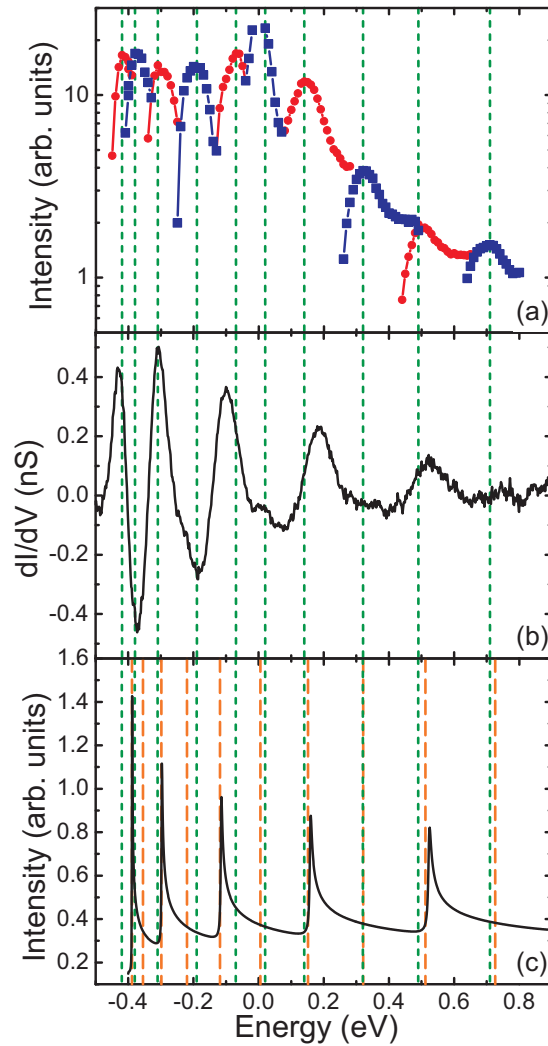
Figure 6.2: Eigenstates of the Cu stripe. (a) Intensities of the eigenstates as extracted from FT analysis. Adjacent states are colored in blue and red for clarity. (b) Single point dI/dV spectrum measured 0.3 nm away from the center of the stripe. Minima and maxima of the dI/dV signal identify eigenstates. (c) Calculated LDOS at the center of the stripe obtained with the Fabry-Pérot model of previous work [100]. This model fails to identify all eigenstates in contrast to our analysis of (a) and (b), the optical model misses the eigenstates linked to the minima of the dI/dV signal. Green dashed lines mark the peak positions of the FFT intensity, orange dashed lines mark the energies of the eigenstates as predicted by the particle-in-a-box model.

of the stripe calculated with the formula given in [100]. The input parameters for this calculation are $E_0 = -0.40$ eV and $m^* = 0.39\ m_e$, as extracted from the parabolic fit of the dispersion relation, and the width of the stripe $d = 9.25$ nm. A comparison to the FFT intensity data reveals that there is a qualitative disagreement with the experimental data. The number of peaks in the calculated LDOS (five) is less than half the number observed in the FFT intensity data (eleven). The positions of the calculated peaks match the positions of the eigenstates only at three energies (-0.3, $+0.18$, $+0.5$ eV). The orange dashed lines in Fig. 6.2(c) mark for comparison the energies of the eigenstates as predicted by the particle-in-a-box model. Good agreement is observed only for every second peak of the LDOS. Both calculations are performed with the same input parameters. Thus, the Fabry-Pérot model qualitatively only predicts half of the eigenstates, it misses eigenstates which are linked to minima of the dI/dV signal. In conclusion, the Fabry-Pérot model is not suitable to identify the eigenstates of this one-dimensional quantization problem, but the analysis presented above does so.

A point that has not been discussed yet is the energy dependence of the amplitude of the eigenstates as identified by FFT intensity. Fig. 6.2(a) reveals a monotone decrease of the amplitude starting at the Fermi energy. The peaks also become slightly broader towards higher energies, see Fig. 6.2(a). To find possible explanations for this observation we compare our results with the work of Rodary et al. from the MPI Halle [85]. In their work the authors investigated the electron confinement within hexagonal vacancy islands on Cu(111). They successfully applied the one-dimensional particle-in-a-box model to describe the wave-vector quantization observed for this system. The authors also observe a decay of the FFT intensity with increasing energy. However, they do not observe a constant FFT intensity below the Fermi energy, as it is obtained here. In contrast, they find a continuous intensity decrease over the whole energy range from -0.44 to $+0.1$ eV.

This result is rather surprising since the vacancy islands are also a pure copper system and therefore the scattering properties should be very similar to the Cu stripe studied here. One obvious difference between the two systems is however, that the vacancy islands are surrounded by Cu, whereas the stripe is surrounded by vacuum. Hence, a possible cause of the different decay of the FFT intensity is a different coupling mechanism at the edges of the confining structures. Since the Cu stripe is surrounded by vacuum, a different coupling to bulk states is expected as for the vacancy islands surrounded by Cu atoms.

Previous work on electron confinement between step edges on Ag(111) [100] extracted from fits with a Fabry-Pérot model, that the reflection amplitude of a descending step (corresponding to the Cu stripe and the Co islands) is by a factor of two larger than the reflection amplitude of an ascending step (corresponding to the Cu vacancy holes). The authors explained this difference by a stronger coupling of the wave functions of the surface state electrons to bulk states at ascending steps. Thus, the picture of different coupling strength to bulk states for the different systems investigated here, seems to be supported. However, a possible change of scattering properties taking place at the Fermi energy, which is found here for the first time, was not observed by previous work [100]. Hence, a detailed understanding of this topic requires additional theoretical input.

Confinement within Co islands

The results presented in section 4.2 revealed, similar to the observations made for the Cu stripe, pronounced modulation patterns within the Co islands. The energy dependence of these patterns is investigated and the wave-vector is extracted from the wave patterns by
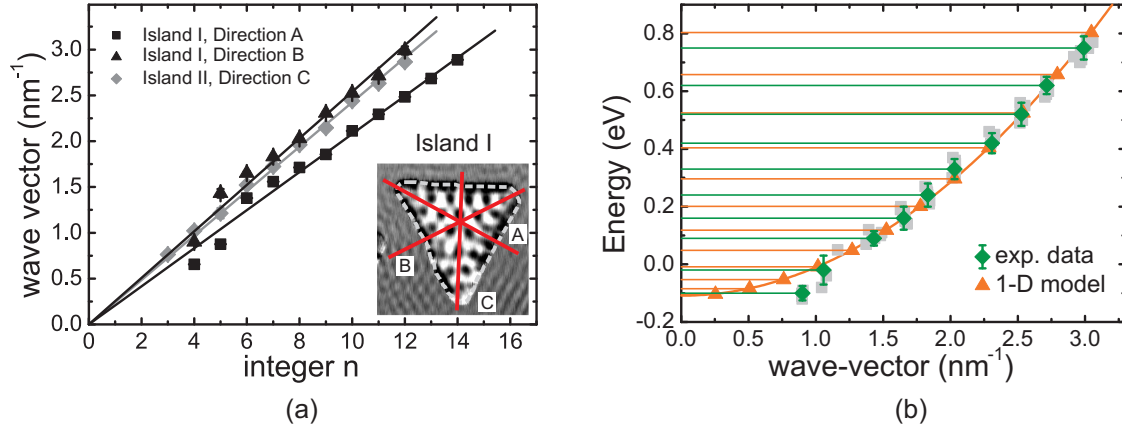
Figure 6.3: Quantization of the wave-vector within a Co island on Cu(111). (a) Plot of the average wave-vectors, as extracted from Fig. 4.5(a), as a function of an integer index. The three data sets correspond to three directions of the triangle. The data for direction C is obtained from the island shown in Fig. 6.5(c). Inset: dI/dV map with $V_{Gap} = +0.09$ V, $I_T = 1$ nA. (b) Quantized dispersion relation of direction B, island I. Green data points mark the averaged wave-vectors, horizontal drop lines mark the energy centers of the eigenstates as extracted from Fourier analysis. Eigenstates of the 1D particle-in-a-box model are marked by orange data points and drop lines.

an FFT analysis. The dispersion relation of the sp-like Co surface state [23, 106] on the Co islands is obtained (see Fig. 4.5(a) on page 32).

Similar to the Cu stripe discussed above, the obtained dispersion relation also exhibits a pronounced quantization. For the Cu stripe, the application of the 1-D quantization rule was rather intuitive. However, due to the triangular two-dimensional shape of the Co islands a more complex explanation of the quantization might be expected. Figure 6.3(a) shows a plot of the averaged wave-vectors, as extracted from FFT analysis, for the three symmetry axes observed in the FFT patterns. Two sets of data are presented for the island shown in Fig. 4.4 (Island I) and one set is shown for a second island (see Fig. 6.5(c). All three data sets reveal a linear increase of k with increasing n. Thus, the simplest model that can be applied is again $k_n = n\pi/d$. It is not so obvious, however, what the characteristic length of a triangle is. The characteristic length d extracted from the fit equals the geometric height of the triangle.

This surprising result indicates that the quantization of the wave vector k caused by electron confinement in a two-dimensional triangular quantum well can be reproduced by the one-dimensional particle-in-a-box model. An explanation for this unexpected result is suggested by referring to geometrical arguments. Figure 6.4 shows the ideal case of an equilateral triangle with base length a. Let us assume that a plane wave emerges from the lower base of the triangle. It will propagate along the height of the triangle h_1 until it hits the left side. After specular reflection the wave propagates along the height h_2 until it hits the third side. A standing wave is formed when the wave travels back and forth along the sketched trajectory. One can show that the sum of the two small heights equals the height h of the triangle[1]:

$$h_1 + h_2 = h$$

---

[1] Using the line segments defined in Fig. 6.4, and keeping in mind that the angles within an equilateral
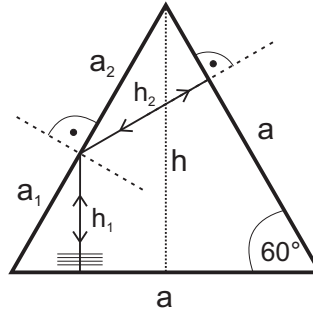
Figure 6.4: Closed trajectory of a propagating plane wave within an equilateral triangle. The heights of the two small triangles, formed by the trajectory, h_1 and h_2, sum up to the height h. See footnote 1 on page 58 for details.

Hence, it is proposed that for electron confinement in a triangle the height is the characteristic length.

A comparison of the three d extracted for the different directions in Fig. 6.3(a) with STM topography data is shown in Figure 6.5. Note, that this island is not equilateral and the three heights differ. Fig. 6.5 reveals a systematic deviation of the extracted characteristic lengths from the different heights. The extracted d are always a bit smaller than the topographical values. Two possible mechanisms are proposed, which could cause this deviation. A general explanation is that the electronic structure of the island is changed close to the rim. Such a change would alter the position of the potential barrier responsible for the scattering towards the island center and thus might lead to a reduced characteristic length.

It was shown in section 4.3.3 that the electronic structure is changing significantly as a function of position on the island. This phenomenon can be explained by an in-plane relaxation of the island [24]. Furthermore an additional state occurs at the rim of the islands around the Fermi energy. This also alters the electronic structure and hence the scattering potential barrier at the rim of the islands. The spatial distribution of that rim-state has a constant width of about 1.4 nm, as extracted from our measurements in Fig. 4.16 (see also section 6.4 for details). The deviations seen in Fig. 6.5 differ between 1.3 and 3.8 nm. Thus it seems unlikely that these deviations are only caused by the rim-state. It rather seems that the relaxation effects and the non-equilateral shape of the triangular islands, which could lead to a different scattering trajectory, are causing the observed deviations. However, the statement, that the characteristic length of quantization within the triangular islands is dominated by the height, seems to be decently well supported by this analysis.

A close inspection of Fig. 4.5(a) reveals that the $E_0 = -0.11$ eV obtained by a parabolic fit of the data lies above the energy where the first modulations are observed (-0.18 eV). Previous studies reported values of -0.22 [89] and -0.16 eV [23]. The calculations of the

---

triangle are all $60°$, we yield:

$$
\begin{aligned}
\sin(60°) &= \sqrt{3}/2 = h_1/a_1 = h_2/a_2. \\
h_1 + h_2 &= \sqrt{3}/2(a_1 + a_2) \\
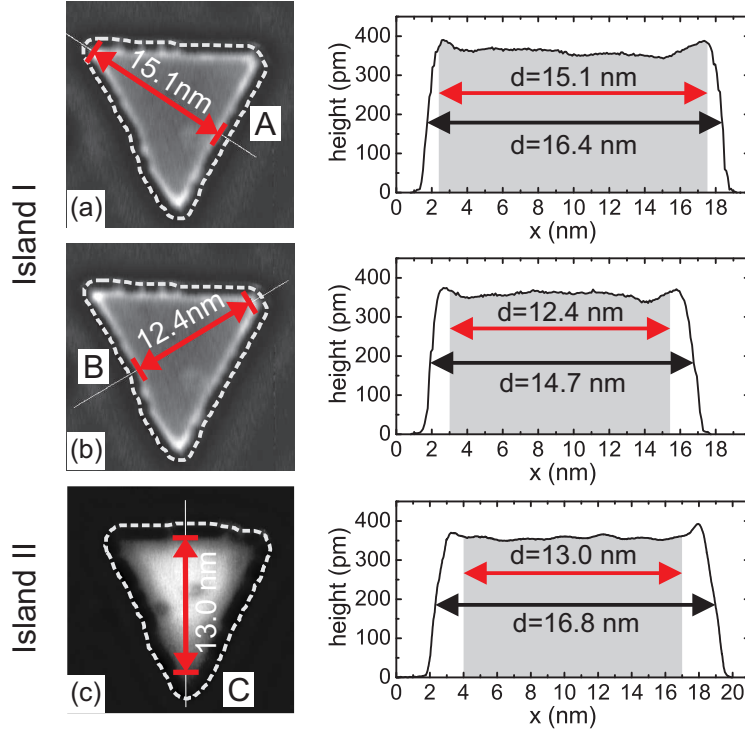&= \sqrt{3}/2\ a = h.
\end{aligned}
$$

Figure 6.5: Comparison of the characteristic lengths extracted from the quantization rule with topographic STM data. Images in the left column display dI/dV images of islands I and II ($V_{Gap} = -0.16$ V, $I_T = 1$ nA). Dashed lines represent the perimeters of the islands as extracted from topography images. The right column displays height profiles along the directions marked in the STM images. Grey areas mark the width of the quantum well according to the fitting results of Fig. 6.3(a).

latter work predicted a value of -0.17 eV. The value of -0.11 eV reported here is not in line with previous studies although the energy where the first modulation patterns are observed is in agreement with previous works.

Fig. 6.3(b) shows again the quantized dispersion relation presented in Fig. 4.5(a). The parabolic fit with $E_0 = -0.11$ eV and $m^* = 0.39\ m_e$ is plotted with the experimental data, the single data points on the parabola mark the states $E_n(k_n)$ as predicted by the one-dimensional particle-in-a-box model. The agreement of the $E_n(k_n)$ with the experimental data is not as good as in the case of the Cu stripe. Especially at energies around -0.2 to -0.1 eV not all states predicted by the model are observed in the experiment. As described above, the parabolic least square fit of the data presented in Fig. 6.3(b) does note take into account that the first modulations within the island are already observed at -0.18 eV. Thus, the agreement between the model and experimental data is worst at these low energies. However, despite its simplicity, the model still describes the experimental results at least qualitatively.

As already shown in the results section we also exploit the energy dependence of the Fourier intensity for the Co islands (see Figure 6.6(a)). The above discussion showed that the series of peaks observed in the Fourier intensity can be interpreted as the spectrum of eigenstates of the system. This data is compared with a single point spectrum taken
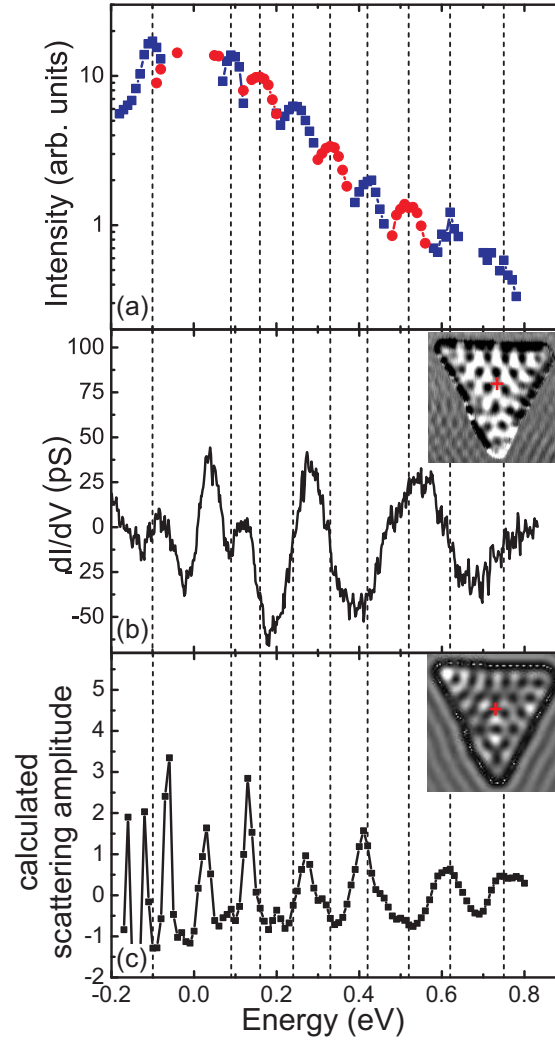
Figure 6.6: Eigenstates of a Co island on Cu(111). (a) Intensities of the eigenstates as extracted from FT analysis along direction B of island I. Adjacent states are colored in blue and red for clarity. (b) Single point dI/dV spectrum taken on the same island at the position marked with a cross in the inset. Inset: dI/dV map at $+0.09$ eV, 22×22 nm^2. (c) Calculated spectrum of scattering intensity obtained with a multiple scattering model. The spectrum is calculated at the position marked by a red cross in the inset (calculated at $+0.09$ eV). Input parameters: $E_0 = -0.18$ eV, $m^* = 0.30\ m_e$.

at the center of the island, shown in Fig. 6.6(b). The spectrum shows a series of peaks of different amplitude. The data of Fig. 6.6(a) as compared to (b) reveal, that there is no agreement of the positions of the peaks in the FT intensity. Hence, the method of identifying eigenstates by single point spectroscopy at a high symmetry point fails in this case. This statement stays valid even if one takes also the minima of the dI/dV spectrum into account. The reason for this failure is ascribed to the reduced symmetry of the non-perfect triangular shape of the island. Due to the deviations from the perfect triangular shape a high symmetry point that would presumably allow the application of the single point technique does not exist in this system. At all positions within the islands a superposition of the scattering along the three symmetry directions takes place. Therefore a single point spectrum always contains a mixture of the three dispersion relations, for three heights of the island, and no identification of eigenstates is possible.

However, the method of analyzing the full two-dimensional information by Fourier transformation applied here is capable of identifying the complete set of eigenstates. This result underlines once more the shortcomings of the previously applied single point spectroscopy to identify eigenstates.

A very simple model to explain the modulation patterns of the dI/dV signal within the islands is the so-called multiple scattering model [14, 82, 107, 108]. This model describes the observed modulation patterns as the superposition of cylindrical waves scattered at the edges of the confining structure. Figure 6.7 compares calculated modulation patterns ("calculated") with experimental dI/dV maps. The principle of calculating the modulation patterns is the following: From each position of the calculation area a cylindrical wave is emerging, and it is scattered at every scattering center within the calculation area. The superposition of all scattered waves at the position from where the original wave emerged gives an intensity value. Performing this procedure at each position (pixel) of the calculation area yields the modulation pattern. The position of the scattering centers are the positions of the edge atoms of the Co island. Here, these positions have been extracted from STM topography data. Hence, the calculations take into account the exact shape of the real Co island. In addition to the scattering centers the electronic properties of the Co island are taken into account by the model. The onset of the surface state E_0 and the effective mass m^* are used as input parameters for the calculations to derive the wavelength of the cylindrical waves as a function of energy.

As already outlined before, the simple parabolic least square fit of the dispersion relation presented in Fig. 6.3(b), which yields $E_0 = -0.11$ eV, neglects that the first modulations within the island are already observed at -0.18 eV. Taking this information into account the dispersion can be fitted with a fixed $E_0 = -0.18$ eV. The resulting parabola which yields $m^* = 0.30 \, m_e$ is presented in Fig. 6.7(g), plotted by a red solid line. This parameter set gives a much better description of the states observed at low energies and is used as the input for the multiple scattering calculations. On the other hand the states at energies above 0.5 eV deviate considerably from the red parabola. Such deviations from the free-electron-like dispersion relation were reported before [109] for Cu(111) and Ag(111). However, according to the previous results a flattening of the dispersion relation might be expected for $k_\parallel > 4$ nm^{-1}. We observe it here already around 2 nm^{-1}, although the dispersion relation of the Co surface state is not so much different from that of the Cu(111) surface state. Hence, the mechanism causing the deviations from the parabola is not understood yet.

A close look at Fig. 6.7 reveals that the model does in principle resemble the exper-
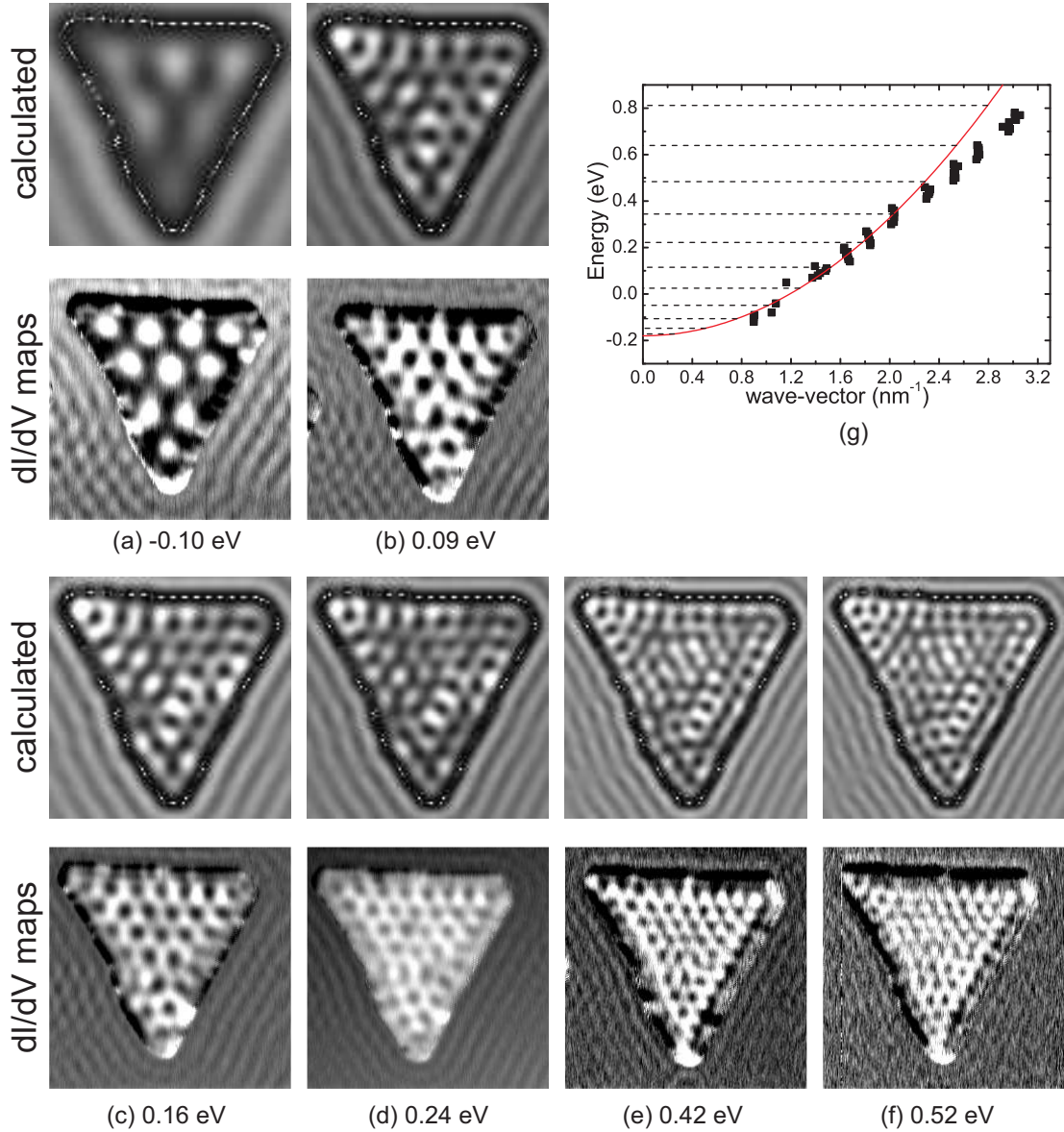
Figure 6.7: Comparison of experimental dI/dV modulation patterns with multiple scattering calculations. (a)-(f) dI/dV maps (lower images) and calculated modulation patterns (upper images). Input parameters for the multiple scattering calculations: $E_0 = -0.18$ eV, $m^* = 0.30\ m_e$. The scattering outside the island is treated with the same input parameters as the islands inner part. Since the Cu(111) surface state has a different E_0 and m^*, the wave pattern outside the island does not agree with the experimental data. Positions of scattering centers are extracted from STM topography data. (g) Dispersion relation of the Co island shown in (a)-(f). The red curve is a least-squares fit of the experimental data with a fixed $E_0 = -0.18$ eV.

imental data. In 6.7(c)-(f) a good agreement between experimental data and theory is observed. For example the number of minima at the upper edge of the island observed in experiment is also obtained by theory. However, at low energies, see 6.7(a), the model does not resemble the experimentally observed modulation pattern. This can be understood by considering that in general three different characteristic lengths, the three heights of the triangular islands, determine the scattering process within one island. Recalling that the wave-vector of the standing waves in the direction of one height is $k_n = n\pi/d$, we easily see that the influence of the characteristic length d is largest for small n. Hence, the modulation patterns at low energies (small n) are most sensitive to the asymmetric shape of the Co islands and are therefore not as well resembled by our simple calculations as the patterns at higher energies.

The calculated modulation patterns are also used to extract the energy dependence of the scattering intensity at one point within the island. Figure 6.6(c) shows a corresponding spectrum obtained at the center of the island, as marked by a red dot in the inset. The spectrum shows a series of peaks, which could tentatively be ascribed to eigenstates of the system. However, a comparison with the peaks of the FFT intensity reveals that the peak positions match only at certain energies. Hence, it is concluded that multiple scattering can in principle resemble modulation patterns observed in experiment but the energy dependence of scattering intensity at the center of the island is not suitable to identify the eigenstates of the system. The last statement supports the argument mentioned above, that not every system has a high symmetry point, which allows the identification of eigenstates with just one spectrum.

Finally I would like to mention, that in literature analytical solutions for the Schrödinger equation for a triangular quantum well have been reported [110–112]. However, all these studies treat quantum wells with infinitely high potential walls. A real world system such as Co islands on Cu(111) are very likely to have penetrable ($R < 1$) potential barriers. This is for example indicated for terraces on a Cu surface by the work of Bürgi [100]. In addition, the modulation patterns obtained with analytical solutions do not at all agree with standing wave patterns observed in experiments presented here. This is ascribed to the fact, that the shape of Co islands on Cu(111) studied here, and also in general [22], shows significant deviations from a perfect equilateral triangle.

In conclusion it is found, that

- The method of performing single point spectroscopy at high symmetry points of a confined system is not suitable to obtain the full set of eigenstates. The reason is that the peaks of the spectrum can in general only reveal half of the eigenstates, as demonstrated by the example of the Cu stripe on Cu(111). Secondly, real systems often do not have the high symmetry point that is required for this method. This is demonstrated by the triangular Co islands. Finally the method is highly position sensitive and only minute deviations from the high symmetry point lead to wrong results.

  We use the full two-dimensional information of the dI/dV modulation instead. Furthermore, this technique can be applied to a great variety of geometrical shapes.

- In the past various models have been used to explain single aspects of electron confinement.

We find that the one-dimensional quantization rule of the electron wave vector is already sufficient to explain the discrete dispersion relation and the energy levels of the eigenstates within a Cu stripe on Cu(111). The same model also leads to a decent description of the wave-vector quantization within triangular Co islands on Cu(111), although the energy levels of the eigenstates are less well described by this very simple model.

## 6.2 Characterization of magnetic tips for spin-STM

The previous section focused on electron confinement effects, and the corresponding measurements have been performed with non-magnetic tips. The next sections 6.3 and 6.4 will discuss results on the magnetic properties of Co islands on Cu(111). Thus, magnetic probe tips are required. This section points out, how such tips can be characterized by measurements in an external magnetic field.

A prerequisite for the reliable interpretation of spin-STM data is the characterization of the magnetic properties of the tip. Only a precise knowledge of the magnetic configuration of the tip opens the way to a thorough understanding of the magnetic properties of the sample. The results obtained by spin-STM always represent an entanglement of tip and sample contributions to the measured signal. Henceforth a detailed knowledge of the tip properties is necessary in order to disentangle tip and sample contributions to the measured effects.

The results presented in this work, see Fig. 4.7, demonstrate that tips having received the same macroscopic preparation can show different behavior under a magnetic field and that dI/dV hysteresis loops can be used to extract the tip contributions. These findings might give the impression that dI/dV spectra are sufficient to characterize the magnetic configuration of the tip. However, it will be shown here that this impression is deceptive. As described in sections 3.2 and 4.3.1, the preparation of tips used here is a two step process. Firstly, tips are covered macroscopically with a magnetic material such as Cr or Co and Cr. Secondly, voltage pulses are applied under tunneling conditions in order to alter the electronic and magnetic properties of the tip apex. Figure 6.8 presents dI/dV spectra measured on different Co islands with different tips. Each spectrum or pair of spectra was obtained with a tip that was microscopically and/or macroscopically differently prepared. The nominal tip coverage is given for each tip in Fig. 6.8. Common to all spectra of Fig. 6.8 is the pronounced peak around -0.3 V which stems from the d-like surface state of Co [23]. At energies below the peak several spectroscopic features are observed, which differ substantially between the different tips. These features have not been described before and they change upon application of voltage pulses. Nevertheless, high magnetic contrast is often found in this region. For each tip which showed magnetic contrast (③ − ⑦) a second spectrum is plotted (dashed lines) which corresponds to the opposite magnetic orientation, such that P and AP states are revealed.

A first conclusion can be drawn from these results: Tips with the same macroscopic preparation can show different spectral features below -0.3 V. At these negative voltages electrons tunnel from occupied states of the sample into unoccupied states of the tip. This suggests, as the LDOS of the islands is not changed during the experiment, that the electronic structure of the tip is altered by the voltage pulses. It seems that these pulses can lead to an atomic rearrangement at the tip apex which in turn is affecting the electronic structure and also the magnetic properties of the tip. To investigate the effect

Figure 6.8: dI/dV spectra measured with seven different tips at the center of different Co islands grown on Cu(111). The nominal composition of every tip is given in atomic layers. Two spectra are plotted for each tip that showed magnetic contrast. Markers indicate where the maximum contrast is obtained. Each pair of spectra and also the single spectrum ① is normalized to the maximum of the spectrum plotted as a solid line, respectively. All spectra are shifted vertically for clarity.
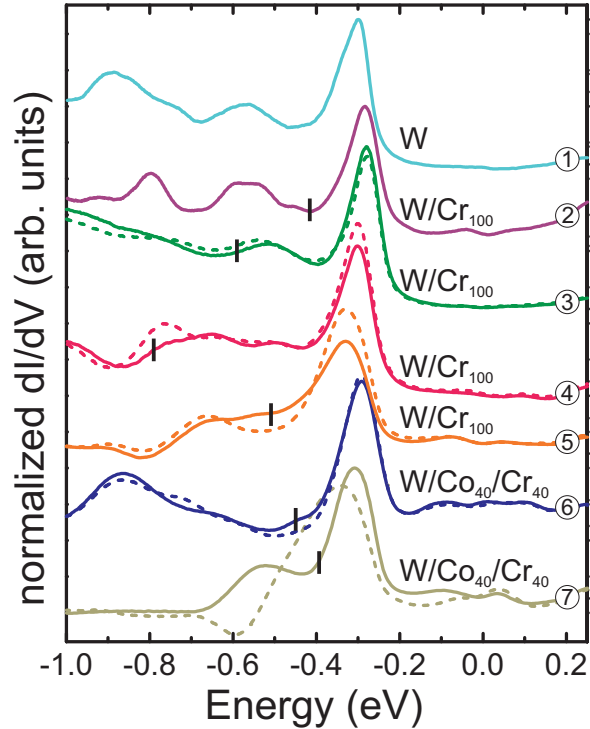
on the magnetic properties hysteresis loops are produced with the very same tips. The results are shown in Figure 6.9.

Fig. 6.9 shows hysteresis loops of the dI/dV signal at the voltages indicated by the markers in Fig. 6.8. The pure tungsten tip ① gave a constant signal as a function of magnetic field and the curve is therefore not shown. A close inspection of the loops reveals a surprising and unexpected result. Tips with the same macroscopic preparation, be it W/Cr or W/Co/Cr, do show vastly different magnetic behavior. The study of the size-dependence of the Co islands switching field has shown that the abrupt signal change around 2 T is caused by the switching of the islands magnetization direction. Thus, the changes of the dI/dV signal between the switching points of the islands are due to a reorientation of the magnetization direction of the tip. A second remarkable observation is that loop ② does not show any response to the field. Hence, the deposition of Cr onto a W tip is not sufficient to ensure magnetic sensitivity of the tip.

The loops presented in Fig. 6.9 are either asymmetric (loop ③) or symmetric with respect to the y-axis. The asymmetric form of loop ③ is ascribed to a fixed magnetization orientation of the tip apex. The symmetric form of loops ④ to ⑦ can be understood by taking into account a changing magnetization direction of the tip apex. Loops ④ to ⑥ can be explained by a continuous rotation of the magnetization direction of the tip from in-plane to an out-of-plane position. For loops ④ and ⑤ this rotation requires a larger field, however, loop ⑥ shows that the rotation can also happen in very small fields. On the other hand loop ⑦ demonstrates that the magnetization direction of the tip can also switch abruptly at ± 0.5 T.

It has been claimed in previous spin-STM work [9, 113–115] that depending on the thickness of the Cr film the tip shows either in-plane or out-of-plane sensitivity.
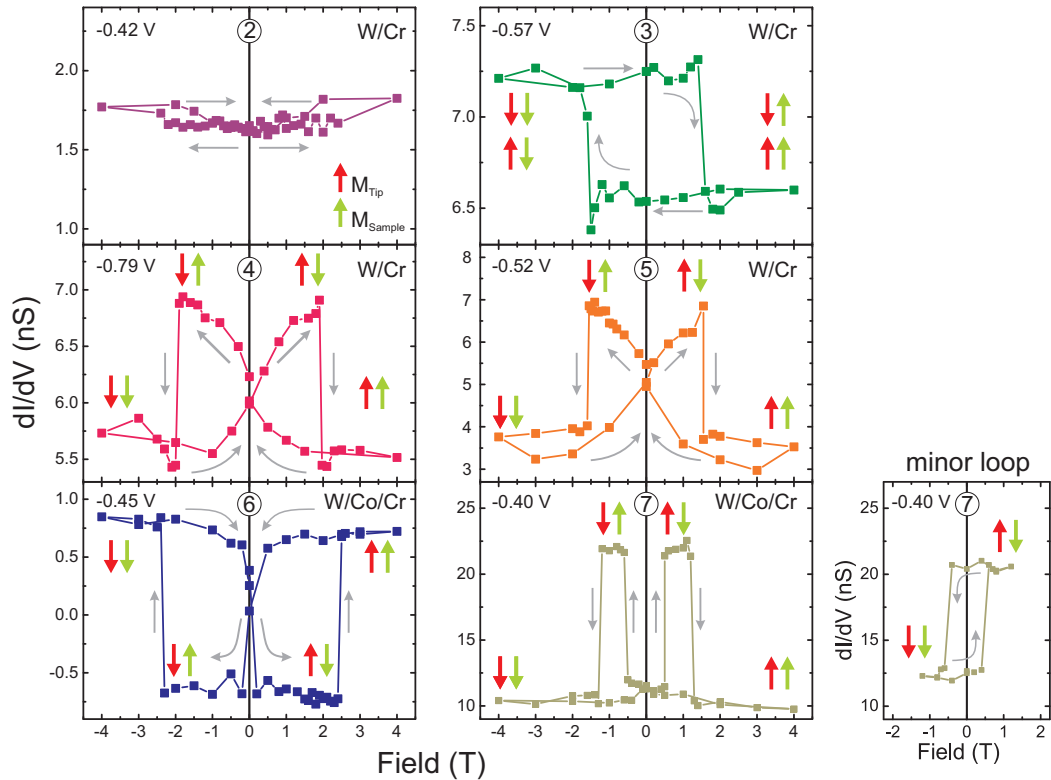
Figure 6.9: Hysteresis loops of the dI/dV signal obtained with the same tips as used in Fig. 6.8. The indicated voltages correspond to the markers in Fig. 6.8. Grey arrows indicate the sequence of data acquisition while sweeping the magnetic field. Green and red arrows sketch the orientation of island and tip magnetization, respectively. For tip ⑦ also the minor loop is shown, where only the tip magnetization direction is switched.

However, Cr is antiferromagnetic in the bulk. Therefore it can be expected that the few atomic layers of Cr deposited onto the tip also exhibit an antiferromagnetic ordering. Hence, a thickness dependence of the magnetic sensitivity of the tip is in general questionable. Our experiments do not exhibit any pronounced thickness dependence of the magnetic contrast. In contrast, the observations of Fig. 6.9 reveal a rather complex behavior of the tip magnetization direction which is even changing within the same macroscopic preparation. This underlines the decisive role of the microscopic tip preparation, which is applied in addition to the macroscopic tip coverage. Furthermore it clearly demonstrates that the magnetic configuration of the tip cannot be deduced from its macroscopic preparation.

The results presented here also have some implications for the investigation of samples with out-of-plane magnetization in zero field. Only the tips used for obtaining loops ③ and ⑦ (see minor loop) are sensitive to an out-of-plane magnetization at zero external field. The magnetization direction of tips ④ to ⑥ is concluded to be in the plane at zero field.

Another important point concerning zero field investigations is the assignment of low and high dI/dV signals to a parallel (P) or antiparallel (AP) alignment of tip and sample magnetization directions. The paired spectra in Fig. 6.8, which represent

the two different magnetization states in the respective case, show several crossings at different voltages. Each crossing of two spectra translates into an inversion of the magnetic contrast. That means at certain voltages a high dI/dV signal corresponds to the P state and a low signal to the AP state, however, at other voltages the opposite is true.

This finding is of utmost importance, as it has been tacitly assumed that a high dI/dV signal corresponds to a parallel alignment of tip and sample magnetization direction and that a low signal corresponds to an antiparallel alignment [16–18]. The above discussion shows that this assumption is not always fulfilled. Although this approach has been used in the field of spin-STM, it leads in general to questionable results. Only measurements during a completely cycle of the external field offer a reliable deduction of the magnetic configuration.

In conclusion the presented results demonstrate that neither the material deposited onto the tip, nor its thickness, nor spectroscopic features are sufficient criteria to guarantee certain magnetic properties of the tip. Hence, field-dependent measurements of the dI/dV signal are the method of choice to overcome these issues.

6.3   Magnetic properties of Co islands on Cu(111)

The results presented in section 4.3.2 showed a pronounced size and temperature dependence of the switching field H_{sw} of single Co islands on Cu(111) (see Fig. 4.9 on page 36). These observations are discussed in this section in view of a possible thermally assisted magnetization reversal process.

The size dependence of the switching field is divided into three regimes. The smallest islands show zero switching field, medium sized islands exhibit a monotone increase of the switching field with size and for the largest islands a decrease of the switching field with size is observed.

This behavior qualitatively resembles early works on thermally assisted switching of ensembles of small magnetic particles. Kneller and Luborsky [26] investigated the size dependence of the switching field of iron and iron-cobalt particles diluted in mercury. Note, however, that they investigated a huge ensemble of particles, which exhibits a broad distribution of particle size and shape, and most likely also a distribution of the easy magnetization direction. Our approach focuses on single particles with well characterized size and shape.

The simplest model for describing the switching of a small magnetic particle is the model by Néel [38] and Brown [39]. Within this theory the magnetization reversal is described as a thermally assisted coherent rotation of all spins. During the whole reversal process all spins are assumed to act in unison and are thus treated as a so-called macrospin.

In the frame work of the Néel-Brown model the energy of a ferromagnetic particle with uniaxial anisotropy in an external magnetic field is given by:

$$E = KV \sin^2 \theta - BM_s V \cos \theta \qquad (6.1)$$

With K...anisotropy constant, V...Volume of the particle, B...external magnetic field, M_s...saturation magnetization and θ...the angle between the magnetization (or
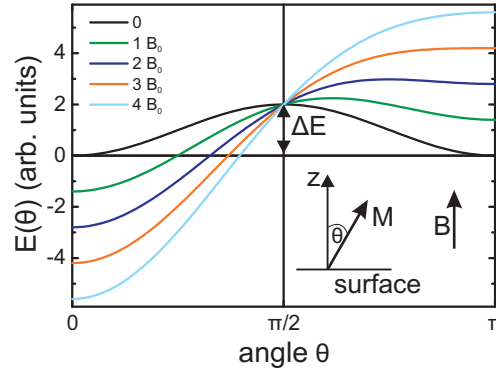
Figure 6.10: Field dependence of the energy barrier for switching the magnetization direction of a single-domain particle in the Néel-Brown model of thermally assisted coherent magnetization reversal (cf. eq. (6.1)). The one-dimensional energy landscape is plotted for different external magnetic fields B in units of B_0. For $B = 0$ the energy is degenerate for $\theta = 0$ and $\theta = \pi$. With increasing field the energy minimum at $\theta = \pi$ vanishes and the magnetization M aligns parallel to the external field B along the z direction.

macrospin) and the easy axis of the particle. Here the easy axis of the Co islands is parallel to the surface normal, as depicted in Fig. 6.10. The energy landscape $E(\theta)$ is changing as a function of the external magnetic field as illustrated in Fig. 6.10. With increasing field the energy minimum at $\theta = \pi$ is more and more shifting upward in energy, until it finally vanishes. In the sketch shown here, this situation is reached at $B = 4B_0$. At this field value only one energy minimum at $\theta = 0$ exists, and the magnetization of the particle will spontaneously align along the z axis. The energy barrier that has to be overcome to switch the magnetization orientation of the particle is:

$$\Delta E = KV \left(1 - \frac{BM_s}{2K} \right) \tag{6.2}$$

This switching barrier is competing with the thermal energy of the system. Bean and Livingston [116] defined a stability criterion for a particle whose magnetization is stable for 100 s:

$$\Delta E = 25 k_B T \tag{6.3}$$

With k_B...Boltzmann constant and T...temperature. In zero magnetic field and with constant temperature this stability criterion determines the transition point between the superparamagnetic and stable magnetization state, the so-called blocked magnetization state. Particles with $V < \frac{25 k_B T}{K}$ show a superparamagnetic response, and particles with $V > \frac{25 k_B T}{K}$ show a stable magnetization for at least 100 seconds. The critical volume where the transition from the superparamagnetic to the blocked state occurs is called blocking volume V_B.

Kneller and Luborsky interpret the transition from regime I to regime II as a transition from the superparamagnetic to the blocked state. They apply the model of thermally assisted switching to quantitatively analyze their data. They ascribe regime III, where a decrease of the switching field is observed, to the formation and propagation of domain walls due to the increased particle size. This mechanism

leads to a reduction of the switching field with increasing particle size. As tempting this interpretation might appear, the following analysis provides evidence for the assumption that already in regime II we observe a magnetization reversal by another mechanism, including non-coherent reversal and possibly domain formation.

Our questioning of the validity of the model of coherent rotation of a macrospin in region II also disagrees with the view presented in recent work. Rusponi et al. [29] and Rohart et al. [117] used the coherent rotation model to interpret their results for supported nanostructures and Wernsdorfer et al. [28] for their observations made for encapsulated clusters. We also observe a transition from a superparamagnetic to the blocked state. However, it will be shown in the following that the model of coherent rotation of a macrospin dramatically fails when it comes to a quantitative description of our data.

We observe a transition from the superparamagnetic to the blocked state as a function of the particle size. We find $V_B = 11.2 \text{ nm}^3$, which equals $N_B = 1100$ atoms, at $T = 8.3 \text{ K}$. As explained above this transition point is governed by the competition between thermal energy $k_B T$ and anisotropy energy KV. The volume V of the islands is extracted from STM topography. The observation of superparamagnetism depends on the time scale of the measurement. The time scale of the experiments presented here is of the order of 100 s. Thus, the stability criterion $k_B T / KV = 25$ applies.

Hence, using the possibly questionable model of thermally assisted switching, the anisotropy follows from

$$K = \frac{25 k_B T}{V_B}.$$

With $T = 8.3 \text{ K}$ the anisotropy is estimated to $K = 256 \text{ kJ/m}^3$. This value is surprisingly small compared to the bulk anisotropy of Co of $K_{bulk} = 513 \text{ kJ/m}^3$ [118, Table 1], especially in view of the large values reported for nanoscopic systems [29,117]. This disagreement is already a first indication that the model of thermally assisted switching by coherent magnetization reversal might not be applicable.

The failure of the model also becomes apparent when considering the maximum switching field of 2.4 T that is observed in regime II. It is well established that the Stoner-Wohlfahrth model [36, 37] yields the largest possible fields for reversing the magnetization direction of a single-domain particle. It assumes a coherent rotation of all magnetic moments in unison within a single-domain particle of ellipsoidal shape. It yields for the maximum switching field: $H_{max} = \frac{2K}{M_S}$. Several mechanisms can lead to a reduction of the switching field predicted by this model, such as shape anisotropy, none zero temperature or non-colinear transition states [119]. However, not a single mechanism is known that would lead to higher field values. Hence, the Stoner-Wohlfahrth approach gives an upper limit of the possible switching fields. X-ray magnetic circular dichroism (XMCD) measurements give an estimate for the magnetization of Co islands on Cu(111) of 1.6 μ_B/atom [120]. With the anisotropy of $K = 256 \text{ kJ/m}^3$ this yields a maximum switching field of $H_{sw} = 0.4 \text{ T}$. This value differs drastically from the 2.4 T observed in the experiment.

To underline the conflict risen by these first estimates of anisotropy and switching field, a quantitative analysis of the data with the model of thermally assisted coherent rotation will be given now. Using the stability criterion (6.3) with (6.2)
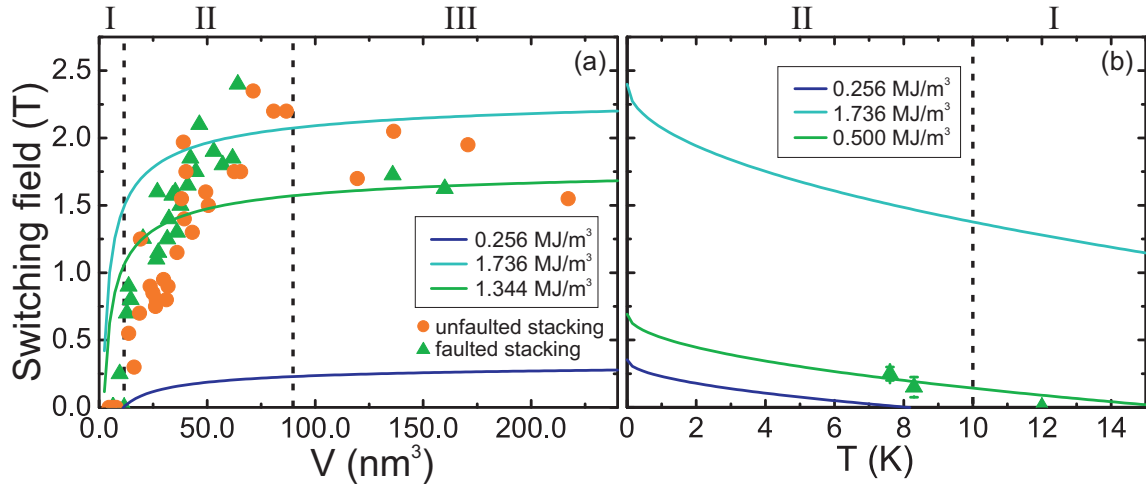
Figure 6.11: Analysis of the size and temperature dependence of the switching field of single Co islands on Cu(111). Three regimes are indicated similar to Fig. 4.9. Solid curves are calculated with the model of thermally assisted switching. Different anisotropy energies K are used in the calculations. None of the curves gives a good description of the experimental data. (a) Size dependence. (b) Temperature dependence.
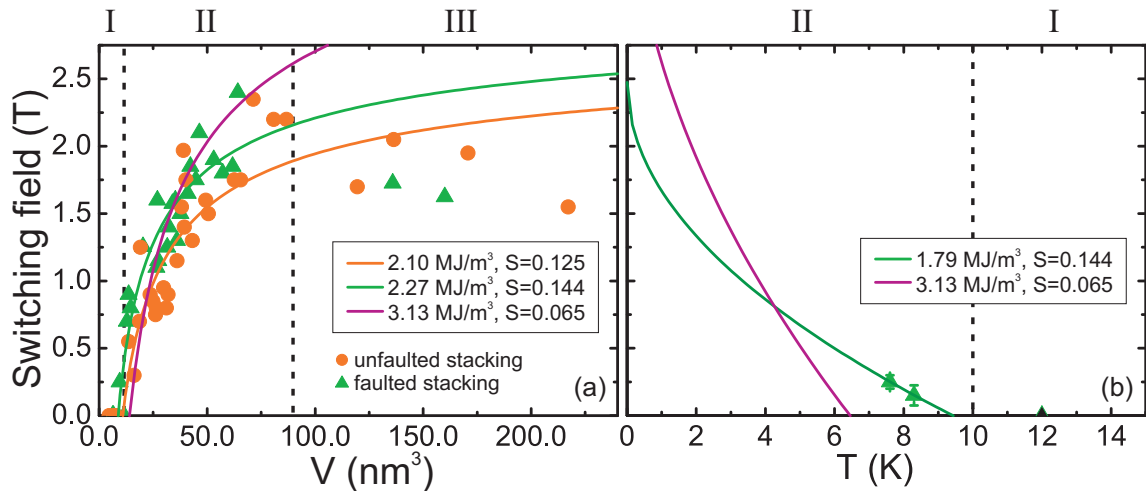
Figure 6.12: Analysis similar to that shown in Fig. 6.11. Here an additional parameter is included in the model. Green and orange curves in (a) and (b) are least square fits to the data. The scaling parameter S and the anisotropy are given for each curve. Including S in the model yields much better agreement with the experimental data. (a) Size dependence. (b) Temperature dependence.

yields the size and temperature dependence of the switching field of a single particle:

$$H_{sw} = \frac{2K}{M_S}\left(1 - 5\sqrt{\frac{k_B T}{KV}}\right) \tag{6.4}$$

This *Sharrock equation* [121] is now used to compare the model to our experimental results on size and temperature dependence of H_{sw}. The only free parameter is the anisotropy K. The calculated size dependence is presented together with the experimental data in Fig. 6.11(a). Note, that, for a better comparability to Eq. (6.4), the switching field is now plotted as a function of the island volume V and not as a function of the number of atoms within the island N. The dark blue curve is calculated with the K extracted from the stability criterion (6.3) in combination with the blocking volume V_B of 0.256 MJ/m³. The light blue curve corresponds to the anisotropy extracted from the maximum switching field of 2.4 T and the Stoner-Wohlfahrth limit: $K = \frac{H_{max}M_S}{2} = 1.736$ MJ/m³. Both curves clearly fail to describe the experimental results. The green curve is a least square fit of the data for faulted islands using the Sharrock equation. It gives an intermediate value for the anisotropy of 1.344 MJ/m³, but the quality of the fit is very poor, and we conclude that it fails to describe the experimental situation.

The Sharrock equation can also be used to model the temperature dependence of the switching field of one particle with a fixed size. Fig. 6.11(b) depicts the temperature dependence of the switching field of one single island with 1010 atoms and faulted stacking (see also Fig. 4.8). The blue curves in this plot are produced by using the same anisotropies as in the case of the size dependence above. Again, the two curves clearly fail to describe the experimental data. On the other hand choosing an intermediate anisotropy of 0.5 MJ/m³ seems to fit the data points quite well (green curve). However, in the limit of zero T the curve yields a maximum switching of only 0.75 T, which is again in sharp contrast to the maximum switching field of 2.4 T observed experimentally. This demonstrates the importance of investigating the size *and* the temperature dependence of the switching field, as performed in this work. Results obtained by one method yield an independent cross check for results obtained by the other, as demonstrated here. In summary it seems impossible to describe the experimental size and temperature dependence of the switching field with the model of thermally assisted coherent rotation.

An idea that could change the situation, at least from a formal point of view, is to introduce a second fitting parameter to the model. Going back to the Sharrock equation (6.4), three quantities could in principle be used as an additional free parameter: magnetization M_S, temperature T and volume V. The magnetization M_S only influences the maximum switching field and has in the first term of Eq. (6.4) the same weight as the anisotropy, it is therefore excluded. The temperature is well determined and was constant for all measurements of H_{sw}, there are no reasonable physical arguments to use T as an additional fitting parameter. The volume of the islands is also well determined by STM topography images. On the other hand, previous work [29] indicated that for Co islands on Pt(111), the anisotropy might be governed by the atoms located at the rim of the islands. Therefore it could be justified to introduce a second fitting parameter, which alters the volume, taking possibly
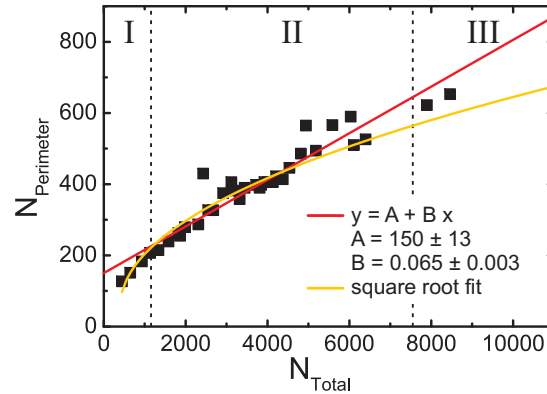
Figure 6.13: Relation between the total number of atoms of the Co islands N_{Total} and number of the atoms located at the rim of the islands $N_{\text{Perimeter}}$. The data is fitted with a square root dependence (yellow) and a linear equation (red). The parameters obtained for the linear fit are given. The three regimes as found for the size dependence of the switching field (see Figs. 4.9 and 6.11) are denoted by dashed lines and roman numbers.

only rim atoms into account. Note however, that this is merely a formal solution to the problem. Mathematically every fitting function yields a better agreement with experimental data when introducing an additional free parameter.

Here, this parameter is a scaling factor S, which is multiplied with the volume. S is simply a number and has no physical unit. For $S < 1$ the volume taken into account by the model would be smaller than the experimentally observed island volume. A fit with $S > 1$ would take into account a larger volume. Least square fits of the size dependence data including this scaling factor are shown in Fig. 6.12(a). The maybe surprising result is that decent fits of the data for faulted and unfaulted islands are indeed obtained. For faulted islands the fit yields a large anisotropy of $K_{\text{faulted}} = 2.27 \text{ MJ/m}^3$ and a small particle volume expressed by $S_{\text{faulted}} = 0.144$. For islands with unfaulted stacking the fit yields $K_{\text{unfaulted}} = 2.10 \text{ MJ/m}^3$ and $S_{\text{unfaulted}} = 0.125$. Taking these results seriously would lead to the conclusion that not all atoms of the island dictate the switching field, but only a portion of $12.5 - 14.4$ %.

As mentioned above, a previous study indicated that the anisotropy of a particle can be governed by only the atoms at the rim [29]. From STM topography we estimate the number of atoms which form the perimeter of the island ($N_{\text{Perimeter}}$). A plot of the number of perimeter atoms as a function of the total number of atoms is presented in Figure 6.13. From basic geometrical considerations a square root dependence of $N_{\text{Perimeter}}$ on N_{Total} is expected. The yellow curve is a least square fit of the data taking into account this square root dependence. The fit agrees comparably well with the data. On the other hand a linear fit (red curve) leads to a just as well agreement with the data[2]. The linear slope of the fit of 0.065 gives the rough estimate that 6.5 % of the island atoms are located at the rim. Please note, that the linear fit gives $N_{\text{Perimeter}} \neq 0$ for $N_{\text{Total}} = 0$. Thus, the number of rim atoms amounts to 6.5 % plus a constant number of 150 atoms. Fitting the size dependence

---

[2]The correlation coefficient R, which describes the quality of least squares fitting, is close to one for both fits, i.e. the correlation of both fits with the data is very high.

data with a fixed $S_{\text{rim}} = 0.065$ (purple curve) yields $K_{\text{rim}} = 2.70$ MJ/m^3. However, this fit only describes a part of the data points and fails completely to reproduce the temperature dependence of the switching field (see Fig. 6.12(b)).

On the other hand the scaling factors, which are found by fitting the size-dependence, $S_{\text{faulted}} = 0.144$ and $S_{\text{unfaulted}} = 0.125$, correspond roughly to twice the number of the rim atoms. Hence, it seems tempting to conclude that the anisotropy is carried by a double row of atoms at the rim of the Co islands. However, as I mentioned right from the beginning, these considerations only represent a very formal solution of the problem. Whether the introduction of the parameter S is *physically* well justified remains to be proven. A clear deficiency of this approach is that the adjusted model does not fulfill the main features of the original Stoner-Wohlfarth model anymore.

In conclusion, the observed size and temperature dependence of the switching field can only be resembled by the model of coherent magnetization reversal when taking into account a large anisotropy of the order of 2 MJ/m^3 in combination with an artificially introduced reduction of the island volume to about 13 % of the real volume. The large K is needed to reproduce the large switching fields and is therefore physically well justified. However, the artificial reduction of the volume presents a rather formal solution and its physically meaning is questionable. It most probably disguises the physics behind the experimental observations made here.

Recent ab-initio calculations performed by C. Etz at the MPI Halle [122] indicate that the anisotropy is not uniform throughout the island. Findings by Etz rather suggest that the magnetocrystalline anisotropy and the local magnetic moments exhibit a pronounced spatial distribution within the island. Early model calculations performed with the tight-binding method [123] also showed the trend that the magnetic moments are increased at the rim of the islands. One of the assumptions of the model of coherent rotation is a uniform anisotropy within the particle. A local variation of the anisotropy would lead to different energy barriers for switching the local magnetic moments within the islands. Thus, a coherent rotation of all spins in unison as a macrospin would become less favorable, and the magnetization reversal could not be described within the framework of thermally assisted coherent rotation. In contrast, local minima of the anisotropy could favor nucleation of so-called droplets. Droplets are, like domains, areas which are oppositely magnetized with respect to the rest of the particle. Unlike domains, droplets are non-equilibrium entities which either grow or shrink but never reach a stable size. The model of magnetization reversal via droplet nucleation is described in various publications [124–127].

One interesting aspect of these works is that systems with high anisotropy favor magnetization reversal via droplet nucleation [126]. The reason is that a high anisotropy leads to very thin domain walls between the droplets of down to one lattice constant [126]. The model of droplet nucleation is describing the magnetization reversal process of single domain particles. Hence, the "domain" walls between the droplets are considerably thinner than a "classical" domain wall between two equilibrium domains. The analysis within the model of thermally assisted switching yields, as mentioned above, a lower limit of the anisotropy for the Co islands. The

domain wall width can be estimated with $\delta_0 = \sqrt{\frac{A}{K_1}}$, where A is the exchange stiffness [128]. The high values of $K > 2$ MJ/m^3 found here would lead, in combination with a typically value for $A = 10^{-11}$ J/m, to $\delta_0 < 2$ nm. This value is smaller than the base lengths of the islands in region II of Fig. 4.9 of $9 - 20$ nm and hence such a domain wall could exist within these islands, although we never imaged two domains within one island by spin-STM.

Very recently the magnetization reversal of a very different system, namely individual Fe islands on W(110), has been investigated by spin-STM [129]. This study did not extract the magnitude of the switching field of thermally stable islands, but rather focused on the statistical analysis of the switching probability of superparamagnetic islands, as extracted from telegraphic noise in the dI/dV signal. The island sizes investigated in [129] are of the order of $30 - 150$ atoms, which translates into diameters of $2 - 6$ nm. The authors find, that their results are best described by a magnetization reversal process via nucleation. The very large anisotropy of 0.55 meV/atom (~ 7 MJ/m^3) that the authors of [129] estimate for Fe islands on W(110), supports the picture, that nanoscale structures can exhibit surprisingly high values of K. The analysis of Ref. [129] suggests that the prefactor ν of the exponential expression giving the energy barrier against reversal depends on the islands size in an anisotropic way. Thus, the authors also tackle the problem by just introducing an additional parameter, the dependence of ν on size, to their model. Since this previous report is solely focusing on the size dependent *switching probability* of particles in the superparamagnetic state, it cannot provide any insight into the size and temperature dependence of the *switching field* of islands with a stable magnetization investigated in this thesis.

In summary the analysis presented here strongly suggests that the model of thermally assisted switching via coherent rotation cannot be applied in the case of Co islands on Cu(111). It is concluded that the magnetization reversal of the islands does not happen via coherent rotation but through a process that includes non-coherent changes of magnetization. Further insight into the question why the model of coherent rotation fails is provided by the results on the position dependence of the electronic and magnetic properties within the Co islands presented in the next section.

6.3.1 Position dependence

The results presented in section 4.3.3 demonstrated that the energy position of the d-like Co peak at -0.3 V as well as its intensity change notably as a function of position on the island. Both effects are discussed in the following.

Rastei et al. observed a shift of the peak position as a function of island size [24]. The authors explain the shift of the peak towards lower energy with decreasing island size with the help of ab-initio calculations. These calculations reveal a change of the in-plane bond length of the top Co layer of the island as a function of position. The simulations show a decrease of the bond length towards the rim of the island of about 1 %. This value is explained by the macroscopic lattice mismatch between the Cu substrate and Co of 2 %. The authors use these results to interpret island *size* dependent peak shifts in their spectra. However, experiments presented here

go beyond this approach by studying the peak shift, the intensity variations and the evolution of the asymmetry on *one individual* island.

Figure 6.14 compares the results obtained for the peak shift and intensity variation within several individual Co islands with the calculated in-plane Co bond length reported previously [24]. The data presented in Figure 6.14(a), reveals that the peak shift is occurring on a length scale of 2 nm (3 nm) going from the edge to the corner (or vice versa). Figure 6.14(c) and (d) present data on the position dependent peak shift obtained on four other islands. In (c) the spatial variation of the peak energy of each island is plotted as a function of the distance from the corner of the islands. In (d) the same data is plotted as a function of the distance from the edge of the islands. This data reveals that the shift of the energy position of the peak is taking place on the same length scales for all four islands. For the corner-to-edge direction a length of 3.2 nm is extracted, for the opposite direction we find 2.5 nm.

The data presented in Fig. 6.14(a),(c) and (d), strongly suggest that the length scales of ~ 2 and ~ 3 nm, on which the spatial variation of the peak is taking place, are a general property of the Co islands which does not depend on the size of the island. The calculated in-plane Co bond length, shown in Fig. 6.14(b), also changes on a length scale of 2 nm measured from the edge and 3 nm measured from the corner. Hence, the energy position of the d-like peak seems to be closely linked to the bond length of the Co atoms within the island.

While the shift of the energy position of the peak is ascribed to an in-plane relaxation it is still not clear what the cause of the reduced peak intensity might be. The plot presented in Fig. 6.14(a) reveals, that the decay of peak intensity and the shift of the peak occur on different length scales. This observation suggests that the intensity decay is not as closely related to the relaxation within the island as the peak position. It seems that an additional effect is acting on the intensity of the peak. However, what this effect could be is not clear at the moment and cannot be concluded from experimental data alone, but theoretical support is needed.

Fig. 4.13 on page 40 reveals that the position dependence of the asymmetry peak position and intensity is exactly the same as the position dependence of the d-like peak and its intensity. From the plot of the peak positions in (b) it is concluded that the maximum in asymmetry has a constant offset to the position of the d-like Co peak of 0.03 eV. This finding reflects a strong connection of the asymmetry maximum to the spin-polarized d-like Co peak. As it is shown in the discussion of section 6.4 the dI/dV asymmetry is proportional to the spin polarization of the Co island.

In conclusion, the results discussed here demonstrate that the electronic structure within the island is highly inhomogeneous. The energy position of the d-like peak, its intensity and also the energy position of maximum asymmetry are all changing as a function of position within one island. The spatial variation of the energy position of the d-like peak is ascribed to a spatial variation of the Co bond length inside the island [24]. As all these electronic and structural properties vary, it seems very plausible that also the magnetic properties vary within the island. This view is corroborated by the calculations of Etz, who finds a spatial variation of the magnetocrystalline anisotropy and the magnetic moments within Co islands on Cu(111) [122].
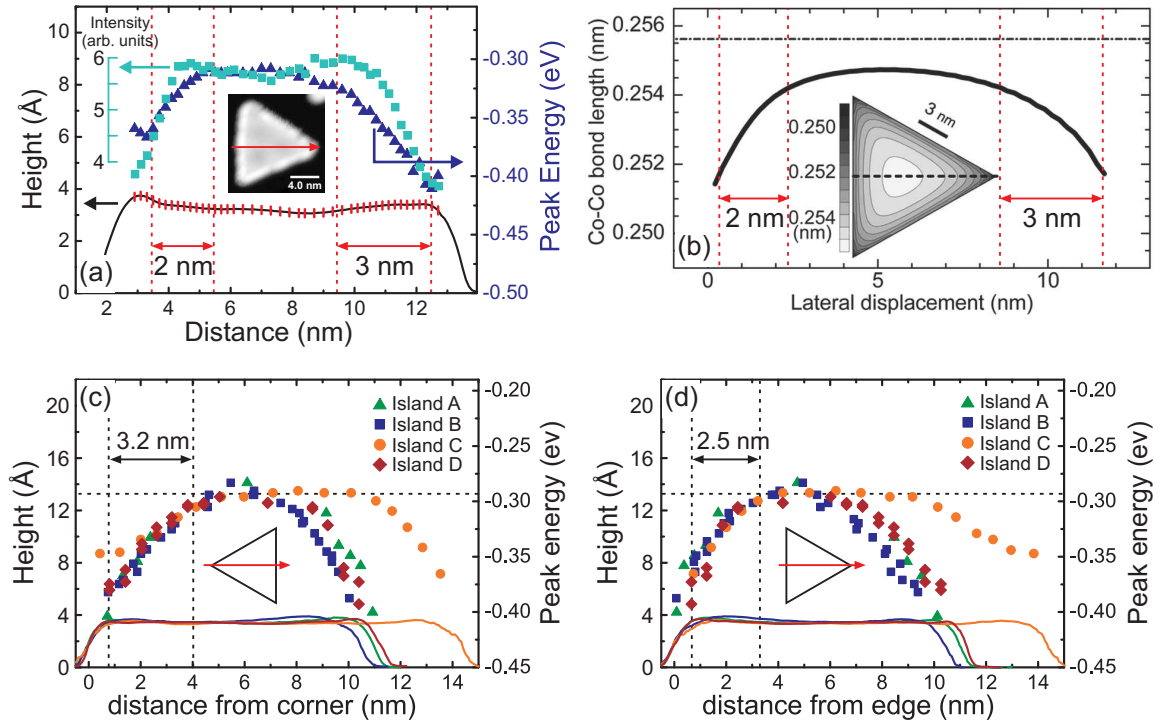
Figure 6.14: (a) Peak shift and peak intensity of the d-like surface state on a Co island on Cu(111) as a function of position (see also Fig. 4.12(a)). (b) Calculated in-plane Co-Co bond length within the top layer of a Co island along the dashed line of the inset (From [24]). (c),(d) Position dependent peak energy of the d-like peak on four other islands. Positions on the islands are measured as distance from the corner (c) and from the edge (d) of the islands. The lengths, as measured from the corner or from the edge, on which the peak position varies are the same for all islands. The length scales of the spatial variation of the peak position and the change of the bond length are very similar.

6.4 Modulated spin-polarization on top of a nanostructure

The previous three sections provided some insight into first the electronic and subsequently into the magnetic properties of Co islands on Cu(111). This section utilizes these new information, in combination with theoretical work, to discuss the spatial modulation of the spin-polarization within an individual Co island.

The experimental results presented in section 4.4 revealed a spatial modulation of the dI/dV asymmetry signal within a single Co island. It was shown that mathematically the dI/dV asymmetry A is, within certain assumptions, proportional to the product of the spin polarizations of tip P_T and sample P_S. Provided that P_T is kept constant, the sign of A depends on the dominant spin character of the sample at a given position and energy. Note, that in the experiment described above, the magnetization direction of the tip was constant and a constant external field was applied, and also the energy was fixed for each asymmetry image. Only the position of the tip was changed during the scanning process of the STM. Thus, P_T is expected to be constant and the dI/dV asymmetry is proportional to the spin-polarization of the sample, i.e. $A \propto P_S$.
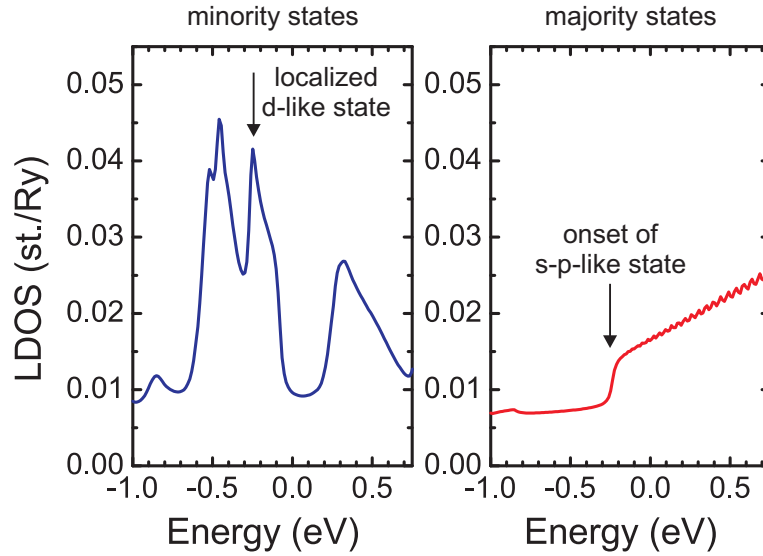
Figure 6.15: Calculated spin-resolved LDOS 4 Å above a continuous bilayer film of Co on Cu(111). The minority LDOS is dominated by localized states, the feature marked by the arrow corresponds to the peak observed in dI/dV spectra around -0.3 eV. The only feature of the majority LDOS is a kink around -0.22 eV, which marks the onset of a dispersive s-p-like state. Energy dependent modulation patterns observed in dI/dV maps of Co islands on Cu(111) are ascribed to this state. Plots adapted from [106].

The dI/dV asymmetry maps presented in Fig. 4.16 on page 43 reveal a pronounced energy dependence of the modulation patterns. Maps (c)-(e), taken at energies between $+0.25$ and $+0.51$ eV, show oscillatory changes of the sign of A as a function of position. On the other hand, maps (a) (-0.15 eV) and (f) ($+0.55$ eV) exhibit only modulations with negative sign. The asymmetry map taken very close to the Fermi energy (map (b), $+0.04$ eV) shows a positive, spatially modulated signal in the center region of the island, and a negative asymmetry at the rim of the island.

A detailed understanding of these complex experimental results is possible with the help of theory. Preliminary calculations reported by L. Niebergall et al. predicted a modulated spin-polarization within triangular Co islands on Cu(111) [30]. However, this previous work was lacking experimental evidence. This section presents an analysis of the calculated spin resolved DOS of Co on Cu(111) obtained by first principles calculations[3] in comparison with our experimental results. This provides a deeper understanding of the observed phenomena.

Figure 6.15 presents the calculated spin-resolved LDOS of a continuous bilayer film of Co on Cu(111) [106]. It reveals that the minority LDOS is dominated by several peak-like features. The feature marked by an arrow corresponds to the peak which is observed around -0.3 eV in dI/dV spectra. This localized state has a d-like character. The minority LDOS shows an additional feature left of this peak, which corresponds to a surface resonance, that occurs due to resonant scattering of
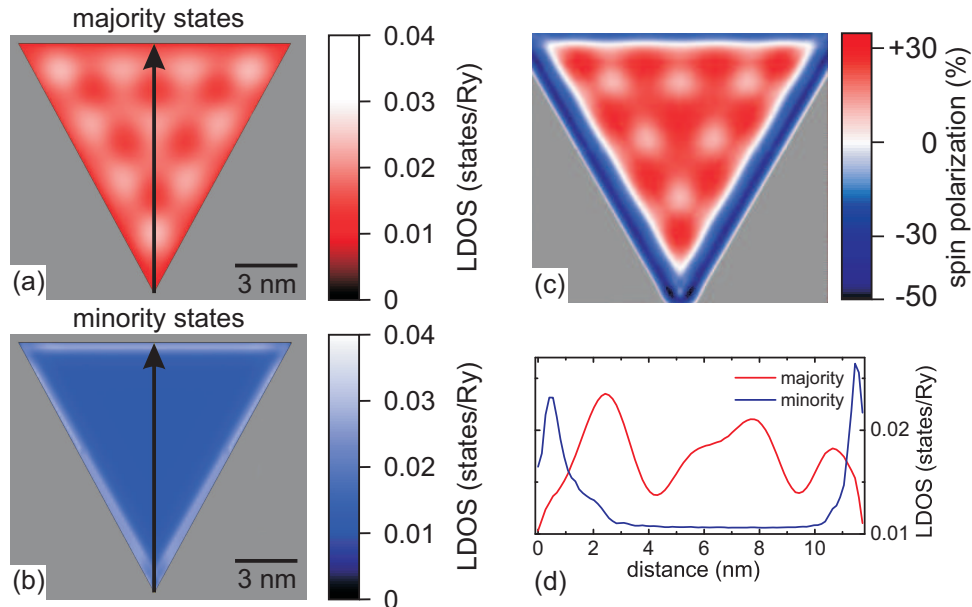
Figure 6.16: Local density of states (LDOS) calculated for a triangular 2 ML high Co island on Cu(111) at 4 Å above the island. LDOS maps are calculated for (a) majority and (b) minority states at the Fermi level. (c) Map of the spatial distribution of the spin polarization as calculated from maps (a) and (b). See text for details. (d) Line profiles along the black arrows in (a) and (b). These calculations where performed by P. Ignatiev, L. Niebergall and V.S. Stepanyuk at the MPI Halle.

bulk Bloch states of Cu at a d-band of the Co bilayer [106]. This surface resonance reflects electronic states with a higher momentum parallel to the surface than the surface state around -0.3 V. Hence, it decays much faster into the vacuum and it contributes less to the measured tunnel current (cf. section 2.2). A small peak that is frequently occurring left of the d-like peak in dI/dV spectra is ascribed to this surface resonance. The majority LDOS only shows one feature, a kink around -0.22 eV. This kink marks the onset of a s-p-like dispersive state. The energy dependent spatial modulations of the dI/dV signal observed within Co islands on Cu(111) (see above) are ascribed to this state.

Figure 6.16 shows calculated maps of the local density of states (LDOS) for majority (a) and minority (b) electrons 4 Å above a triangular bilayer high Co island on Cu(111). Calculations have been performed at this height as it resembles closely the distance of $4 - 6$ Å between tip and sample during the STM experiment (see section 3.1). The majority LDOS is modulated inside the triangular island due to the formation of standing waves caused by electron confinement of the delocalized s-p-like surface state. Contrary to that the map of the minority LDOS is constant within the island. The band structure of minority electrons is dominated by localized d-like states which are hardly affected by the confinement. At the very rim of the island (see linescan in (d)) an increase of the LDOS is observed. This observation can be explained by the existence of an electronic rim state, which is localized in space around the edges of the island and around the Fermi level in energy [89]. Pietzsch and coworkers [89], by comparing dI/dV spectra of two incidentally oppo-
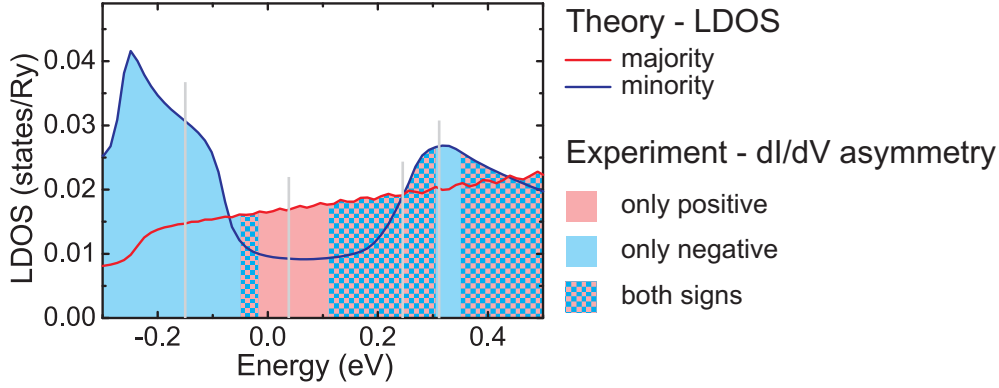
Figure 6.17: Energy dependence of the calculated LDOS above a continuous Co bilayer film on Cu(111) and the measured dI/dV asymmetry. Solid red and blue lines represent the calculated LDOS for majority and minority states, respectively. Differently shaded areas illustrate where only positive, only negative or both signs of asymmetry are observed in the experiment. Solid grey lines mark energies at which the maps of Fig. 6.18 are obtained.

sitely magnetized islands of different size, claimed, that this rim state is of minority spin character. The calculations presented here and our experimental results prove this claim for the first time.

From the two LDOS maps the spatial distribution of the spin polarization P_{Co} above the Co island is calculated by:

$$P_{Co} = \frac{LDOS_\downarrow - LDOS_\uparrow}{LDOS_\downarrow + LDOS_\uparrow} \tag{6.5}$$

where $LDOS_\downarrow$ ($LDOS_\uparrow$) is the local density of states in the vacuum region above the Co island of the minority (majority) electrons. The resulting map of the spin polarization, shown in Fig. 6.16(c), exhibits positive values in the central region of the island with a clear modulation. The rim of the island shows a negative spin polarization. It is evident that the spatial modulation of the spin polarization as seen in (c) is governed by the spatial modulation of the majority LDOS. To shed some light on the origin of the positive spin polarization at the center of the island two line profiles along the black arrows in (a) and (b) are presented in (d). They reveal that the modulated majority LDOS is higher than the spatially flat minority LDOS within the central region of the island, i.e. $LDOS_\uparrow - LDOS_\downarrow > 0$ and also $P_{Co} > 0$. At the rim the situation is reversed, leading to a negative P_{Co}.

A comparison of the calculated spin polarization of Fig. 6.16(c) with the experimental dI/dV asymmetry map presented in Figs. 4.16(b) and 6.18(b) demonstrates a good agreement within the island. This result leads to two important conclusions. Firstly, the dI/dV asymmetry map reflects qualitatively the spatial distribution of the spin polarization of the Co island at the energy chosen by the gap voltage. Secondly, the modulation pattern observed in the dI/dV asymmetry map originates essentially from the modulations in the majority spin channel, which are caused by confinement of the free-electron-like majority surface state. The sign of the modulated spin polarization is determined by the magnitude of the, in the center, spatially constant minority states as compared to the spatially modulated majority states.

The experimental data presented earlier revealed a pronounced energy dependence of the asymmetry modulation patterns. Hence, corresponding calculations of the spin polarization have been performed. Figure 6.17 shows the calculated spin-resolved LDOS 4 Å above a bilayer thick continuous Co film on Cu(111). The majority LDOS increases monotonically with energy and shows a kink around −0.2 eV. This point marks the beginning of the s-p surface state which is dispersing with energy and is causing the modulation patterns within the Co islands. The minority LDOS is dominated by two broad features around ≈ −0.25 eV and +0.3 eV which can both be identified as localized d-like surface states. From this data it is obvious that the spin-polarization of the Co film highly depends on the energy and that it is expected to change sign at various energies.

The filling of the curve connects the theory predictions for a continuous film with the experimental observations made for the islands. The colors indicate the sign of dI/dV asymmetry observed at the various energies. Energy ranges where the minority LDOS is dominant show a mainly negative asymmetry (blue) whereas in areas governed by the majority LDOS mainly positive values (red) or a mixture of positive and negative values (blue red checkered) are observed.

Figure 6.18 presents maps of the experimentally obtained dI/dV asymmetry at different energies (a)-(d) and the corresponding maps of the spin polarization calculated at the same energies (e)-(h). The latter have been produced in the same manner as the data in Fig. 6.16. At −0.15 eV (Fig. 6.18(a),(e)) the peak in the minority LDOS exceeds the level of the majority LDOS and the spin polarization becomes negative in the central region of the island. The light modulation of P within the island is only due to the spatial modulation of the majority LDOS. The minority LDOS is dominated by a localized and spatially flat d-like feature in this energy range[4]. The situation is reversed close to the Fermi energy. Here the magnitude of the majority LDOS exceeds that of the minority states, and the center of the island exhibits a positive spin polarization. As discussed above, the rim of the island shows a negative spin polarization. This is ascribed to the appearance of a localized minority state [89].

At +0.25 eV the curves of the minority and majority LDOS cross (see Fig. 6.17), and thus the net spin polarization is expected to be zero. However, Fig. 6.18(g) shows, instead of a constant zero signal, a modulation around zero including positive and negative values. The reason for that is again the spatial modulation of the majority LDOS due to electron confinement within the island. This causes local deviations of the majority LDOS from the constant value predicted for a continuous Co film. Thus the majority LDOS is lower, higher or equal to the minority LDOS at positions where the standing waves have their minima, maxima or nodes, and the resulting spin polarization is negative, positive or zero, respectively.

With increasing energy the situation changes again. Around +0.30 eV the mi-

---

[4]At the rim of the island a positive spin polarization is observed by the experiment, which is not reproduced by the calculations. This discrepancy is caused by the fact that the calculations do not take into account structural relaxations [130, Supporting online material], which were shown to influence the energy position of the d-like minority state (cf. section 6.3.1). Secondly, the electronic structure at the rim of the island is mimicked in the calculations by inserting special Co potentials at edges. This method gives a good agreement between the theoretical and experimental edge states only at the Fermi energy. However, these limitations of the theoretical model do not affect the main conclusions drawn here.
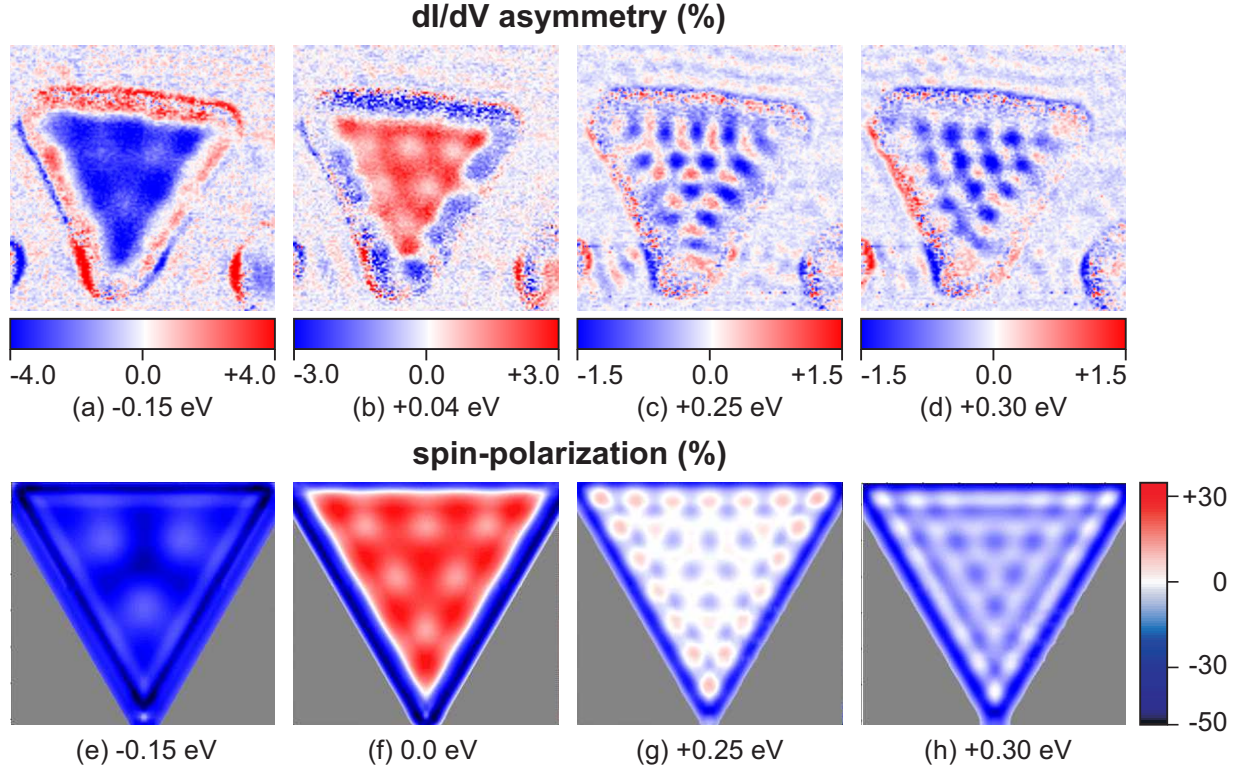
dI/dV asymmetry (%)

-4.0   0.0   +4.0   -3.0   0.0   +3.0   -1.5   0.0   +1.5   -1.5   0.0   +1.5
   (a) -0.15 eV   (b) +0.04 eV   (c) +0.25 eV   (d) +0.30 eV

spin-polarization (%)

   (e) -0.15 eV   (f) 0.0 eV   (g) +0.25 eV   (h) +0.30 eV

Figure 6.18: Energy dependent spatial variations of the measured dI/dV asymmetry and the calculated spin-polarization. (a)-(d) Maps of the dI/dV asymmetry obtained at the energies stated. Each asymmetry map is calculated from two dI/dV images measured at AP and P states using Eq. 4.1. Imaging conditions: $B = -1.1$ T, $I_{Stab} = 1.0$ nA, $V_{Stab} = +0.5$ V (e)-(h) Maps of the spin-polarization obtained at the same energies as the dI/dV maps. These maps are calculated from a pair of LDOS maps for majority and minority states using Eq. 6.5.

nority states are dominant, as can be seen from Fig. 6.17. Consequently a negative spin polarization is observed within the island. Note, that here the signal is oscillating between zero and a negative level and the experimental results even show some spots with positive values. This can be explained by the smaller difference between minority and majority LDOS as compared to the situation at -0.15 eV, where the minority states exceed the majority level by almost 100 %.

Comparing the two sets of images of Fig. 6.18 reveals an overall good agreement between theory and experiment, i.e. the energy dependence of the modulation patterns observed in experiment is very well resembled by the calculations. Thus, the first interpretation, that the modulation and change of sign of the dI/dV asymmetry is due to a spatial superposition of s-p-like majority and d-like minority states, is strongly supported by these results. These findings also corroborate our statement that the measured dI/dV asymmetry is proportional to the spin polarization of the sample.

As stated above, the electronic structure at the rim of the island is dominated by a so-called rim state around the Fermi energy [89]. Our data on the spatial distribution
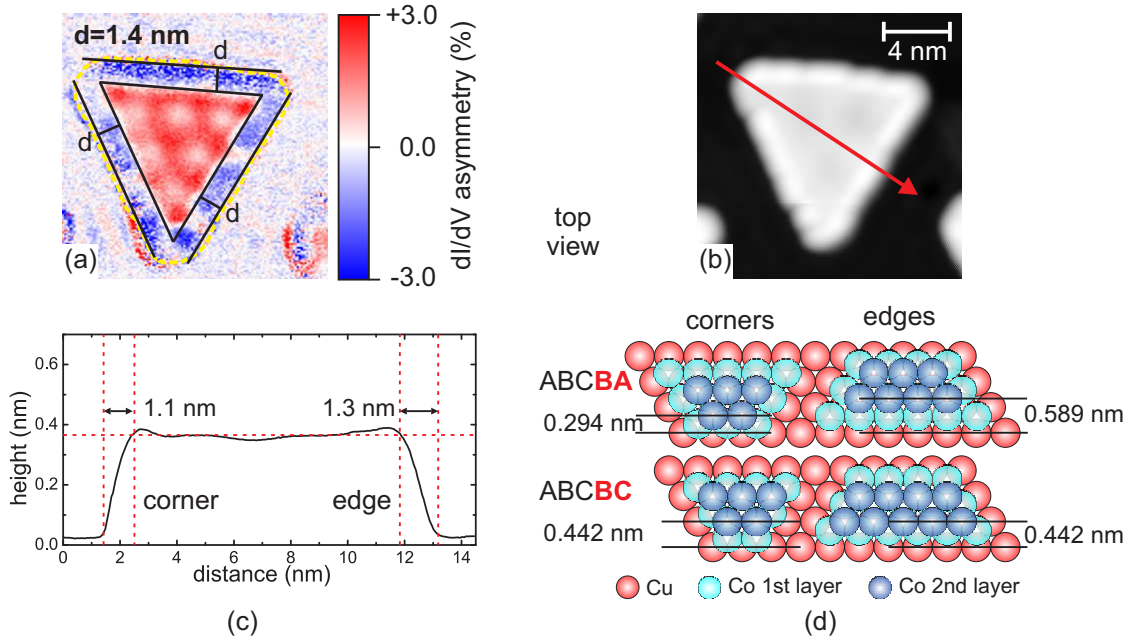
Figure 6.19: Spatial extension of the rim state. (a) Map of the dI/dV asymmetry at +0.04 eV. The width of the area with negative asymmetry is $d = 1.4$ nm. The yellow dashed line marks the topographic dimensions of the island, as extracted from (b). (b) STM topography of the same island. Imaging conditions: $V_{Gap} = -0.1$ V, $I_T = 1$ nA, $T = 8.3$ K. (c) Line scan along the red arrow in (b). The apparent width of the corner microfacet amounts to 1.1 nm, that of the edge microfacet to 1.3 nm. (d) Top view on a hard sphere model of the corner and edge facets according to [22]. The two stacking orders possible for the investigated island are shown and the calculated facet widths are denoted.

of the spin polarization reveal the spatial extension of this state. Figure 6.19 presents a dI/dV asymmetry map obtained at +0.04 eV. The blue colored area at the edges is ascribed to the rim state, its width is determined to be 1.4 nm. To estimate the "real" width of the spatial extension of the rim state, the influence of the finite radius of the tip apex needs to be considered. Fig. 6.19(b) presents a topography image of the island studied in (a), and a line scan through this data is presented in (c). As outlined in the experimental section 3.2 previous theoretical work [22] identified four possible stacking orders for bilayer Co islands on Cu(111), which can be classified as faulted and unfaulted. The island examined here is identified as a faulted island[5].

Fig. 6.19(d) shows a hard sphere model of the island corners and edges corresponding to the two possible faulted stacking orders. The width of the microfacets formed at the corners and edges are calculated according to this model. For the ABCBA stacking the model yields a width of $2a_{Cu}/\sqrt{6} = 0.294$ nm for the corner facet and $4a_{Cu}/\sqrt{6} = 0.589$ nm for the edge facet. The ABCBC stacking results in the same width at the corner and gives at the edge $3a_{Cu}/\sqrt{6} = 0.442$ nm. The

---

[5] As outlined before in section 3.2, this identification is possible through a statistical analysis of large scale STM images.

line scan shown in (c) reveals an apparent width of 1.1 nm for the corner microfacet and 1.3 nm for the edge microfacet. Since the width of the corner facet is smaller than that of the edge facet, it is concluded that the island most likely follows the ABCBA stacking.

Independent of the precise stacking order, the width of the facets is overestimated in STM topography by 0.7 nm. The major causes of such an overestimation are the finite radius of the tip apex and the electronic structure of tip and sample. We have to keep in mind that the signal obtained by constant current STM measurements is always a convolution of the electronic structure and the morphology of the sample with the electronic structure of the tip and its apex radius. Nevertheless, the 0.7 nm, by which the calculated facet width is overestimated, are a good estimate for an *effective* tip radius, including the effects mentioned above.

This effective tip radius leads to a broadening of the apparent width of topographic obstacles like step edges or clusters. However, its influence on the lateral resolution of flat surfaces is much smaller. Since, the major part of the blue colored rim area is on top of the island, and not at the edge directly, it is concluded that the width of the spatial extension of the rim state might be overestimated by ~ 0.3 nm and amounts to $d \sim 1.1$ nm. Pietzsch et al. [89] estimated from their topography and dI/dV images of different Co islands a larger width of 1.7 ± 0.2 nm. Our analysis presented here, visualizes the rim state area of *one individual* island directly for the first time, and gives therefore a better estimate of the real spatial extension of the rim state.

The width of the rim state most probably also affects the characteristic length crucial for electron confinement within the island. The discussion presented in section 6.1 revealed that the characteristic length for electron confinement within the island is dominated by the geometric height of the triangular shaped islands. However, the analysis of the wave-vector quantization (see Fig. 6.3) also revealed that the characteristic lengths are $1.3 - 3.8$ nm shorter than the corresponding heights. If this reduction was only caused by the rim state then it should have a value of at least twice the width of the rim state or 2.2 nm. Hence, it is concluded that the occurrence of the additional state at the rim of the islands is affecting the electron confinement, but it is not the only mechanism influencing the observed phenomena.

A close inspection of Fig. 6.18(a)-(d) reveals that the dI/dV asymmetry on the Cu substrate around the island also exhibits a light modulation, which changes with energy. This rather surprising observation indicates that scattering of electrons of the Cu surface state at the edges of Co islands induces a modulated spin polarization also in the Cu surface state. This effect and its spatial variation have not been studied with STM on the nanometer scale so far. Hence, this highly interesting topic is a subject of current studies of this system at the MPI Halle.

6.5   Co nanorods on Cu(110)-p(2×3)N

In this section the experimental results obtained on the morphology and electronic structure on Co nanorods on the Cu(110)-p(2×3)N (Cu$_3$N) surface are analyzed and discussed.
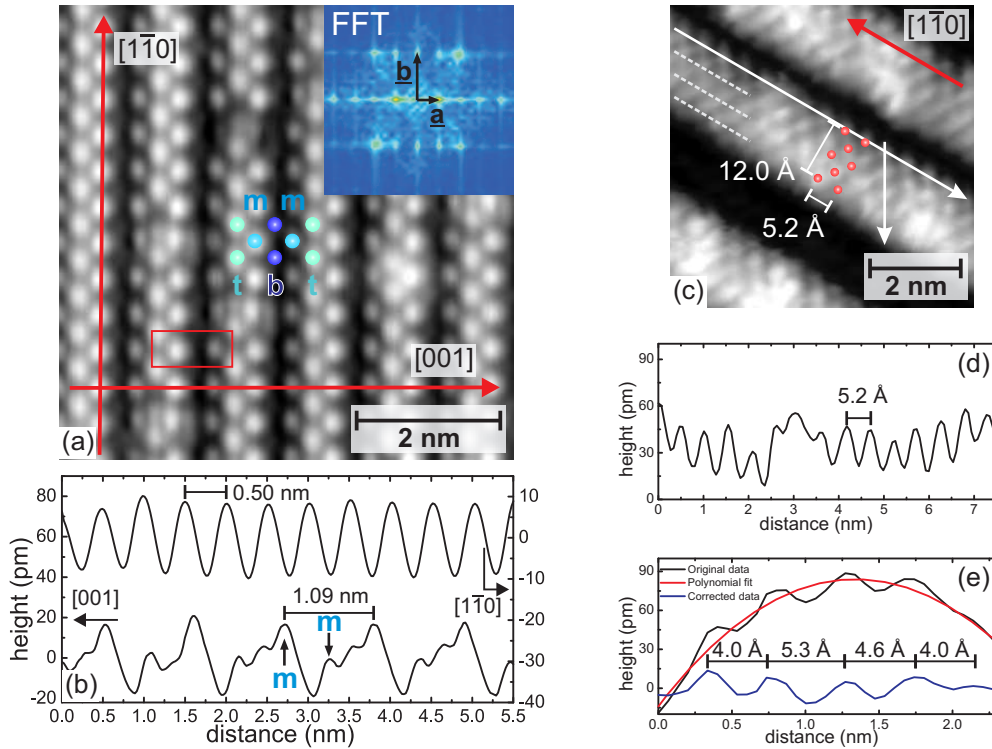
Figure 6.20: Atomically resolved STM topography images of Cu(110)-p(2×3)N and Co wires grown on top (see also Figs. 5.1 and 5.3). (a) Cu_3N network grown on Cu(110). Imaging conditions: $V_{Gap} = +0.2$ V, $I_T = 10$ nA, $\phi = 90°$, $T = 8.3$ K. (b) Line scans along the red arrows. Atom positions according to a previous model [35] are denoted by blue circles. (c) Co wires grown on top of Cu_3N, zoom-in of Fig. 5.3. Red circles mark atom positions according to [35]. (d),(e) Line scans along the white arrows in (c).

In a recent publication Ma and coworkers investigated this system by STM [35]. With the help of ab-initio calculations they proposed a structure model for this surface. The authors find a good agreement of the model with their STM data, however, they were not able to resolve all atomic positions of the model unit cell. This is done here. Fig. 6.20(a) resolves all atom positions predicted by the model. FFT and the line scans shown in (b) give the unit vectors as $\underline{a} = 1.094$ nm and $\underline{b} = 0.502$ nm. These results are in perfect agreement with the previously proposed model [35], which determined $\underline{a} = 1.09$ nm and $\underline{b} = 0.50$ nm.

However, the data presented here shows an asymmetry of the nitrogen rows, that was not reported before. Here, atoms occupying middle positions ("m") exhibit different apparent heights. Middle atoms located left of the top atoms ("t") exhibit a smaller apparent height as compared to middle atoms located on the right side. This is also evident from the line scan presented in (b). The cause of this apparent asymmetry is not clear yet.

Figure 6.20(c) presents the zoom-in of an atomically resolved constant current STM image of Co wires grown on top of the Cu_3N surface (cf. Fig. 5.3 on page 48). Recent calculations [35] reveal that the growth of the nanowires is guided by strain relief at the surface. The same publication proposes a model for the morphology of

the Co wires with a unit cell of 5.1×10.8 Å. From our results we extract a unit cell for the wire of 5.2×12.0 Å. Thus, the short unit vector extracted from our data is in good agreement with the proposed model, whereas the longer unit vector is 1 Å longer than in the model. This deviation might be caused by a convolution of the electronic structure of the wire with topographic information. As the data presented in Fig. 5.5 reveals, the Co wires appear much wider in dI/dV maps than in topography images. Hence, it seems plausible that the convolution of electronic and structural properties leads to larger apparent width of the Co wires.

The model of Ma claims a width of the wires of five atoms. However, the same model reveals that the middle row is deeply embedded into the Cu_3N network and is therefore possibly not visible in STM. The line scan presented in Fig. 6.20(e) is obtained along the close packed direction of the wire, which has a $60°$ angle with the long axis of the wire. Along this direction the previous model proposes five Co atoms with a distance of 3.6 Å. The line scan reveals only four maxima, which are ascribed to atom positions, with distances between 4.0 and 5.3 Å. The largest distance is observed between the second and the third maximum, which would support the picture, that the middle atom is too deeply embedded into the structure to be resolved by STM. The distance between the first and the last of the five atoms in the model published previously [35] is 4×3.6 Å$= 14.4$ Å. This number is in close agreement with the 13.9 Å obtained from the line scan. In conclusion the results presented here support, apart from minor deviations, the model proposed previously [35].

The electronic structure of both the Cu_3N surface and the Co nanorods grown on top of it are investigated by $dI/dV|_{\Delta Z}$ spectroscopy measurements. This special spectroscopy mode was chosen, since the normal dI/dV spectroscopy, where the tip-sample distance is kept constant during measurement, exhibits an exponential increase of the signal with increasing voltage. This behavior reflects the exponential dependence of the tunnel current on the height of the tunnel barrier, which is decreasing exponentially with increasing bias. This fundamental characteristics limits the range of bias voltage that can be applied to obtain meaningful spectroscopy data at a constant tip-sample distance to approx. ± 2 V.

A common feature of all $dI/dV|_{\Delta Z}$ spectra presented in chapter 5 are pronounced peaks at energies above $+5$ eV. These peaks are identified as image potential states (IPS) forming in front of the surface due to the electric field between tip and sample surface [96, 131] (see section 3.1). In STS measurements IPS can be easily discriminated from other electronic states since they are shifting to higher energies upon increasing the I_T set point, i.e. upon moving the tip closer to the surface. This is demonstrated in Figure 6.21. The plot shows two $dI/dV|_{\Delta Z}$ spectra measured at the same position on Cu(110) at different set points. Changing I_T from 1 nA (black line) to 10 nA (red line) leads to a shift of the peak series to higher energies and to an increase of their periodicity. Hence, it is concluded that the first of these peaks marks the first IPS. This study focuses on electronic features positioned between $+1$ eV and the first IPS. The first IPS is always marked by an arrow in $dI/dV|_{\Delta Z}$ spectra.

The first IPS of Cu_3N is positioned around $+5.8$ V. The spectra of Fig. 5.2 on page 47 exhibit another four features below that energy. The peaks marked at $+1.9$
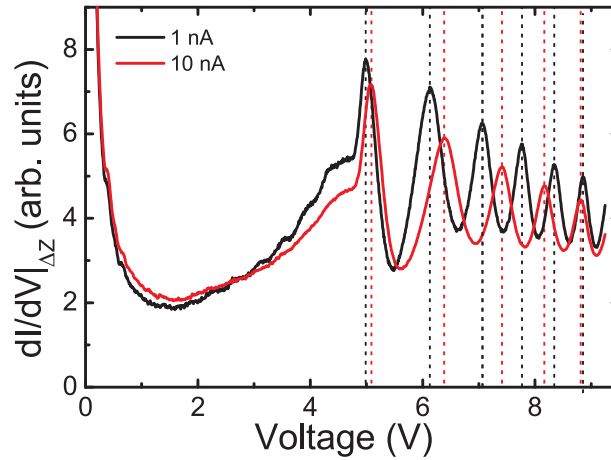
Figure 6.21: $dI/dV|_{\Delta Z}$ spectra measured on Cu(110) at two different stabilization points. At 10 nA the series of peaks is shifted to higher energies and also the distance between the peaks is increasing. Dotted lines mark the peak centers for each spectrum. The first peak in each of the spectra is ascribed to the first image potential state.

and +3.3 V have been observed routinely in the experiments and also with different tips. Hence, they are attributed to the electronic structure of the sample. However, the physical origin of these peaks in terms of band structure is still unknown and currently theoretical efforts are under way to clarify this point [132].

The electronic structure of the Co wires is studied by single point $dI/dV|_{\Delta Z}$ spectroscopy and by measuring dI/dV maps. Figure 5.4 presents point spectra measured on a Co wire in the dI/dV and in the $dI/dV|_{\Delta Z}$ mode. In both spectroscopy modes a peak is observed in the spectra at +1.8 eV. Since the peak is observed in the dI/dV mode with constant tip-sample distance, it indicates the existence of an unoccupied localized state of the sample at this energy.

Figure 5.5(b) taken at +1.8 eV shows pronounced spatial variations of the dI/dV signal, which are ascribed to corresponding changes of the LDOS within the wires. One possible cause for the spatial variations of the LDOS is the formation of standing wave patterns due to electron confinement along the wires. This assumption would require a delocalized dispersive surface state or surface resonance within the wires [133]. Standing waves forming in the LDOS due to the confinement of such surface state electrons within the wires would lead to highly periodical modulation patterns, whose wave-length decreases with increasing energy. The data presented in Fig. 5.5 do not show such a behavior. Hence, the idea of electron confinement can be discarded.

In conclusion the source of the spatial variations of the LDOS within the wires is not clear yet. They might be caused by chemical impurities, invisible in STM topography data, or by relaxation effects that lead only to minute changes of the atomic structure but dramatically affect the electronic structure. The latter behavior is for example observed for the Co islands on Cu(111) [24]. Presently we cannot further our understanding of this issue.

As described above the electronic structure of the Co wires around +1.8 eV

is highly inhomogeneous. At this energy the dI/dV maps show bright and dark areas within the wires. To investigate this effect in more detail $dI/dV|_{\Delta Z}$ spectra are measured on bright and dark spots within the wires and also at one position between the wires. The resulting spectra are presented in Fig. 5.6 on page 51. The main result of these measurements is that the position of the peak around $+1.8$ eV slightly varies at the different positions, whereas the peak around $+3.6$ eV remains unchanged. These results suggest that the second peak is closely related to the underlying Cu_3N substrate, since the peak stays at one energy even for different positions on the sample. However, the first peak is indeed changing with position and thus seems to be governed by the local chemical and structural environment within and around the Co wires. This view is supported by the fact that this peak also appears in dI/dV spectra obtained at a constant tip-sample distance. Furthermore this idea would also fit into the picture that local relaxation within the wires is causing the observed inhomogeneities of the LDOS within the wires, since relaxation within Co islands on Cu(111) is known to cause a shifting of the energy position of the d-like Co peak around -0.3 eV [24].

In conclusion the above results present the first study of the electronic structure of Cu(110)-p(2×3)N and of Co wires grown on top. This study reveals that the electronic structure of the wires is very similar to that of the Cu_3N substrate. This suggests a strong electronic coupling of the wires to the substrate. Hence, the Cu(110)-p(2×3)N surface does not seem to be a good candidate for studying the decoupled electronic structure of objects grown on top of it. The data gathered on the electronic properties of the Co wires are an important prerequisite for future studies of their magnetic properties by spin-STM. As illustrated in section 6.2, some knowledge of the electronic structure of the sample, to be studied by spin-STM, is needed, for the necessary in-situ preparation of magnetic tips. Without this information, it becomes very challenging to prepare magnetically sensitive tips.

A recent study by Ma [34] found the magnetic easy axis being perpendicular to the wire axis. This result comes as a surprise, since one would expect, that the wires should exhibit a strong shape anisotropy forcing the easy magnetization axis to be along the wire. This effect is for instance well known for needle shaped Fe whiskers, whose easy magnetization axis is parallel to their long axis [134]. The unexpected results of [34], obtained by magneto-optical Kerr effect (MOKE) and X-ray magnetic circular dichroism (XMCD) measurements, calls for an independent future cross check on the atomic scale done by spin-STM.

Chapter 7

Conclusions and Outlook

In this work the electron confinement within Co islands on Cu(111) and within a Cu stripe on Cu(111) was investigated. The energy dependence of standing wave patterns occurring within the two systems was analyzed and yielded the dispersion relation of the surface state electrons of both systems. The dispersion relation is discrete in the wave-vector in both cases. It was demonstrated, that the essential aspect of the discrete dispersion relation can be quantitatively described by electron wave vector quantization. We find that the wave vector quantization follows a simple quantization rule, whose only parameter is the characteristic length of the system. For the Cu stripe this characteristic length was revealed to be the width of the stripe. We find that the decisive length scale for a triangular Co island is the geometrical height of the triangle.

The analysis of the standing wave patterns also yielded the full spectrum of eigenstates for the Cu stripe and for the Co islands. It was shown, that the previously used method of identifying maxima in single point dI/dV spectra obtained at high symmetry points of the investigated system as eigenstates fails to identify all eigenstates. It was outlined that minima *and* maxima identify eigenstates. Furthermore it was demonstrated that the previously used Fabry-Pérot model fails to predict all eigenstates. Our approach does not rely on the exploitation of measurements at the high symmetry points required for the application of the previous approaches. This resembles an important progress in the description of electron confinement.

A new approach to spin-polarized scanning tunneling microscopy was introduced in this thesis. This new approach comprises measurements of the differential conductance (dI/dV) in an external magnetic field, performed with a tip covered with magnetic material. The method allows to measure dI/dV hysteresis loops of individual particles. It was shown that a careful analysis of these hysteresis loops allows for a identification of tip and sample contributions to the measured dI/dV signal. Thereby an unambiguous and reliable identification of parallel (P) and antiparallel (AP) orientations of tip and sample magnetizations is possible for the first time in spin-STM measurements. Our new approach also reveals that the established assignment of a high dI/dV signal to P and a low dI/dV signal to AP magnetization configurations is not always correct, and that depending on the applied bias a high dI/dV signal can identify a P as well as an AP configuration.

It was shown that, in contrast to the common picture, the magnetic configura-

tion of a tip and its change in an external field depends on both the macroscopic preparation by film coverage and on the microscopic preparation by voltage pulses. This characterization of the tip is the decisive prerequisite for a reliable analysis of the magnetic properties of the sample. One unexpected result in this context was, that the magnetization orientation of tips covered with Cr can be influenced by an external magnetic field of several hundred mT, in contrast to the previous description in the literature.

The switching field of individual particles, of single Co islands on Cu(111), was extracted from hysteresis loops of the dI/dV signal. This work presents the first spin-STM study of the size and temperature dependence of the switching field of individual nanoparticles. For single Co islands with sizes between 1000 and 20000 atoms we found switching fields of the order of $1 - 2$ T at 8 K. We analyzed the size as well as the temperature dependence of the switching field within the simple Néel-Brown model of thermally assisted coherent magnetization reversal. We identify a clear failure of this model for Co islands on Cu(111). Nevertheless, an estimate for the lower limit of the magnetocrystalline anisotropy was obtained from this analysis, yielding a value of ~ 2 MJ/m^3 (0.16 meV/atom). This value is approx. four times higher than the value reported for bulk Co. The failure of the Néel-Brown model indicates that the magnetization reversal may involve non-coherent processes. This conjecture was supported by our study of the spatial dependence of the electronic structure within the Co islands.

This work revealed pronounced spatial variations of the electronic structure within one Co island. These variations were linked to changes of the in-plane bond length of Co atoms within a single Co island. The inhomogeneous electronic structure and the corresponding structural variations lead to the expectation that also the magnetic properties of the Co islands are non-uniform within the islands. This picture is corroborated by preliminary ab-initio calculations by C. Etz from the MPI Halle. In conclusion, the high anisotropy, the failure of the Néel-Brown model and the indications for inhomogeneities in the magnetic properties of the Co islands are all vigorous hints, that the magnetization reversal of Co islands on Cu(111) is a non-coherent process.

Our new approach to spin-STM enabled us to study spin-polarized electron confinement for the first time. Maps of the dI/dV asymmetry were found to reflect the spin-polarization of the sample. We studied the energy dependence of the spin-polarization within a single Co island on Cu(111) and found a pronounced spatial modulation of the spin-polarization. Our results were analyzed with the help of ab-initio calculations of the spin-resolved electronic structure of the Co islands. It was found that the energy dependent modulation patterns of the spin-polarization within the island can be ascribed to the energy dependence of the relative magnitudes of minority and majority surface states. Our results also present the first experimental evidence for a spin dependent scattering of Cu(111) surface state electrons at the edges of the Co islands.

We also studied Co wires on Cu(110)-p(2×3)N by STM and STS. The first study of the electronic properties of this system was presented, and indications for a strong electronic coupling of the Co wires to the substrate were found. Thus, unlike Cu$_2$N on Cu(100), Cu(110)-p(2×3)N does not seem to be a good candidate for studies

of the decoupled electronic and magnetic properties of particles grown on top of it. Within the Co wires pronounced spatial variations of the local density of states were found, which also vary significantly with energy. A thorough understanding of this result is still missing and calls for input from theory. The data on the electronic properties of the Co wires presented in this work may serve as a basis for future spin-STM investigations of this system.

In view of the results presented in this thesis, it would be highly interesting to apply our new method of spin-STM also to other systems in the future. For example the magnetic properties of Co islands on Pt(111) and on Au(111) have only been investigated by averaging methods like magneto-optical Kerr effect measurements and X-ray magnetic circular dichroism. A study of the switching field of single Co islands also on those substrates, might possibly gain new insight into the influence of the substrate on the observed switching fields. Due to the different magnetic polarizability of Cu, Pt and Au notable differences of the switching fields of the Co islands are expected. From the experimental point of view it would be nice to have an external magnetic field, which can be applied in all directions. This would enable the measurement of hysteresis loops of single islands along their hard magnetization axis. Such hysteresis loops would offer a more direct way to estimate the magnetic anisotropy of the islands.

Also the exciting new results on the spin-polarization induced in the Cu(111) surface state, presented here, are a strong motivation for further investigations. It is for instance not a-priori clear how two neighboring and oppositely magnetized Co islands will influence the spin-polarization of the Cu(111) surface state. Our results obtained for the spatial modulation of the spin-polarization within the Co islands might also contribute to the growing field of spintronics, where the tailoring of magnetic and at the same time electronic properties of nanostructures is desired. A tailoring of the spin-polarization within the Co islands seems possible by changing their size and/or shape.

Bibliography

[1] M. F. CROMMIE, C. P. LUTZ, and D. M. EIGLER, *Nature* **363**, 524 (1993).

[2] Y. HASEGAWA and P. AVOURIS, *Phys. Rev. Lett.* **71**, 1071 (1993).

[3] I. M. L. BILLAS, A. CHTELAIN, and W. A. D. HEER, *Science* **265**, 1682 (1994).

[4] J. SHEN, R. SKOMSKI, M. KLAUA, H. JENNICHES, S. S. MANOHARAN, and J. KIRSCHNER, *Physical Review B* **56**, 2340 (1997).

[5] J. SHEN and J. KIRSCHNER, *Surface Science* **500**, 300 (2002).

[6] G. BINNIG, H. ROHRER, C. GERBER, and E. WEIBEL, *Appl. Phys. Lett.* **40**, 178 (1982).

[7] G. BINNIG and H. ROHRER, *Surf. Sci.* **126**, 236 (1983).

[8] W. J. KAISER and R. C. JAKLEVIC, *IBM J. Res. Dev.* **30**, 411 (1986).

[9] M. BODE, *Rep. Prog. Phys.* **66**, 523 (2003).

[10] W. WULFHEKEL and J. KIRSCHNER, *Annu. Rev. Mater. Res.* **37**, 69 (2007).

[11] P. GAMBARDELLA, S. RUSPONI, M. VERONESE, S. S. DHESI, C. GRAZIOLI, A. DALLMEYER, I. CABRIA, R. ZELLER, P. H. DEDERICHS, K. KERN, C. CARBONE, and H. BRUNE, *Science* **300**, 1130 (2003).

[12] A. F. OTTE, M. TERNES, K. VON BERGMANN, S. LOTH, H. BRUNE, C. P. LUTZ, C. F. HIRJIBEHEDIN, and A. J. HEINRICH, *Nature Physics* **4**, 847 (2008).

[13] C. L. GAO, U. SCHLICKUM, W. WULFHEKEL, and J. KIRSCHNER, *Phys. Rev. Lett.* **98**, 107203 (2007).

[14] M. CROMMIE, C. LUTZ, D. EIGLER, and E. HELLER, *Surf. Rev. Lett.* **2**, 127 (1995).

[15] P. AVOURIS, I.-W. LYO, R. E. WALKUP, and Y. HASEGAWA, *J. Vac. Sci. Tech. B* **12**, 1447 (1994).

[16] O. PIETZSCH, A. KUBETZKA, M. BODE, and R. WIESENDANGER, *Phys. Rev. Lett.* **92**, 057202 (2004).

[17] Y. Yayon, V. W. Brar, L. Senapati, S. C. Erwin, and M. F. Crommie, *Phys. Rev. Lett.* **99**, 067202 (2007).

[18] C. Iacovita, M. V. Rastei, B. W. Heinrich, T. Brumme, J. Kortus, L. Limot, and J. P. Bucher, *Phys. Rev. Lett.* **101**, 116602 (2008).

[19] J. de la Figuera, J. E. Prieto, C. Ocal, and R. Miranda, *Phys. Rev. B* **47**, 13043 (1993).

[20] M. T. Kief and W. F. Egelhoff, *Phys. Rev. B* **47**, 10785 (1993).

[21] J. de la Figuera, J. E. Prieto, G. Kostka, S. Muller, C. Ocal, R. Miranda, and K. Heinz, *Surf. Sci.* **349**, L139 (1996).

[22] N. N. Negulyaev, V. S. Stepanyuk, P. Bruno, L. Diekhöner, P. Wahl, and K. Kern, *Phys. Rev. B* **77**, 125437 (2008).

[23] L. Diekhöner, M. A. Schneider, A. N. Baranov, V. S. Stepanyuk, P. Bruno, and K. Kern, *Phys. Rev. Lett.* **90**, 236801 (2003).

[24] M. V. Rastei, B. Heinrich, L. Limot, P. A. Ignatiev, V. S. Stepanyuk, P. Bruno, and J. P. Bucher, *Phys. Rev. Lett.* **99**, 246102 (2007).

[25] P. A. Ignatiev, V. S. Stepanyuk, L. Niebergall, P. Bruno, and J. Berakdar, *Euro. Phys. J. D* **45**, 547 (2007).

[26] E. F. Kneller and F. E. Luborsky, *J. Appl. Phys.* **34**, 656 (1963).

[27] T. Chang and J. G. Zhu, Angular dependence measurement of individual barium ferrite recording particles near the single domain size, in *38th Annual Conference on Magnetism and Magnetic Materials*, volume 75, pp. 5553–5555, AIP, 1994.

[28] W. Wernsdorfer, E. B. Orozco, K. Hasselbach, A. Benoit, B. Barbara, N. Demoncy, A. Loiseau, H. Pascard, and D. Mailly, *Phys. Rev. Lett.* **78**, 1791 (1997).

[29] S. Rusponi, T. Cren, N. Weiss, M. Epple, P. Buluschek, L. Claude, and H. Brune, *Nat. Mater.* **2**, 546 (2003).

[30] L. Niebergall, V. S. Stepanyuk, J. Berakdar, and P. Bruno, *Phys. Rev. Lett.* **96**, 127204 (2006).

[31] F. Leibsle, S. Dhesi, S. Barrett, and A. Robinson, *Surf. Sci.* **317**, 309 (1994).

[32] F. M. Leibsle, R. Davis, and A. W. Robinson, *Phys. Rev. B* **47**, 10052 (1993).

[33] F. M. Leibsle, R. Davis, and A. W. Robinson, *Phys. Rev. B* **49**, 8290 (1994).

[34] X. D. MA, T. NAKAGAWA, Y. TAKAGI, M. PRZYBYLSKI, F. M. LEIBSLE, and T. YOKOYAMA, *Phys. Rev. B* **78**, 104420 (2008).

[35] X.-D. MA, D. I. BAZHANOV, O. FRUCHART, F. YILDIZ, T. YOKOYAMA, M. PRZYBYLSKI, V. S. STEPANYUK, W. HERGERT, and J. KIRSCHNER, *Phys. Rev. Lett.* **102**, 205503 (2009).

[36] E. C. STONER and E. P. WOHLFARTH, *Phil. Trans. R. Soc. A* **240**, 599 (1948).

[37] E. STONER and E. WOHLFARTH, *IEEE T. Magn.* **27**, 3475 (1991).

[38] L. NÉEL, *Comptes rendus hebdomadaires des séances de l'Académie des Sciences* **228**, 664 (1949).

[39] W. F. BROWN, *Phys. Rev.* **130**, 1677 (1963).

[40] C. J. CHEN, *Introduction to scanning tunneling microscopy*, Monographs on the physics and chemistry of materials ; 64, Oxford University Press, Oxford, 2. edition, 2008.

[41] D. A. BONNELL, *Scanning probe microscopy and spectroscopy. Theory, techniques, and applications*, Wiley-VCH, New York, NY, 2. edition, 2001.

[42] C. BAI, *Scanning tunneling microscopy and its applications*, Springer series in surface sciences ; 32, Springer, Berlin, 2., rev. edition, 2000.

[43] R. WIESENDANGER, *Theory of STM and Related Scanning Probe Methods*, Springer Series in Surface Sciences ; 29, Springer, Berlin, 2. edition, 1996.

[44] J. TERSOFF and D. R. HAMANN, *Phys. Rev. Lett.* **50**, 1998 (1983).

[45] J. TERSOFF and D. R. HAMANN, *Phys. Rev. B* **31**, 805 (1985).

[46] C. J. CHEN, *Phys. Rev. Lett.* **65**, 448 (1990).

[47] R. LANDAUER, *IBM J. Res. Dev.* **1**, 223 (1957).

[48] M. BÜTTIKER, Y. IMRY, R. LANDAUER, and S. PINHAS, *Phys. Rev. B* **31**, 6207 (1985).

[49] M. BÜTTIKER, *Phys. Rev. Lett.* **57**, 1761 (1986).

[50] K. K. SAHA, J. HENK, A. ERNST, and P. BRUNO, *Phys. Rev. B* **77**, 085427 (2008).

[51] J. ENKOVAARA, D. WORTMANN, and S. BLÜGEL, *Phys. Rev. B* **76**, 054437 (2007).

[52] M. CZERNER, G. RODARY, S. WEDEKIND, D. V. FEDOROV, D. SANDER, I. MERTIG, and J. KIRSCHNER, *J. Magn. Magn. Mater.* **322**, 1416 (2010).

[53] S. DATTA, *Electronic transport in mesoscopic systems*, Cambridge studies in semiconductor physics and microelectronic engineering ; 3, Cambridge Univ. Press, Cambridge, 1st paperback (with corrections) edition, 1997.

[54] M. DI VENTRA, *Electrical transport in nanoscale systems*, Cambridge Univ. Press, Cambridge, 2008.

[55] G. A. FIETE and E. J. HELLER, *Rev. Mod. Phys.* **75**, 933 (2003).

[56] M. JULLIÈRE, *Phys. Lett. A* **54**, 225 (1975).

[57] J. C. SLONCZEWSKI, *Phys. Rev. B* **39**, 6995 (1989).

[58] T. MIYAZAKI and N. TEZUKA, *J. Magn. Magn. Mater.* **139**, L231 (1995).

[59] J. S. MOODERA and L. R. KINDER, *Appl. Phys. Lett.* **79**, 4724 (1996).

[60] P. WEINBERGER, *Phys. Rev. B* **80**, 060403 (2009).

[61] V. L. MORUZZI, J. F. JANAK, and A. R. WILLIAMS, *Calculated electronic properties of metals*, Pergamon Press, New York, 1978.

[62] A. L. BASSI, C. S. CASARI, D. CATTANEO, F. DONATI, S. FOGLIO, M. PASSONI, C. E. BOTTANI, P. BIAGIONI, A. BRAMBILLA, M. FINAZZI, F. CICCACCI, and L. DUÒ, *Appl. Phys. Lett.* **91**, 173120 (2007).

[63] M. JOHNSON and J. CLARKE, *J. Appl. Phys.* **67**, 6141 (1990).

[64] W. WULFHEKEL and J. KIRSCHNER, *Appl. Phys. Lett.* **75**, 1944 (1999).

[65] H. J. HUG, B. STIEFEL, P. J. A. VAN SCHENDEL, A. MOSER, S. MARTIN, and H.-J. GÜNTHERODT, *Rev. Sci. Instrum.* **70**, 3625 (1999).

[66] F. J. GIESSIBL, *Rev. Mod. Phys.* **75**, 949 (2003).

[67] C. ENSS and S. HUNKLINGER, *Low-Temperature Physics*, Springer-Verlag Berlin Heidelberg, Berlin, Heidelberg, 2005.

[68] W. BUCKEL, R. KLEINER, and R. HUEBENER, *Superconductivity. Fundamentals and applications*, Physics textbook, Wiley-VCH, Weinheim, 2., rev. and enl. ed. edition, 2004.

[69] Lake Shore Cryogenics, Inc., *Temperature Measurement and Control Catalogue*, 2004.

[70] S. H. PAN, E. W. HUDSON, and J. C. DAVIS, *Rev. Sci. Instrum.* **70**, 1459 (1999).

[71] M. PASSONI, F. DONATI, A. L. BASSI, C. S. CASARI, and C. E. BOTTANI, *Phys. Rev. B* **79**, 045404 (2009).

[72] M. ZIEGLER, N. NÉEL, A. SPERL, J. KRÖGER, and R. BERNDT, *Phys. Rev. B* **80**, 125402 (2009).

[73] S. M. York and F. M. Leibsle, *Phys. Rev. B* **64**, 033411 (2001).

[74] K. Kopitzki and P. Herzog, *Einführung in die Festkörperphysik*, volume 5., durchgesehene Auflage, B.G. Teubner, 2004.

[75] K. Oura, *Surface science. An introduction ; with 16 tables*, Advanced texts in physics, Springer, Berlin, 2003.

[76] OMICRON Vakuumphysik GmbH, Taunusstein, Germany, *Tip Etching Kit User Manual*, 1.1 edition, 1998.

[77] K. U. Schlickum, *Spin-polarized scanning tunneling microscopy studies on in-plane magnetization components of thin antiferromagnetic films on Fe(001)*, PhD thesis, Martin-Luther-Universität Halle-Wittenberg, 2005.

[78] R. Wiesendanger, D. Bürgler, G. Tarrach, T. Schaub, U. Hartmann, H. J. Güntherodt, I. V. Shvets, and J. M. D. Coey, *Appl. Phys. A* **53**, 349 (1991).

[79] W. Shockley, *Phys. Rev.* **56**, 317 (1939).

[80] P. O. Gartland and B. J. Slagsvold, *Phys. Rev. B* **12**, 4047 (1975).

[81] M. F. Crommie, C. P. Lutz, and D. M. Eigler, *Science* **262**, 218 (1993).

[82] M. F. Crommie, C. P. Lutz, D. M. Eigler, and E. J. Heller, *Surf. Sci.* **361-362**, 864 (1996).

[83] P. T. Sprunger, L. Petersen, E. W. Plummer, E. Laegsgaard, and F. Besenbacher, *Science* **275**, 1764 (1997).

[84] L. Petersen, P. T. Sprunger, P. Hofmann, E. Lægsgaard, B. G. Briner, M. Doering, H.-P. Rust, A. M. Bradshaw, F. Besenbacher, and E. W. Plummer, *Phys. Rev. B* **57**, R6858 (1998).

[85] G. Rodary, D. Sander, H. Liu, H. Zhao, L. Niebergall, V. S. Stepanyuk, P. Bruno, and J. Kirschner, *Phys. Rev. B* **75**, 233412 (2007).

[86] N. W. Ashcroft and N. D. Mermin, *Solid state physics*, Saunders College Publ., Philadelphia, 1976.

[87] M. Sicot, O. Kurnosikov, O. A. O. Adam, H. J. M. Swagten, and B. Koopmans, *Phys. Rev. B* **77**, 035417 (2008).

[88] O. Pietzsch, A. Kubetzka, M. Bode, and R. Wiesendanger, *Science* **292**, 2053 (2001).

[89] O. Pietzsch, S. Okatov, A. Kubetzka, M. Bode, S. Heinze, A. Lichtenstein, and R. Wiesendanger, *Phys. Rev. Lett.* **96**, 237203 (2006).

[90] G. Rodary, S. Wedekind, H. Oka, D. Sander, and J. Kirschner, *Appl. Phys. Lett.* **95**, 152513 (2009).

[91] G. Rodary, S. Wedekind, D. Sander, and J. Kirschner, *Jap. J. Appl. Phys.* **47**, 9013 (2008).

[92] E. Y. Tsymbal, O. N. Mryasov, and P. R. LeClair, *J. Phys.: Condens. Matter* **15**, R109 (2003).

[93] M. Getzlaff, *Fundamentals of Magnetism*, Springer, 2008.

[94] D. Wortmann, S. Heinze, P. Kurz, G. Bihlmayer, and S. Blügel, *Phys. Rev. Lett.* **86**, 4132 (2001).

[95] J. A. Stroscio, D. T. Pierce, A. Davies, R. J. Celotta, and M. Weinert, *Phys. Rev. Lett.* **75**, 2960 (1995).

[96] D. B. Dougherty, P. Maksymovych, J. Lee, M. Feng, H. Petek, and J. J. T. Yates, *Phys. Rev. B* **76**, 125428 (2007).

[97] F. Reinert, G. Nicolay, S. Schmidt, D. Ehm, and S. Hüfner, *Phys. Rev. B* **63**, 115415 (2001).

[98] K. Morgenstern, K.-F. Braun, and K.-H. Rieder, *Phys. Rev. Lett.* **89**, 226801 (2002).

[99] F. Baumberger, T. Greber, and J. Osterwalder, *Phys. Rev. B* **64**, 195411 (2001).

[100] L. Bürgi, O. Jeandupeux, A. Hirstein, H. Brune, and K. Kern, *Phys. Rev. Lett.* **81**, 5370 (1998).

[101] J. Li, W.-D. Schneider, R. Berndt, and S. Crampin, *Phys. Rev. Lett.* **80**, 3332 (1998).

[102] J. Kliewer, R. Berndt, and S. Crampin, *New J. Phys.* **3**, 22 (2001).

[103] J.-Y. Veuillen, P. Mallet, L. Magaud, and S. Pons, *J. Phys.: Condens. Matter* **15**, S2547 (2003).

[104] H. Jensen, J. Kroger, R. Berndt, and S. Crampin, *Phys. Rev. B* **71**, 155417 (2005).

[105] J. Li, W. D. Schneider, S. Crampin, and R. Berndt, *Surf. Sci.* **422**, 95 (1999).

[106] P. A. Ignatiev, *Theoretical study of spin-polarized surface states on metal surfaces*, PhD thesis, Martin-Luther-Universität Halle-Wittenberg, 2009.

[107] E. J. Heller, M. F. Crommie, C. P. Lutz, and D. M. Eigler, *Nature* **369**, 464 (1994).

[108] M. F. Crommie, C. P. Lutz, D. M. Eigler, and E. J. Heller, *Phys. D* **83**, 98 (1995).

[109] L. Bürgi, L. Petersen, H. Brune, and K. Kern, *Surf. Sci.* **447**, L157 (2000).

[110] W.-K. Li and S. M. Blinder, *J. Math. Phys.* **26**, 2784 (1985).

[111] P. N. Gorley, Y. V. Vorobiev, J. González-Hernández, and P. P. Horley, *Microelectron. Eng.* **66**, 39 (2003).

[112] N. A. Stavropoulos and D. K. Morr, *Phys. Rev. B* **71**, 140501 (2005).

[113] A. Wachowiak, J. Wiebe, M. Bode, O. Pietzsch, M. Morgenstern, and R. Wiesendanger, *Science* **298**, 577 (2002).

[114] K. von Bergmann, *Iron nanostructures studied by spin-polarised scanning tunneling microscopy*, PhD thesis, Universität Hamburg, 2004.

[115] M. Bode, A. Kubetzka, K. von Bergmann, O. Pietzsch, and R. Wiesendanger, *Microscopy Research and Technique* **66**, 117 (2005).

[116] C. P. Bean and J. D. Livingston, *J. Appl. Phys.* **30**, S120 (1959).

[117] S. Rohart, V. Repain, A. Tejeda, P. Ohresser, F. Scheurer, P. Bencok, J. Ferre, and S. Rousset, *Phys. Rev. B* **73**, 165412 (2006).

[118] D. Sander, *J. Phys.: Condens. Matter* **16**, R603 (2004).

[119] S. Rohart, V. Repain, A. Thiaville, and S. Rousset, *Phys. Rev. B* **76**, 104401 (2007).

[120] A. Hahlin, J. H. Dunn, O. Karis, P. Poulopoulos, R. Nunthel, J. Lindner, and D. Arvanitis, *J. Phys.: Condens. Matter* **15**, S573 (2003).

[121] M. P. Sharrock, *J. Appl. Phys.* **76**, 6413 (1994).

[122] C. Etz, MPI Halle, private communication.

[123] J. Izquierdo, A. Vega, and L. C. Balbs, *Phys. Rev. B* **55**, 445 (1997).

[124] H. L. Richards, S. W. Sides, M. A. Novotny, and P. A. Rikvold, *J. Magn. Magn. Mater.* **150**, 37 (1995).

[125] H. L. Richards, S. W. Sides, M. A. Novotny, and P. A. Rikvold, *J. Appl. Phys.* **79**, 5749 (1996).

[126] D. Hinzke and U. Nowak, *Phys. Rev. B* **58**, 265 (1998).

[127] U. Nowak, O. N. Mryasov, R. Wieser, K. Guslienko, and R. W. Chantrell, *Phys. Rev. B* **72**, 172410 (2005).

[128] R. Skomski, *Simple models of magnetism*, Oxford graduate texts, Oxford University Press, Oxford, 2008.

[129] S. Krause, G. Herzog, T. Stapelfeldt, L. Berbil-Bautista, M. Bode, E. Y. Vedmedenko, and R. Wiesendanger, *Phys. Rev. Lett.* **103**, 127202 (2009).

[130] H. Oka, P. A. Ignatiev, S. Wedekind, G. Rodary, L. Niebergall, V. S. Stepanyuk, D. Sander, and J. Kirschner, *Science* **327**, 843 (2010).

[131] C. D. Ruggiero, T. Choi, and J. A. Gupta, *Appl. Phys. Lett.* **91**, 253106 (2007).

[132] D. Bazhanov and V. Stepanyuk, MPI Halle, private communication.

[133] N. Oncel, *J. Phys.: Condens. Matter* **20**, 393001 (2008).

[134] A. Hubert and R. Schäfer, *Magnetic domains. The analysis of magnetic microstructures*, Springer, Berlin, 1998.

Publications

Parts of this thesis have been published in the following works:

1. G. Rodary, S. Wedekind, D. Sander, J. Kirschner, *Magnetic Hysteresis Loop of Single Co Nano-islands*, Jap. J. Appl. Phys. **47**, 9013 (2008)

2. G. Rodary, S. Wedekind, H. Oka, D. Sander, J. Kirschner, *Characterization of tips for spin-polarized scanning tunneling microscopy*, Appl. Phys. Lett. **95**, 152513 (2009)

3. M. Czerner, G. Rodary, S. Wedekind, D. V. Fedorov, D. Sander, I. Mertig, J. Kirschner, *Electronic picture of spin-polarized tunneling with a Cr tip*, J. Magn. Magn. Mater. **322**, 1416 (2010)

4. H. Oka, P. A. Ignatiev, S. Wedekind, G. Rodary, L. Niebergall, V. S. Stepanyuk, D. Sander, J. Kirschner, *Spin-Dependent Quantum Interference Within a Single Magnetic Nanostructure*, Science **327**, 843 (2010)

Acknowledgments

I am indebted to my supervisor Prof. Jürgen Kirschner for his continued support and promotion of my professional career in the last nine years and for giving me the opportunity to do my PhD work in his department. From various intense discussions I learned a lot about physics and the sometimes neglected good scientific practice.

I am as well indebted to Dr. Dirk Sander for his support and guidance, and for being an excellent teacher in many respects. His cheerful nature made working with him a great pleasure. I also benefited from his careful reading of the manuscript, which lead to numerous valuable improvements of this thesis.

Prof. Wolf Widdra from the University of Halle I would like to thank for acting as my mentor within the International Max-Planck-Research School.

I very much appreciate the contributions from our theory collaborators and the enlightening discussion that we had together. In particular I would like to thank Prof. Ingrid Mertig and Prof. Jamal Berakdar and their staffs from the University of Halle, and Dr. Larissa Niebergall, Dr. Corina Etz, Dr. Jürgen Henk, Dr. Pavel Ignatiev and Dr. Valeriy Stepanyuk from the theory department of the MPI Halle. Steven Achilles I would like to thank for fruitful discussions about some theoretical aspects of electron transport.

I am grateful to my friends and colleagues in the CryoSFM lab, Nicole Kurowsky, Dr. Guillemin Rodary, Dr. Hirofumi Oka, Fabio Donati, Dr. Safia Ouazi, Dr. Yasmine Nahas and Marco Corbetta, for their help and support and for creating an inspiring and cheerful working atmosphere.
I would like to acknowledge all people, who carefully read the manuscript for their helpful comments.

The electronics and mechanics workshop, the administration and all colleagues of the MPI Halle I would like to thank for their valuable technical and administrative support and for making the MPI Halle a great place to work at.

Last but not least I would like to express my gratitude to my family and my best friend Tom for keeping me connected to the non-scientific world.

I am most thankful to my dear wife Kathrin for her love, support and patience.

Curriculum vitae

Name, Vorname:	Wedekind, Sebastian
Geburtstag:	16. Juni 1981
Geburtsort:	Halle (Saale)
Staatsangehörigkeit:	Deutsch
Familienstand:	Verheiratet
Adresse (dienstlich):	Max-Planck-Institut für Mikrostrukturphysik, Weinberg 2, D-06120 Halle
Email:	swedek@mpi-halle.de

Bildungsgang

12/2006 - 11/2009	Doktorand am Max-Planck-Institut für Mikrostrukturphysik, Halle
09/2001 - 11/2006	Physikstudium an der Martin-Luther-Universität Halle-Wittenberg, Vertiefungsrichtung: Oberflächenphysik Diplomarbeit: *Aufbau und Charakterisierung eines Tieftemperatur-Rastertunnelmikroskops* Abschluss: Diplomphysiker
09/1992 - 07/2000	Mathematisch-naturwissenschaftliches Gymnasium "Georg Cantor", Halle, Abschluss: Allgemeine Hochschulreife

Halle (Saale), 27.11.2009

Sebastian Wedekind

Erklärung an Eides statt

Hiermit erkläre ich, dass ich die vorliegende Arbeit selbstständig und ohne fremde Hilfe verfasst, andere als die von mir angegebenen Quellen und Hilfsmittel nicht benutzt und die den benutzten Werken wörtlich oder inhaltlich entnommenen Stellen als solche kenntlich gemacht habe.
Eine Anmeldung der Promotionsabsicht habe ich an keiner anderen Fakultät einer Universität oder Hochschule beantragt.

Halle (Saale), 27.11.2009

Sebastian Wedekind